ASTRONOMICAL INSTITUTE
SLOVAK ACADEMY OF SCIENCES

PROCEEDINGS OF THE CONFERENCE

VII BREDIKHIN CONFERENCE

May 24 – 28, 2021, Zavolzhsk, Russia

CONTRIBUTIONS OF THE ASTRONOMICAL OBSERVATORY SKALNATÉ PLESO

• VOLUME LI •

Number 3

December 2021

ISSN: 1336–0337 (on-line version)

CODEN: CAOPF8

Editorial Office: Astronomical Institute of the Slovak Academy of Sciences
SK - 059 60 Tatranská Lomnica, The Slovak Republic

CONTENTS

The Contributions of the Astronomical Observatory Skalnaté Pleso
are available in a full version
in the frame of ADS Abstract Service
and can be downloaded in a usual way from the URL address:

‘’https://ui.adsabs.harvard.edu/‘’

as well as from the web-site of
the Astronomical Institute of the Slovak Academy of Sciences
on the URL address:

‘’https://www.astro.sk/caosp/caosp.php‘’

The journal is covered/indexed by:

Thomson Reuters services (ISI)
Science Citation Index Expanded (also known as SciSearch®)
Journal Citation Reports/Science Edition

SCOPUS

PROCEEDINGS OF THE CONFERENCE

Edited by:

Mikhail Sachkov & Anna Kartashova

VII BREDIKHIN CONFERENCE

May 24 – 28, 2021, Zavolzhsk, Russia

Institute of Astronomy Russian Academy of Sciences, Moscow, Russia
Zavolzhsk Municipal Museum , Zavolzhsk, Russia

http://agora.guru.ru/bredikhin2020/

LIST OF PARTICIPANTS

Omar Mutlag Al-Shiblawi	Ural Federal University, Russia
Elena Bakanas	Russian Space System, Institute of Astronomy Russian Academy of Sciences, Russia
Galina Bolgova	Institute of Astronomy Russian Academy of Sciences, Russia
Gennady Borisov	Moscow State University, Russia
Irina Brykina	Institute of Mechanics of Lomonosov Moscow State University, Russia
Ileana Chinnici	INAF - Palermo Astronomical Observatory, Italy
Vera Dorofeeva	Vernadsky Institute of Geochemistry and Analytical Chemistry of the Russian Academy of Sciences, Russia
Svetlana Duyndik	Crimean Federal University, Russia
Lidiya Egorova	Institute of Mechanics of Lomonosov Moscow State University, Russia
Vyacheslav Emel'yanenko	Institute of Astronomy Russian Academy of Sciences, Russia
Nataliya Emel'yanenko	Institute of Astronomy Russian Academy of Sciences, Russia
Alina Eremeeva	Moscow State University, Russia
Vladimir Efremov	Moscow Institute of Physics and Technology, Sadovsky Institute of Geosphere Dynamics, Russia
Dmitry Glazachev	Sadovsky Institute of Geosphere Dynamics, Russia
Vladislav Gusev	Ural Federal University, Russia
Victor Grokhovsky	Ural Federal University, Russia
Mária Hajduková	Astronomical Institute Slovak Academy of Sciences, Slovakia
Sergey Ipatov	Vernadsky Institute of Geochemistry and Analytical Chemistry of the Russian Academy of Sciences, Russia
Oleksandra Ivanova	Astronomical Institute Slovak Academy of Sciences, Slovakia
Sergey Kalabanov	Kazan Federal University, Russia
Anna Kartashova	Institute of Astronomy Russian Academy of Sciences, Russia
Svetlana Kasatkina	Zavolzhsk Municipal Museum , Russia
Gulchekhra Kokhirova	Institute of Astrophysics of the National Academy of Sciences of Tajikistan, Tajikistan
Nikolay Kruglikov	Ural Federal University, Russia
Vladimir Kuznetsov	Institute of Applied Astronomy of the Russian Academy of Sciences, Russia

Eduard Kuznetsov	Ural Federal University, Russia
Yuriy Medvedev	Institute of Applied Astronomy of the Russian Academy of Sciences, Russia
Andrey Murtazov	Ryazan State University named for S. Yesenin, Russia
Razilya Muftakhetdinova	Ural Federal University, Russia
Nikolay Perov	Cultural and Educational Center named V.V. Tereshkova, Russia
Evgeniya Petrova	Ural Federal University, Russia
Elena Podobnaya	Sadovsky Institute of Geosphere Dynamics, Russia
Olga Popova	Sadovsky Institute of Geosphere Dynamics, Russia
Firuza Rakhmatullaeva	Institute of Astrophysics of the National Academy of Sciences of Tajikistan, Tajikistan
Mikhail Sachkov	Institute of Astronomy Russian Academy of Sciences, Russia
Mikhail Savel'ev	Federal Center of Science and High Technologies VNII GOCHS, Russia
Maria Sizova	Institute of Astronomy Russian Academy of Sciences, Russia
Vasiliy Skotnikov	Yaroslavl State Pedagogical University named after K.D.Ushinsky, Russia
Marina Sokolova	Kazan Federal University, Russia
Valeriy Shematovich	Institute of Astronomy Russian Academy of Sciences, Russia
Boris Shustov	Institute of Astronomy Russian Academy of Sciences, Russia
Alexandra Terenjeva	Institute of Astronomy Russian Academy of Sciences, Russia
Vladimir Usanin	Kazan Federal University, Russia
Denis Ustinov	Ural Federal University, Russia
Sergey Vereshchagin	Institute of Astronomy Russian Academy of Sciences, Russia
Tamara Vinogradova	Institute of Applied Astronomy of the Russian Academy of Sciences, Russia
Grigory Yakovlev	Ural Federal University, Russia

PREFACE

A series of conferences dedicated to the latest achievements in the theory of comets and the dynamics of small bodies of the solar system called "Bredikhin Readings" was organized by the Russian Academy of Sciences (until 1991 of the USSR Academy of Sciences). The conferences are named after the great Russian astronomer Fedor Bredikhin, director of the Moscow Observatory, director of the Pulkovo Observatory, who made a decisive contribution to the development of comet and meteor research. Initially, it was planned that the conference would take place every three years and be held in places associated with Bredikhin. The first conference was held in 1983 in Zavolzhsk, Ivanovo region, Russia. There, until 1917 it was named the Kineshma district of Kostroma province, there was a manor “Pogost” (Churchyard), in which the scientist conducted his astronomical observations, where he made his most significant discoveries, a place that were visited by the scientific elite of pre-revolutionary Russia. Here (now - on the territory of the city of Zavolzhsk, Ivanovo region) is the family tomb of the Bredikhins - a monument of federal significance. The second Bredikhin readings were held in 1986 in Nikolaev (Ukraine), the place where the scientist was born. The third readings were held in 1989 at the Pulkovo Observatory, the director of which was Bredikhin. The fourth readings were held in 1992 in the city of Zavolzhsk. Further, for 22 years, the "Bredikhin readings" were not held. In 2014, on the initiative and with the support of the administration of Zavolzhsk and the Russian Academy of Sciences, it was decided to resume this conference. In 2014, the "V Bredikhin Conference" were successfully held. According to the results of the conference, it was decided to hold "Bredikhin conference" regularly in the city of Zavolzhsk. In May 2021, the VII Bredikhin conference were held.

The conference was held in three sections: "Comets", "Meteoroids, meteors, meteorites", "History of cometary astronomy". This collection includes original works written based on materials that were presented at the VII Bredikhin conference.

The most important contribution to the development of cometary astronomy was the results of the ROSETTA space mission. According to modern ideas, comets have retained the primary matter in their composition, so their study is of crucial importance for understanding the processes of formation of the Solar System. Many problems of determining the chemical composition of comets and studying the physical processes in their nuclei and comas can be solved exclusively using ultraviolet data, at the same time, a number of tasks require supplementing UV data with data obtained from ground-based telescopes. Due to the opacity of the earth’s atmosphere for UV radiation, obtaining data in the UV region of electromagnetic radiation is possible only using methods of extra-atmospheric astronomy. UV data is particularly important, because it is in the UV part of the spectrum that most of the astrophysical significant resonance lines of atoms (OI, CI, HI, etc.), molecules (CO, CO2, OH, etc.), and their ions are located. In recent years, interesting results have been obtained from

monitoring high-resolution spectra in the region of CaII lines in gas disks around selected stars, which is explained by cometary activity around these stars. We assume that UV observations will also be effective in exocometrical studies. A number of works presented in this collection are devoted to the upcoming World Space Observatory Ultraviolet project. This is one of the main projects of the Federal Space Program of Russia of fundamental space research. The project is to replace the Hubble Space Telescope in orbit. The equipment of the project should be ready in 2025 Most of the scientific research program is occupied by exoplanetary research. A number of articles in this special issue are also devoted to them. Meteor studies are important for understanding the processes of formation and evolution of the Solar System. The works of this collection are also devoted to this scientific problem.

I am pleased to acknowledge all who have contributed to the success of the conference. I thank for finance support the Administration of Zavolzhsk town. I am grateful to my fellow SOC members for valuable suggestions on invited speakers, assistance with putting together the scientific program. Special thanks to the Local Organizing Committee for conceiving the conference and managing all of its logistical aspects. We thank all participants for making this conference memorable and scientifically rewarding. I would like to express my special gratitude to the staff of the Zavolzhsk Municipal Museum and personally to the director Svetlana Kasatkina for her help in organizing the conference

Mikhail Sachkov, SOC Chair Moscow, November 2021

Contrib. Astron. Obs. Skalnaté Pleso **51**, 186 – 206, (2021)
https://doi.org/10.31577/caosp.2021.51.3.186

Small meteor ablation model: Applying to Perseid observations

V. Efremov[1,2], O. Popova[1], D. Glazachev[1], A. Margonis[3], J. Oberst[3,4] and A. Kartashova[5]

[1] *Sadovsky Institute of Geosphere Dynamics RAS, Moscow, Russia, (E-mail: efremov.vv@phystech.edu)*

[2] *Moscow Institute of Physics and Technology Moscow, Russia*

[3] *Technische Universität Berlin, Institute of Geodesy and Geoinformation Science Berlin, Germany*

[4] *German Aerospace Center (DLR), Institute of Planetary Research Berlin, Germany*

[5] *Institute of Astronomy RAS Moscow, Russia*

Received: August 1, 2021; Accepted: November 28, 2021

Abstract. We study the process of meteoroid interaction with the Earth's atmosphere, in particular, the effect of ablation. An ablation model is used, where mass loss of a meteoroid is determined using the saturated vapor pressure of the assumed meteoroid's substance. An automated method is suggested, where we estimate the physical parameters of a meteoroid by comparing data from observations and models of known parameters. Model constraints and features of the models are discussed.

Key words: Meteors – meteoroids – ablation model – Perseid shower

1. Introduction

Meteor bodies, along with asteroids and comets, carry important information about our Solar system, as the material, of which they are composed, testifies to the composition of matter in the early stages of Solar system evolution. Most part of these bodies do not reach the Earth's surface and do not become meteorites. A meteoroid entering the atmosphere produces radiation, ionization and sound waves. Analysis of these effects along with the meteoroid dynamics allows one to obtain information on the properties of the meteoric body and meteoric matter. In fact, the atmosphere is a detector to look at the properties of meteor bodies. The study of meteors permits one to learn more about the properties of asteroids and comets as they are the parent bodies of meteoroids.

Table 1. Locations of observational sites

Site	Coordinates		
	Longitude(°)	Latitude (°)	Altitude(m)
Mainalon	37.26	22.59	1600
Parnon	37.65	22.29	1400

This is more cost-effective than space missions, although does not completely replace them.

Most meteoric bodies do not reach the surface of the Earth, so their properties have to be determined by remote sensing techniques. The problem of accurately determining the mass and other properties of the meteoroids from observational data remains unresolved despite the long history of studying meteor events (Subasinghe et al., 2017). The details of the interaction of meteor particles with the atmosphere are poorly known, so all their characteristics are determined with large uncertainties.

To estimate parameters of meteoric bodies (mass, density, etc.) from observational data, various ablation models are used (Popova et al., 2019). Two different ablation models were applied to a number of meteors in Efremov et al. (2018), and the results showed a significant difference in parameter estimates. In this paper we apply specific ablation models to observations of the Perseids and determine the parameters of the meteoroids. The model uncertainties and constraints are discussed.

2. Observations and model

2.1. SPOSH camera and meteor observations

A series of observing campaigns were carried out during Perseids activity in the period 2010-2016 from southern Greece (Margonis et al., 2019).

SPOSH (Smart Panoramic Optical Sensor Head) cameras were used for observations (Fig.1). The SPOSH camera is a flexible and sensitive system designed for imaging meteors not only from Earth observations but also from space probes orbiting the Earth or other planets (Christou et al., 2012). The camera is equipped with a highly sensitive back-illuminated 1024x1024 CCD chip and has a custom made optical system of high light-gathering power with a wide field-of-view (FOV) of 120x120°. The camera was designed to capture meteors of magnitudes as faint as $+6^m$ moving at angular speeds of $5^\circ/s$ (Oberst et al., 2011).

Two SPOSH camera systems were deployed at two sites (Mainalon and Parnon) (Table 1), separated by a 51.5 km-long baseline. The camera fields-of-view from the two stations overlap due to the near all-sky coverage of the cameras. To determine the meteoroid speed, a rotating shutter consisting of

Figure 1. A SPOSH camera with a rotating shutter

two blades was mounted in front of the camera lens. The SPOSH data were acquired at Mt. Mainalon Station by Anastasios Margonis (TUB) and at Mt. Parnon Station by master students of the TUB along with DLR scientists. A software package developed for the SPOSH camera system was used (Margonis et al., 2018). The software consists of different modules, each carrying out distinct tasks in the characterization of a meteor event.

The range of absolute magnitudes of Perseid meteors recorded in August 2016 was from -6 to +2 magnitudes. Since the model used describes the ablation process of small meteor bodies (see below), meteors no brighter than -2^m were chosen.

2.2. Ablation model

An ablation model is used to estimate parameters of meteor bodies (mass, density, etc.) from observational data. In this model the incoming energy flux is used for thermal radiation cooling, meteoroid heating and ablation (Lebedinets, 1980; Popova et al., 2019). The mass loss of a particle is determined taking into account the saturated vapour pressure (Knudsen-Lengmuir equation). To determine the parameters of meteoric bodies a selection of initial data is required, which will allow one to reconstruct the observations by solving a system of differential equations describing the change in height, velocity, mass and luminosity as a function of time.

The energy balance and mass loss equations are as follows:

$$\frac{1}{2}c_h\rho_a V^3 = 4\varepsilon\sigma(T^4 - T_0^4) - \frac{L}{\pi R^2}\frac{dM}{dt} + \frac{4}{3}R\rho c\frac{dT}{dt} \tag{1}$$

$$dM/dt = -4\pi R^2 P_v(T)\sqrt{\mu/(2\pi kT)}, \tag{2}$$

where M, V are mass and velocity of the body; t is the time; ρ_a is an atmospheric density at flight altitude; g is the acceleration of gravity; L is an ablation heat; c_h is a heat transfer coefficient; T is the body temperature; T_0 is an atmospheric temperature; P_v is saturated vapor pressure; μ is average atomic mass of evaporating substance; ρ is the meteoroid density; R is the meteoroid radius; ϵ is an emissivity; c is a heat capacity; k is Boltzmann constant; σ is Stefan-Boltzmann constant.

The energy conservation equation is supplemented by the equations of motion:

$$dV/dt = -c_d \pi R^2 \rho_a V^2 / M, \tag{3}$$

$$d\gamma/dt = -g \cos\gamma / V, \tag{4}$$

$$dH/dt = -V \sin\gamma \tag{5}$$

and by the equation for the light curve:

$$I = -\tau \frac{dE_k}{dt}, \tag{6}$$

where H is the height above the planet's surface; γ is an entry angle (an angle of the trajectory inclination to the horizon); c_d is the drag coefficient; I is the intensity; E_k is the meteoroid kinetic energy; τ is a luminous efficiency.

This model assumed that sublimation begins as soon as the meteoroid temperature starts to rise (Lebedinec & Suskova, 1968; Love & Brownlee, 1991; Moses, 1992; Campbell-Brown & Koschny, 2004), and the temperature dependent mass loss rate being modelled using the KnudsenLangmuir formula (Bronshten, 1983).

The energy equation (1) is widely used in numerous papers devoted to the entry of small meteoroids in present form or with some modification (see review by Popova et al. (2019)). This ablation model is widespread in studies concerning the influx of micrometeorites, extraterrestrial matter, and cosmic dust as well the effects of this material on the atmosphere (see for example Plane (2012); Carrillo-Sánchez et al. (2016); Genge et al. (2017)).

For light curve fitting and meteoroid parameters determination the model is not used very often. The most elaborated model of this kind, which was applied to observational data, was suggested by (Campbell-Brown & Koschny, 2004) to model Leonids meteors. Their dustball model includes equations (1-6) and suggests that meteoroids fragment into fundamental grains when the threshold temperature is reached and the volatile 'glue' is destroyed (thermal disruption). Kikwaya et al. (2011) used the thermal disruption model (Campbell-Brown & Koschny, 2004) to fit observational data and to determine meteoroids parameters. It was required that the observed light curve and deceleration had to

be fitted simultaneously by the modeled ones. Bulk densities of the meteoroids were determined as well as other characteristics were estimated (e.g. grain mass, threshold temperature)(Kikwaya et al., 2011). Later Campbell-Brown (2017) and Armitage & Campbell-Brown (2020) modified the fragmentation mechanism of the thermal fracture model to better simulate meteor trails. Armitage & Campbell-Brown (2020) investigated the ablation of two meteoroids. Their task was to determine whether high-resolution wakes provide enough data to constrain the mass distribution of small meteoroid grains.

Čapek & Borovička (2017) used the ablation model (Eqs.(1-6)) as one of three possible ablation processes to describe the light curves and beginning heights of small iron meteoroids. They found that another process, i.e. the immediate removal of the liquid from the meteoroid's surface, is the most probable mechanism leading to the observed meteors (Čapek & Borovička, 2017; Čapek et al., 2019).

The studies mentioned above combined the considered ablation model with fragmentation to fit observational data. Here the described ablation model without fragmentation is applied to Perseid meteor observations as a first approach to look on the model constraints in more detail.

2.2.1. Model parameters

The size and density of the meteoroid, determined from the observational data, depend not only on the fitted curves of luminosity and deceleration, but also on the assumptions about the luminous efficiency, heat transfer coefficient, expressions for the vapor pressure, etc., used in the ablation model. We will call these quantities the parameters of the model, although they may be dependent on both the properties of the meteoroid and the mode of its flight.

The luminous efficiency τ represents the fraction of a meteoroid's kinetic energy converted into light, either bolometrically,or in a specific spectral bandpass. In principle, the luminous efficiency depends on the chemical composition of the body and its velocity, size and height of flight. Subasinghe et al. (2017) collected estimates of different authors and demonstrated that the estimates differ from 10 to 100 times.

In the current application of the ablation model the luminous efficiency (τ) was supposed to be constant over the entire flight of the meteoroid and ranged from 1% to 5% (Weryk & Brown, 2013; Subasinghe et al., 2017). In the most part of considered cases the luminous efficiency was fixed at $\tau = 5\%$. The power output by a zero magnitude meteor is one more factor of uncertainty. Weryk & Brown (2013) estimated the power of 0^m meteor to be in the range 770-1610 W for a number of passbands assuming the temperature in the radiative area to be 4500-6000 K. Here this value is fixed at 1100 W bolometrically.

The meteoroid was assumed to have a spherical shape. The heat transfer coefficient was supposed to be constant along the trajectory and to be equal to the value for the sphere in free-molecular mode ($c_h = 1$). The heat of ablation

(L) and the average atomic mass (μ) are determined by the substance and correspond to the used saturated vapour pressure P_v.

In the frame of this model meteoroid temperature is essential, and pre-warming is important. The altitude $H \approx 300$ km is a starting altitude, it is a reasonable compromise between accurate pre-heat accounting and calculation time. The numerical code is realized in WolframMath.

2.2.2. Vapour pressure uncertainty

In the ablation model under consideration, the mass loss is determined through the saturated vapour pressure of the meteoroid, for which different authors propose markedly different dependencies for the same substance (see below). The most commonly used pressure-temperature relationship is as follows:

$$\log_{10} P_v = A - B/T, \tag{7}$$

where A and B are constants for a given substance and may vary for different temperature ranges. These constants are usually determined experimentally (Bronshten, 1983).

One of the main components of meteorites is silicates, including olivine (Rubin, 1997). Olivine is a rock-forming mineral, a magnesia-iron silicate with the formula $(Mg, Fe)_2[SiO_4]$. Olivine forms a group or series of olivine. The Fe and Mg content varies between the two endmembers of the continuous isomorphic olivine series: forsterite (Fo) - $Mg_2[SiO_4]$ and fayalite (Fa) - $Fe_2[SiO_4]$. Olivine is one of the most common minerals on the Earth (Deer et al., 2013). In addition, olivine is one of the main minerals that make up extraterrestrial matter. Olivine can be found in of meteorites (Rubin, 1997), it is a major mineral in the lunar regolith (Arnold et al., 2016), and it is the most common mineral in samples brought back from the S-type asteroid Itokawa (Nakamura et al., 2011). The presence of olivine has also been confirmed in comet material (Hanner et al., 1997; Hanner, 1999) and in cosmic dust (Campins & Ryan, 1989; Rietmeijer, 2004; Borovička et al., 2019). Olivine is present in particles belonging to comet 81P/Wild (Wild II) delivered by the Stardust mission (Zolensky et al., 2008). Rosetta mission confirmed the presence of olivine in 67P/Churyumov-Gerasimenko comet (Pätzold et al., 2019).

The saturated vapour pressure dependence on temperature for olivine and few related substances are shown on Fig.2 according to a number of publications (references are given in Fig.2 caption). The melting temperature of olivine is in the range 1500-2100 K at atmospheric pressure in dependence on Fe/Mg content (Costa et al., 2017). It can be seen that at a temperature of 2000 K the pressure has a spread of three orders of magnitude. Often dependencies are obtained experimentally in a narrow temperature range and extrapolation is used over a wider temperature range. Part of the scatter in the data may be associated with this.

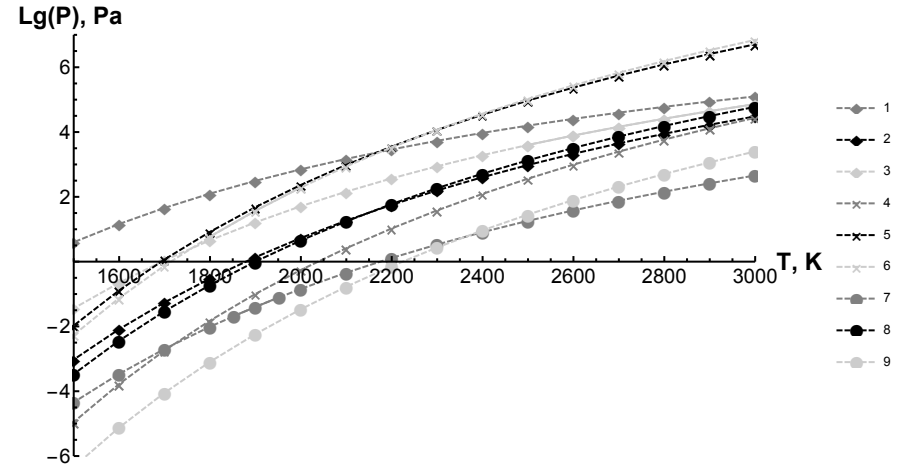

Figure 2. Dependence of saturated vapour pressure on temperature for olivine, silicates, iron and magnesium oxides according to different articles. The dashed lines mark the areas where the relationship for pressure is extrapolated. 1 - Baldwin & Sheaffer (1971), olivine and chondrite, 2 - Costa et al. (2017), olivine, 3 - Costa et al. (2017), olivine, vapours Fe/Mg, 4 - Sekanina & Chodas (2012), forsterite, 5 - Sekanina & Chodas (2012), fayalite, 6 - Kazenas & Chizhikov (1976), MgO, 7 - Kazenas & Chizhikov (1976), FeO, 8 - Kimura et al. (1997) , silicates, 9 - Kimura et al. (1997) , quartz.

Campbell-Brown & Koschny (2004) as well as subsequent publications (Kikwaya et al., 2011; Campbell-Brown, 2017; Armitage & Campbell-Brown, 2020; Vida et al., 2020) estimated the dependence of the saturated vapor pressure for some meteor substance based on the solution of Clausius-Clapeyron equation and calibrated on atmospheric pressure. The resulting function would be located above the function for olivine (Fig. 2) and would lead to higher pressures at 1000-2000 K.

Different studies used various dependences of saturated vapor pressure. For example, Moses (1992) studied the meteoroid influx and its effect in Neptune's atmosphere using the dependence close to Costa et al. (2017) data for olivine (Fig.2). Genge et al. (2017) modeled the entry heating of basaltic micrometeorites and used the ablation model with vapor pressure, for which the corresponding curve would be located slightly lower than quartz curve on Fig.2. Love & Brownlee (1991) studied the micrometeoroids entry in the Earth's atmosphere assuming pressure dependence with higher values at T≈1000-2500 K than curves shown on Fig.2 but lower than the dependence by Campbell-Brown & Koschny (2004). They claimed that the estimated rate of evaporative mass loss is consistent with that from the laboratory heating of Murchison chondrite.

Noticeable number of publications, which consider the influx of chemical elements into the Earth's upper atmosphere, are using Chemical Ablation Model (CABMOD, Vondrak et al. (2008)). In CABMOD the vapour pressures of the species evaporating from the meteoroid are calculated using the MAGMA chemical equilibrium code. This model allows one to consider differential ablation and to predict the injection rates of individual elements. Here we will not consider the differential ablation and will apply different pressure dependences for olivine and related substances in the ablation model.

2.2.3. The objective function

The objective function is a measure of the difference between the simulated light curve and that of the meteor. It serves as the quantitative metric that represents the fitness of a given solution.

Few objective functions were tested to gain a better understanding of the limitations and strengths of different options. In the first type of function considered, the intensity values are used to construct the discrepancy function, which is minimized during the solution search. The first discrepancy Δ_{AI} is as following:

$$\Delta_{AI} = \sqrt{\frac{\sum_i^n (I_o - I_s)^2}{n}}, \tag{8}$$

where I_o is the observed intensity, I_s is the solution intensity. The error is calculated at altitudes where observational data are available, n is the number of observational points. The intensity varies by orders of magnitude during the meteor flight, so another function was constructed based on relative error Δ_{RI}:

$$\Delta_{RI} = \sqrt{\frac{\sum_i^n ((I_o - I_s)/I_o)^2}{n}}, \tag{9}$$

Two other objective functions relied on meteor magnitude Δ_{AM} and relative magnitude Δ_{RM}:

$$\Delta_{AM} = \sqrt{\frac{\sum_i^n (M_o - M_s)^2}{n}}, \tag{10}$$

$$\Delta_{RM} = \sqrt{\frac{\sum_i^n ((M_o - M_s)/M_o)^2}{n}}, \tag{11}$$

where M_o is an observed magnitude, M_s is a solution magnitude. In order to avoid M_0 values in the $(0, \pm 1)$ interval and corresponding effects, both light curves were artificially shifted by 10 magnitudes (parallel transfer).

The meteoroid parameter was determined from the light curve only, as the deceleration curve was not recorded accurately. The absence of significant deceleration (a loss of no more than 10% of the initial velocity) was controlled. It

Table 2. Velocity, entry angle, absolute magnitude, and F-factor for the meteoroids in question. Estimates of mass from empirical relationships versus average mass obtained from four objective functions with saturated vapour pressure from Costa et al. (2017) (olivine, vapours Fe/Mg).

meteor	V	γ	M_v	Mass					F
	km/s	(°)		10^{-5} kg					
				Ja1967	Ve1965	Je2006	Vi2018	Modelling	
20160811_184336	60.7	12.8	-1.14	14.27	39.35	110.90	11.30	1.73±0.17	0.38
20160811_221139	58.3	32.1	-1.30	10.91	37.26	105.02	8.29	1.14±0.13	0.44
20160811_200532	61.3	17.0	-0.91	9.01	27.29	76.92	7.56	0.97±0.12	0.25
20160811_202351	60.7	21.4	-0.73	6.74	21.97	61.920	5.92	0.99±0.08	0.23
20160811_190504	66.2	14.8	-0.78	6.42	18.94	53.39	5.57	0.93±0.10	0.18
20160811_205252	59.4	21.5	-0.18	4.18	14.37	40.49	4.22	0.51±0.03	0.23
20160811_190233	66.8	13.3	0 .55	1.73	5.61	15.82	2.10	0.19±0.03	0.45
20160811_205351	59.4	22.0	-0.18	4.18	14.37	40.49	4.22	0.46±0.04	0.16
20160811_202522	60.4	19.0	-0.05	3.67	12.43	35.04	3.83	0.42±0.03	0.44
20160811_205505	60.5	22.0	0.12	2.81	10.02	28.23	3.06	0.39±0.02	0.31
20160811_205716	63.5	24.0	0.64	1.30	4.97	14.00	1.62	0.15±0.05	0.53

Note: Ja1967: Jacchia et al. (1967); Ve1965: Verniani (1965); Je2006: Jenniskens (2006); Vi2018: Vida et al. (2018)

should also be noted that we did not account for fragmentation in our model, although its role may be notable (Subasinghe et al., 2017).

3. Application of the ablation model to meteor data

The ablation model described above was used to simulate 11 meteors, whose velocity, entry angle and maximal absolute magnitude are given in Table 2.

3.1. Effect of the objective function

Application of the ablation model described above to observational data allows one to determine meteoroid parameters (mass, size and density). Meteoroid size and density were chosen as independent variables in the search for a solution. A comparison of the simulated and observed light curves for meteor 20160811_184336 is shown in Fig. 3 obtained with saturated vapour pressure from Costa et al. (2017) (olivine, vapours Fe/Mg). Four objective functions were used. Various objective functions better describe different parts of the light curve. Solution obtained using the discrepancy Δ_{AI}, based on the minimisation of the standard deviation, better describes the middle part of the light curve, other solutions better approximate the beginning and the end of the light curve.

Obtained parameters of meteor 20160811_184336 are collected in Table 3 for one saturated pressure dependence. The meteoroid mass estimate slightly

Table 3. Meteor 20160811_184336 parameters. Vapor pressure P_v from Costa et al. (2017)(olivine, vapours Fe/Mg, $L = 6 * 10^6$ J/kg).

Error Δ	Mass, 10^{-5} kg	Density, kg/m^3	Radius, cm	Value of Δ
Δ_{AI}	1.94	120	0.34	$3.79 * 10^{-8}$
Δ_{RI}	1.50	226	0.25	0.36
Δ_{AM}	1.82	224	0.27	2.20
Δ_{RM}	1.65	204	0.27	0.46
Mean value	1.73± 0.17	194± 43	0.28± 0.03	

depends on the choice of the objective function (the scatter is about 15% or less), the radius also depends slightly on the residual function (the scatter does not exceed 20%). At the same time, the density estimate demonstrates large scatter - up to two times.

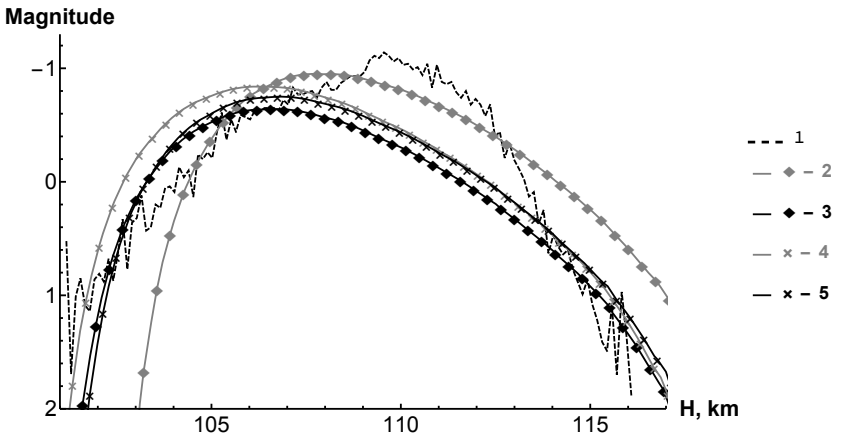

Figure 3. Light curve of meteor 20160811_184336 (dashed, curve 1) and model curves obtained with different objective functions: (2) - Δ_{AI}, (3) - Δ_{RI}, (4) - Δ_{AM}, (5)- Δ_{RM}. Saturated vapour pressure from Costa et al. (2017)(olivine, vapours Fe/Mg). Corresponding meteoroid parameters are shown in Table 3.

However, the solution found does not always describe the light curve accurately. For example for meteor 20160811_200532 the solution using the saturated vapour pressure from Sekanina & Chodas (2012) (fayalite) does not describe the light curve for objective functions Δ_{AM} and Δ_{RM} (Fig.4).This is due to the implemented solution search procedure. When the model solution has no data for brightness at certain altitudes (i.e. the model meteoroid burned out earlier than the observed one), a small value of magnitude $+10^m$ is formally assigned on

Table 4. Parameters of meteor 20160811_200532, vapor pressure P_v from Sekanina & Chodas (2012)(fayalite, $L = 2.46 * 10^6$ J/kg).

Error Δ	Mass 10^{-5} kg	Density kg/m^3	Radius cm	Δ
Δ_{AI}	0.92	611	0.15	$3.60 * 10^{-8}$
Δ_{RI}	0.89	574	0.15	0.55
Δ_{AM}	4.97	585	0.27	2.90
Δ_{RM}	7.23	487	0.33	0.88
Mean value	3.50±2.72	564±47	0.23±0.08	
Mean value for Δ_{AI} and Δ_{RI}	0.91±0.02	593±19	0.15	

Note: Uncertain values are marked gray

these altitudes. Under this condition, in some cases, the discrepancies Δ_{AM} and Δ_{RM} take the minimum values for the model light curves covering the entire height range, even if the model curves are located far from the observed ones. The continuation condition of the model curve will need to be reviewed and improved. At the moment unreliable solutions are not taken into account when estimating meteor parameters.

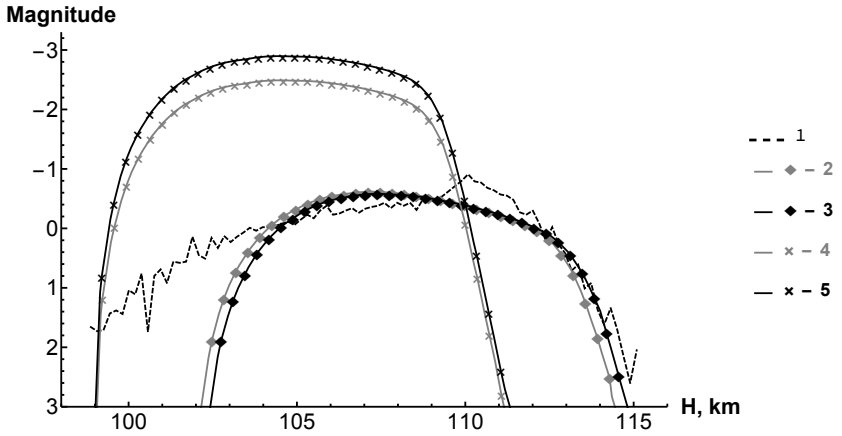

Figure 4. Meteor 20160811_200532 (dashed, curve 1) and model curves obtained with different objective functions: (2) - Δ_{AI}, (3) - Δ_{RI}, (4) - Δ_{AM}, (5) - Δ_{RM}. Saturated vapour pressure from Sekanina & Chodas (2012)(fayalite). Corresponding meteoroid parameters are shown in Table 4.

The quality of the description of the light curves within the considered ablation model varies from meteor to meteor. Figure 5 shows the model and observed

Table 5. Parameters of meteor 20160811_205716, vapor pressure P_v from Sekanina & Chodas (2012) (forsterite, $L = 3.86 * 10^6$ J/kg).

Error Δ	Mass, 10^{-5} kg	Density, kg/m^3	Radius, cm	Value of Δ
Δ_{AI}	0.15	485	0.09	$4.37 * 10^{-8}$
Δ_{RI}	0.15	519	0.09	0.19
Δ_{AM}	0.15	512	0.09	0.21
Δ_{RM}	0.15	512	0.09	0.03
Mean value	0.15	507±3	0.09	

light curves for meteor 20160811_205716. In this case, the parameters are the same for all the objective functions, and the density varies insignificantly (Fig.5, Table 5). The F-parameter (see below Section 3.3) is equal 0.5 (Table 2) for this meteor, one may assume that fragmentation is insignificant in this case.

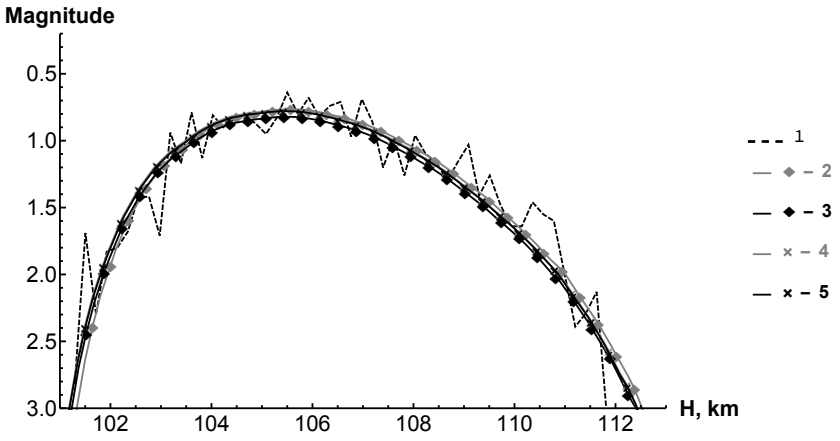

Figure 5. Meteor 20160811_205716 (dashed, curve 1) and model curves obtained with different objective functions: (2) - Δ_{AI}, (3) - Δ_{RI}, (4) - Δ_{AM}, (5) - Δ_{RM}. Saturated vapour pressure from Sekanina & Chodas (2012) (forsterite). Corresponding meteoroid parameters are shown in Table 5.

3.2. Influence of the dependence for saturated vapour pressure

As mentioned above, the estimate of meteoroid parameters also depends on the saturated vapour pressure used. Figure 6 and Table 6 shows the parameter estimates for meteor 20160811_184336 using different pressures P_v with the same objective function. Different dependences for vapor pressure significantly affect

the shape of the light curve and the quality of its fit. At one of the pressures (quartz (Kimura et al., 1997)) the solution found does not fit the observational data. With a minimum of discrepancy, the meteoroid is not burned up (due to the high heat of ablation), but decelerated. No significant deceleration is recorded in the observational data, so this solution is not taken into account in the parameter estimation.

When comparing the estimates obtained at different pressures, it can be seen that the deviation from the average value of mass is not more than 10%, and the size is not more than 35%. In terms of density, the spread five times higher or more can five times higher or more.. Thus, it is possible to estimate the mass of the meteoroid quite accurately, but the density estimate appears uncertain.

Table 6. Parameters of meteor 20160811_184336 obtained with different pressure dependences P_v and objective function Δ_{RI} .

Mass 10^{-5} kg	Density kg/m^3	Radius cm	L 10^6 J/kg	Δ	P_v
1.50	226	0.25	6	0.36	C2019,olivine, vapours Fe/Mg
1.67	119	0.32	6	0.42	C2019, olivine
1.63	77	0.37	3.86	0.59	SCh2012, forsterite
1.74	516	0.20	2.46	0.45	SCh2012, fayalite
1.66	88	0.36	7.12	0.43	K1997, silicates
1.64±0.08	205±164	0.30±0.07		0.45±0.08	Mean without quartz
2.49	0.68	2.06	9.38	0.38	K1997, quartz

Note:C2019:Costa et al. (2017); SCh2012:Sekanina & Chodas (2012); K1997:Kimura et al. (1997). Uncertain values are marked gray.

3.3. F-parameter

As it was mentioned above, the fragmentation is not included in our model although it may critically affect the light curve (LC). For the coarse estimate of the fragmentation influence on the light curve, F-parameter was suggested, where F is symmetry, a parameter with no units (Fleming et al., 1993). It is defined as the ratio of the one-sided width of the LC at 1^m below the peak, to the total width at this level. Formally F-parameter may be written as:

$$F = \frac{t_1 - t_M}{t_1 - t_2}, \tag{12}$$

where t_1 is the time near the beginning of the meteor when its brightness is 1^m fainter than the peak, t_2 is the time near the meteor end when its brightness is 1^m below the peak, and t_M is the time of the peak brightness (Brosch et al.,

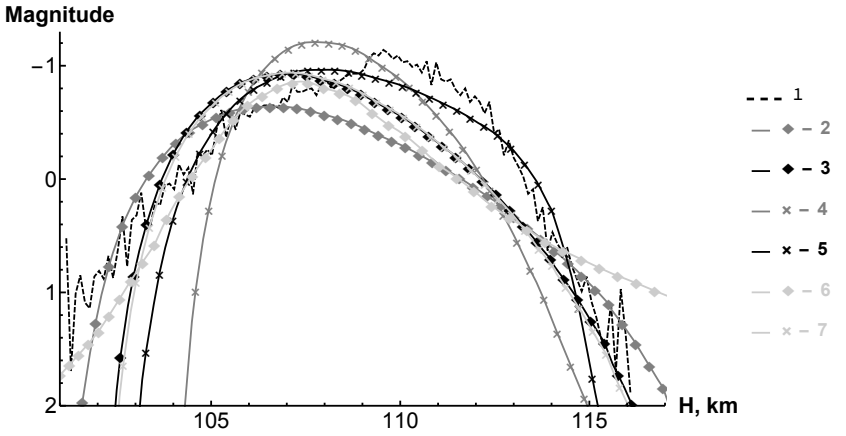

Figure 6. Luminosity curve of meteor 20160811_184336 (dashed, curve 1) and model curves obtained with Δ_{RI} discrepancy and using different dependencies for saturated vapour pressures: (2) - Costa et al. (2017) (olivine, Fe/Mg vapours), (3) - Costa et al. (2017) (olivine), (4) - Sekanina and Chodas (2012) (forsterite), (5) - Sekanina & Chodas (2012) (fayalite), (6) - Kimura et al. (1997) (quartz), (7) - Kimura et al. (1997) (silicates). Corresponding meteoroid parameters are shown in Table 6.

2004). F-parameter is used to classify meteoric bodies by the shape of the light curve.

Observed light curves of meteors under consideration are characterized by $F \approx 0.16 - 0.53$, i.e. their maxima are in the middle or are shifted towards the beginning of the light curve (Table 2). Our data fall within the interval found in the paper by Koten et al. (2004), who determined that F values for the Perseids are in the range 0.20 - 0.95 with the maximum distribution at 0.54. In the frame of our single body model F-parameter is about 0.5-0.7 (Fig. 3-6), its value varies with applied pressure dependences.

The closer the observed F-parameter is to 0.50, the more accurately its mass is determined. This model describes satisfactory meteoroids, whose F-parameter is about 0.4-0.5. For these meteoroids the fragmentation effect is less significant, all four objective functions yield close parameters (Fig.5). The meteors with $F \approx 0.2 - 0.3$ are probably be better modeled with fragmentation included. The fragmentation model will be included into consideration in future studies.

There is no correlation between estimated meteoroid density and the F parameter for our data sample. In our sample the size of the meteoroid has more influence than the shape of the light curve (see below).

3.4. Mass of the meteoroids

Meteoroid mass is often determined based on empirical relations obtained during many years of observations and their interpretation. These relations used meteor maximum magnitude, velocity and entry angle (Jacchia et al. (1967); Verniani (1965); Jenniskens (2006); Vida et al. (2018)). Mass estimates based on these relationships are shown in the Table 2, along with simulation results for the meteors in question. Estimates collected in the Table 2 demonstrate large uncertainty in mass determination - more than an order of magnitude, which is long-standing problem of meteor research.

All considered meteoroids are Perseids, and their velocity are close to each other. The application of the ablation model is consistent with the well-known correlation between meteor brightness and meteoroid mass, the smaller is the maximum brightness, the smaller is the obtained mass of the meteoroid (Table 2, Fig.7).

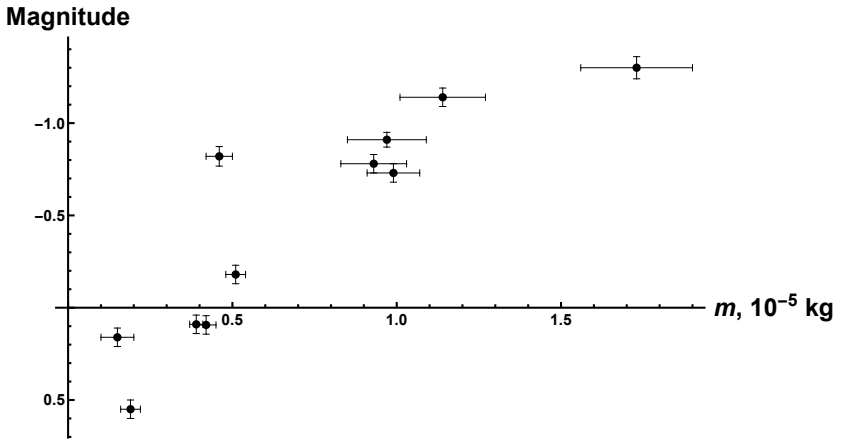

Figure 7. Relationship between meteor maximum brightness and meteoroid mass. Average mass value of the four objective functions with the saturated vapour pressure from Costa et al. (2017)(olivine, vapours Fe/Mg) was used.

The mass estimates we obtained are closest to the relationship from Vida et al. (2018) (difference by a factor of up to 10). Given that our estimates were obtained at a luminous efficiency of 5%, perhaps at lower efficiency of 1% the mass estimates would agree with the relationship from Vida et al. (2018).

3.5. Meteoroid density estimates

The density of meteoroids in our model is determined with a large uncertainty. The scatter in density may reach several times for the same meteor using dif-

ferent objection functions and different vapour pressures (see Table 3, 4, 5,6).

For the 11 meteors in question, the density spread is very wide, ranging from 50 to 1700 kg/m^3. The average density for all meteors is $\approx 362 \pm 237 kg/m^3$, for individual meteors the spread of average densities is from $114 \pm 99 to 640 \pm 500 kg/m^3$. In some solutions we get unusually low densities ($\approx 30 - 60\ kg/m^3$). There is a weak correlation between density and meteor brightness. For fainter meteors the average density is higher than for brighter ones. The highest correlation occurs with saturated pressure for fayalite (Sekanina & Chodas, 2012).There is no correlation between density and F-parameter. This is probably because meteoroids have different magnitudes, indicating a difference in size, and this in turn has a greater influence on the resulting density than the shape of the luminosity curve (which is characterised by the F-parameter).

Density estimation is influenced by both the choice of the objection function (variation up to 6 times) and the choice of dependence for pressure (up to 2-6 times). The highest particle densities are obtained using saturated vapour pressure for forsterite (Sekanina & Chodas, 2012).

Our estimates are within the range of known cometary densities. Density of dust particles of comet 67P/Churyumov-Gerasimenko collected by the COSIMA spacecraft in the Rosetta mission ranges from 100 to 400 kg/m^3 (Hornung et al., 2016), the average density of the comet itself is estimated as 537 kg/m^3 (Pätzold et al., 2019). Results on the physical properties reveal that dust particles are essentially aggregates of grains, with high porosities, from at least 50% to much higher values (see review Borovička et al. (2019)).

A number of papers have derived estimates of Perseid meteor densities from observational data. Bellot Rubio et al. (2002) analyzed 413 photographic meteors with brightnesses from -5^m to $+2.5^m$, obtained with Super-Schmidt cameras under single body and quasi-continuous fragmentation models. Both models assumed that all the energy of the incoming flux is spent on the ablation. The authors concluded that nearly three-quarters of the meteors in this set can be described within a single body model. The densities found under the single-body model are always lower than in the frame fragmentation model. For the 5 Perseid meteors the density was estimated at $600 \pm 100 kg/m^3$.

Babadzhanov (2003) estimated the densities of the 111 meteors observed in Dushanbe using the quasi continuous fragmentation model. For 44 Perseid meteors the density was estimated as $1300 \pm 200 kg/m^3$.The mean mineral density of bright Perseid meteoroids (191 meteors of -1^m to -9^m magnitude) was estimated at $2250 \pm 40 kg/m^3$ based on the solution of the heat-conduction equation (Babadzhanov & Kokhirova, 2009). 35% of these meteoroids have densities from 1000 to 2000 kg/m^3. In addition, a quasi-continuous fragmentation model has been used to simulate light curves and to estimate the meteoroid's bulk density and grain masses. This model allowed light curves to be reproduced and bulk densities to be estimated for the 97 Perseid meteors. The bulk density was estimated at $1200 \pm 200 kg/m^3$ and the porosity was about 45% (Babadzhanov & Kokhirova, 2009).

Kikwaya et al. (2011) studied a large group of meteors with brightness from $+2.5^m$ to $+6^m$, fitting light and deceleration curves to meteoroid parameters. The investigation was based on the thermal disruption model (Campbell-Brown & Koschny, 2004). The search for meteor body parameters was carried out in two stages. First the search was done over the entire parameter phase space and then over the selected area. For the 107 Perseid meteors the density of the meteoroids was in the range 420 - 820 kg/m^3.

Our density estimates turn out to be lower or comparable to those of other authors derived from the analysis of observational data with the help of different models. It is also worth bearing in mind that density estimates with fragmentation are typically higher.

4. Conclusions

A model describing the interaction of small meteoroids with the Earth's atmosphere is applied to observations of Perseid meteors in order to reproduce the light curves and to determine the parameters of meteoroids (density, size/mass). In this model, the mass loss of a meteoroid is determined using the saturated vapor pressure of the assumed meteoroid's substance. Dependencies of the saturated vapor pressure to the temperature of the same substance are different according to other authors, which affects the determination of the meteoroid parameters. An automated method to estimate the physical parameters of a meteoroid by comparing observational and model derived data with known parameters was suggested.

For testing the performance of the model optical meteor observations of SPOSH cameras in 2016 were used. The range of absolute magnitudes of meteors was selected as $-1.3^m - +1^m$. Parameters of meteoroids (density, size/mass) were obtained. The effects of the chosen dependence of saturated vapor pressure and used objective functions on meteoroid properties were considered.

The meteoroid parameters were determined from the light curves only, as the deceleration curves were not recorded, but the absence of significant deceleration (a loss of no more than 10% of the initial velocity) was controlled. It should also be noted that we have not considered fragmentation in our model, although its role may be significant.

The estimate of the mass of a meteoroid has little dependence on the choice of the objective function (deviation from the mean is no more than 15%), and the radius also has a low dependence on the objective function (deviation from the mean no more than 20%). At the same time, the dispersion in density is much higher.

Saturated vapour pressure dependences slightly affects the mass estimate (the deviation from the average value is no more than 10%), more pronounced effect occurs for radius estimate (t deviation is no more than 35%). Density spread may exceed five times. The vapour pressure dependence significantly

affects the shape of the light curve, the quality of its fitting and the estimation of density.

The chosen model better describes meteoroids for which the F-parameter exceeds $\approx 0.4-0.5$. For meteoroids with a high F value the effect of fragmentation is minimal, and the estimate of meteoroid parameters is only weakly dependent on the chosen objective function. For meteors with smaller F values, it is likely that fragmentation should be taken into account. The fragmentation model will be included into consideration in future studies.

The density of meteoroids within our model is determined with a large uncertainty, which may reach several times for the same meteor using different objective functions and vapour pressures. The average density for all meteors is $\sim 362\pm237 kg/m^3$. A comparison of our density estimates with data for cometary matter shows that our estimates are within the range of known cometary densities and appear to be lower or comparable to those of other authors, derived from the analysis of observational data in various models.

Acknowledgements.

AK to thank DAAD program "Research Stays for University Academics and Scientists, 2019"- 57440917. AM was financially supported by the German Research Foundation (DFG) - Project number (OB124/20-1).

References

Armitage, T. & Campbell-Brown, M., Constraining the grain mass distribution of small meteoroids using high resolution data. 2020, *Planetary Space Science*, **186**, 104915, DOI: 10.1016/j.pss.2020.104915

Arnold, J. A., Glotch, T. D., Lucey, P. G., et al., Constraints on olivine-rich rock types on the Moon as observed by Diviner and M3: Implications for the formation of the lunar crust. 2016, *Journal of Geophysical Research: Planets*, **121**, 1342, DOI: https://doi.org/10.1002/2015JE004874

Babadzhanov, P. B., Meteor showers associated with the near-Earth asteroid (2101) Adonis. 2003, *Astronomy and Astrophysics*, **397**, 319, DOI: 10.1051/0004-6361:20021506

Babadzhanov, P. B. & Kokhirova, G. I., Densities and porosities of meteoroids. 2009, *Astronomy and Astrophysics*, **495**, 353, DOI: 10.1051/0004-6361:200810460

Baldwin, B. & Sheaffer, Y., Ablation and breakup of large meteoroids during atmospheric entry. 1971, *Journal of Geophysics Research*, **76**, 4653, DOI: 10.1029/JA076i019p04653

Bellot Rubio, L. R., Martínez González, M. J., Ruiz Herrera, L., et al., Modeling the photometric and dynamical behavior of Super-Schmidt meteors in the Earth's atmosphere. 2002, *Astronomy and Astrophysics*, **389**, 680, DOI: 10.1051/0004-6361:20020672

Borovička, J., Macke, R. J., Campbell-Brown, M. D., et al. 2019, *Physical and Chemical Properties of Meteoroids*, ed. G. O. Ryabova, D. J. Asher, & M. J. Campbell-Brown, 37

Bronshten, V. A. 1983, *Physics of Meteoric Phenomena* (Dordrecht, Holland, D. Reidel Publishing Company), 358

Brosch, N., Helled, R., Polishook, D., Almoznino, E., & David, N., Meteor light curves: the relevant parameters. 2004, *Monthly Notices of the RAS*, **355**, 111, DOI: 10.1111/j.1365-2966.2004.08300.x

Campbell-Brown, M., Modelling a short-wake meteor as a single or fragmenting body. 2017, *Planetary Space Science*, **143**, 34, DOI: 10.1016/j.pss.2017.02.012

Campbell-Brown, M. D. & Koschny, D., Model of the ablation of faint meteors. 2004, *Astronomy and Astrophysics*, **418**, 751, DOI: 10.1051/0004-6361:20041001-1

Campins, H. & Ryan, E. V., The Identification of Crystalline Olivine in Cometary Silicates. 1989, *Astrophysical Journal*, **341**, 1059, DOI: 10.1086/167563

Carrillo-Sánchez, J. D., Nesvorný, D., Pokorný, P., Janches, D., & Plane, J. M. C., Sources of cosmic dust in the Earth's atmosphere. 2016, *Geophysics Research Letters*, **43**, 11,979, DOI: 10.1002/2016GL071697

Christou, A. A., Oberst, J., Elgner, S., et al., Orbital observations of meteors in the Martian atmosphere using the SPOSH camera. 2012, *Planetary Space Science*, **60**, 229, DOI: 10.1016/j.pss.2011.09.002

Costa, G. C. C., Jacobson, N. S., & Fegley, Bruce, J., Vaporization and thermodynamics of forsterite-rich olivine and some implications for silicate atmospheres of hot rocky exoplanets. 2017, *Icarus*, **289**, 42, DOI: 10.1016/j.icarus.2017.02.006

Deer, W., Howie, R., & Zussman, J. 2013, *An introduction of the rock-forming minerals* (Mineralogical Society of Great Britain and Ireland, London, United Kingdom), 498

Efremov, V.V.and Popova, O., Glazachev, D., & Kartashova, A., Determination of the meteor particles properties from observational data [in Russian]. 2018, *Dynamic processes in geospheres*, 150

Fleming, D. E. B., Hawkes, R. L., & Jones, J., Light curves of faint television meteors. 1993, in *Meteoroids and their Parent Bodies*, ed. J. Stohl & I. P. Williams, 261

Genge, M. J., Larsen, J., Van Ginneken, M., & Suttle, M. D., An urban collection of modern-day large micrometeorites: Evidence for variations in the extraterrestrial dust flux through the Quaternary. 2017, *Geology*, **45**, 119, DOI: 10.1130/G38352.1

Hanner, M. S., The Silicate Material in Comets. 1999, *Space Science Reviews*, **90**, 99, DOI: 10.1023/A:1005285711945

Hanner, M. S., Gehrz, R. D., Harker, D. E., et al., Thermal Emission From The Dust Coma Of Comet Hale-Bopp And The Composition Of The Silicate Grains. 1997, *Earth Moon and Planets*, **79**, 247, DOI: 10.1023/A:1006201820477

Hornung, K., Merouane, S., Hilchenbach, M., et al., A first assessment of the strength of cometary particles collected in-situ by the COSIMA instrument onboard ROSETTA. 2016, *Planetary Space Science*, **133**, 63, DOI: 10.1016/j.pss.2016.07.003

Jacchia, L., Verniani, F., & Briggs, R. E., An Analysis of the Atmospheric Trajectories of 413 Precisely Reduced Photographic Meteors. 1967, *Smithsonian Contributions to Astrophysics*, **10**, 1

Jenniskens, P. 2006, *Meteor Showers and their Parent Comets*

Kazenas, E. & Chizhikov, D., The Pressure and Composition of the Vapor above Oxides of Chemical Elements [in Russian]. 1976

Kikwaya, J. B., Campbell-Brown, M., & Brown, P. G., Bulk density of small meteoroids. 2011, *Astronomy and Astrophysics*, **530**, A113, DOI: 10.1051/0004-6361/201116431

Kimura, H., Ishimoto, H., & Mukai, T., A study on solar dust ring formation based on fractal dust models. 1997, *Astronomy and Astrophysics*, **326**, 263

Koten, P., Borovička, J., Spurný, P., Betlem, H., & Evans, S., Atmospheric trajectories and light curves of shower meteors. 2004, *Astronomy and Astrophysics*, **428**, 683, DOI: 10.1051/0004-6361:20041485

Lebedinec, V. N. & Suskova, V. B., Evaporation and Deceleration of Small Meteoroids. in , *Physics and Dynamics of Meteors*, ed. L. Kresak & P. M. Millman, Vol. **33**, 193

Lebedinets, V. N. 1980, *Dust in the upper atmosphere and cosmic space.*

Love, S. G. & Brownlee, D. E., Heating and thermal transformation of micrometeoroids entering the Earth's atmosphere. 1991, *Icarus*, **89**, 26, DOI: 10.1016/0019-1035(91)90085-8

Margonis, A., Christou, A., & Oberst, J., Observations of meteors in the Earth's atmosphere: Reducing data from dedicated double-station wide-angle cameras. 2018, *Astronomy and Astrophysics*, **618**, A99, DOI: 10.1051/0004-6361/201832927

Margonis, A., Christou, A., & Oberst, J., Characterisation of the Perseid meteoroid stream through SPOSH observations between 2010-2016. 2019, *Astronomy and Astrophysics*, **626**, A25, DOI: 10.1051/0004-6361/201834867

Moses, J. I., Meteoroid ablation in Neptune's atmosphere. 1992, *Icarus*, **99**, 368, DOI: 10.1016/0019-1035(92)90153-X

Nakamura, T., Noguchi, T., Tanaka, M., et al., Itokawa Dust Particles: A Direct Link Between S-Type Asteroids and Ordinary Chondrites. 2011, *Science*, **333**, 1113, DOI: 10.1126/science.1207758

Oberst, J., Flohrer, J., Elgner, S., et al., The Smart Panoramicfleming1993light Optical Sensor Head (SPOSH)—A camera for observations of transient luminous events on planetary night sides. 2011, *Planetary Space Science*, **59**, 1, DOI: 10.1016/j.pss.2010.09.016

Pätzold, M., Andert, T. P., Hahn, M., et al., The Nucleus of comet 67P/Churyumov-Gerasimenko - Part I: The global view - nucleus mass, mass-loss, porosity, and implications. 2019, *Monthly Notices of the RAS*, **483**, 2337, DOI: 10.1093/mnras/sty3171

Plane, J. M. C., Cosmic dust in the earth's atmosphere. 2012, *Chemical Society Reviews*, **41**, 6507, DOI: 10.1039/c2cs35132c

Popova, O., Borovička, J., & Campbell-Brown, M. D. 2019, *Modelling the Entry of Meteoroids*, ed. G. O. Ryabova, D. J. Asher, & M. J. Campbell-Brown, 9

Rietmeijer, F. J. M., Dynamic pyrometamorphism during atmospheric entry of large (∼10 micron) pyrrhotite fragments from cluster IDPs. 2004, *Met. Planet. Sci.*, **39**, 1869, DOI: 10.1111/j.1945-5100.2004.tb00082.x

Rubin, A. E., Mineralogy of meteorite groups. 1997, *Met. Planet. Sci.*, **32**, 231, DOI: 10.1111/j.1945-5100.1997.tb01262.x

Sekanina, Z. & Chodas, P. W., Comet C/2011 W3 (Lovejoy): Orbit Determination, Outbursts, Disintegration of Nucleus, Dust-tail Morphology, and Relationship to New Cluster of Bright Sungrazers. 2012, *Astrophysical Journal*, **757**, 127, DOI: 10.1088/0004-637X/757/2/127

Subasinghe, D., Campbell-Brown, M., & Stokan, E., Luminous efficiency estimates of meteors -I. Uncertainty analysis. 2017, *Planetary Space Science*, **143**, 71, DOI: 10.1016/j.pss.2016.12.009

Čapek, D. & Borovička, J., Ablation of small iron meteoroids-First results. 2017, *Planetary Space Science*, **143**, 159, DOI: 10.1016/j.pss.2017.03.004

Čapek, D., Koten, P., Borovička, J., et al., Small iron meteoroids. Observation and modeling of meteor light curves. 2019, *Astronomy and Astrophysics*, **625**, A106, DOI: 10.1051/0004-6361/201935203

Verniani, F., On the Luminous Efficiency of Meteors. 1965, *Smithsonian Contributions to Astrophysics*, **8**, 141

Vida, D., Brown, P., & Campbell-Brown, M., Physical properties and radiant distribution of the Orionids as observed by the Canadian Automated Meteor Observatory's mirror tracking system. 2020, in *European Planetary Science Congress*, EPSC2020–456

Vida, D., Brown, P. G., & Campbell-Brown, M., Modelling the measurement accuracy of pre-atmosphere velocities of meteoroids. 2018, *Monthly Notices of the RAS*, **479**, 4307, DOI: 10.1093/mnras/sty1841

Vondrak, T., Plane, J. M. C., Broadley, S., & Janches, D., A chemical model of meteoric ablation. 2008, *Atmospheric Chemistry & Physics*, **8**, 7015, DOI: 10.5194/acp-8-7015-2008

Weryk, R. J. & Brown, P. G., Simultaneous radar and video meteors—II: Photometry and ionisation. 2013, *Planetary Space Science*, **81**, 32, DOI: 10.1016/j.pss.2013.03.012

Zolensky, M., Nakamura-Messenger, K., Rietmeijer, F., et al., Comparing Wild 2 particles to chondrites and IDPs. 2008, *Met. Planet. Sci.*, **43**, 261, DOI: 10.1111/j.1945-5100.2008.tb00621.x

Contrib. Astron. Obs. Skalnaté Pleso **51**, 207 – 220, (2021)
https://doi.org/10.31577/caosp.2021.51.3.207

Observations of meteor showers with the meteor radar of KFU

S. Kalabanov[1], D. Korotyshkin[1], R. Ishmuratov[2], O. Sherstykov[1] and F. Valiullin[1]

[1] *Kazan Federal University, Russia, Kazan, 16A Kremlevskaya st., office 1404, (E-mail: kazansergei@mail.ru)*

[2] *Kazan State Power Engineering University, Russia, Kazan, 51 Krasnoselskaya st. (E-mail: rash-i@mail.ru)*

Received: August 1, 2021; Accepted: October 28, 2021

Abstract. The initial results of a new cycle (since 2016) of meteor observations in Kazan (56°N 49°E) which is associated with equipping of Kazan Federal University (KFU) with the new meteor radar SKiYMET are given. Simultaneously with the processing of experimental data using the built-in (native) software SKiYMET, the processing was performed using the new software developed in KFU. A comparative analysis showed a significant increase in the number of registrations due to the processing of meteors that are weaker with signal-to-noise ratio. The seasonal and daily dependencies of the meteor number for the period 2016-2019 are given. The obtained distributions of entry meteor speeds and their dependencies by seasons and heights of meteor trails are separately considered. The method of data processing for obtaining coordinates of meteor shower radiants in the equatorial coordinate system is described. The results of observations of the Geminids, Eta Aquariids, Arietids, April Lyrids, Northern and Southern Daytime Omega-Cetids, Daytime Lambda Taurids and Daytime Arietids meteor showers are presented.

Key words: Meteor radar – meteor shower – entry meteor speed – radiant coordinates – software

1. Introduction

1.1. Radar equipment and techniques for meteor observations

Radar observations of meteors in the world have been conducted for more than half a century since the middle of the last century (McKinley & Millman, 1949). They provide valuable information on the distribution of meteor matter near the Earths orbit. In addition, meteor phenomena are used in the study of the Earths average atmosphere (at heights of 80100 km), as well as in radio communications. Radar observations of meteors at Kazan University (56°N 49°E) began in 1956 and they were held for several decades in a row with a small breaks (Kostylev, 1958). During this time, the Kazan school of researchers was formed (Kalabanov et al., 2018b). One of the last significant scientific advances was the development

of a discrete quasitomographic method for determining the radiant coordinates of meteor showers. Using this method, it was possible to detect small meteor gathering (showers) and to compute the elements of their astronomical orbits (Sidorov et al., 2005) and (Kalabanov et al., 2018a).

The Kazan Meteor Radar (KMR) is a new generation system deployed on the scientific research area of Kazan Federal University, Tatarstan, Russia (56°N 49°E) in March 2015 developed and supplied by the Australian company Genesis Software (http://www.gsoft.com.au/productsandservices/skiymet). KMR is equipped with a 15 kW (pulse) transmitter with an average power of 1 kW. The carrier frequency of the radar is 29.75 MHz. The frequency of the probing pulses is 1594 Hz. The pulse duration is 24 μs. The basic configuration of the SkiYMET radar has one transmitting antenna (orthogonally dual Yagi 2-element antennas) with a circular radiation pattern (Fig.1). As a result there is full radiation coverage of the northern celestial hemisphere.

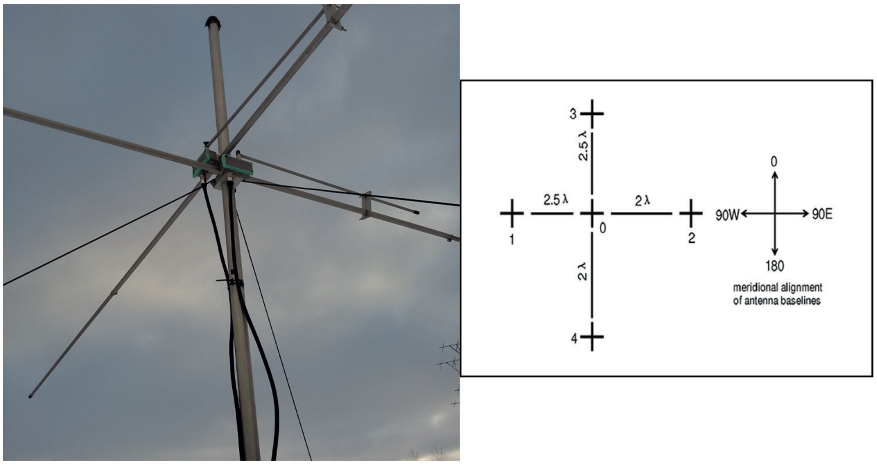

Figure 1. Orthogonally dual Yagi 2-element antennas and antenna system configuration of five antennas (0, 1, 2, 3, 4).

The receiving antenna system is a phase interferometer consisting of five antennas arranged in a cross (Fig.1). Each of the five antennas is also orthogonally dual 2-element Yagi antennas with a circular radiation pattern. The phase interferometer makes it possible to determine the angular coordinates of the reflecting points on the meteor tracks. The accuracy parameters for determining the angular coordinates (interferometric errors) depend on the signal-to-noise ratio (SNR) and on the duration of the meteor radio reflection (radio echo). Generally, interferometric errors are below 0.5 degrees, as for other systems based on SKYiMET. The heights of the registered meteor trails range from 80 to 100 km.

The radar provides observation and computation of the meteor number, the angular coordinates of the reflecting areas on meteor traces, the entry meteor speeds, as well as wind movements of the atmosphere (at heights of meteor traces).

1.2. Data processing technique

The method for processing of meteor observation data includes three consecutive stages: 1) primary processing of radar data - measurement of radio reflections and detection (identification) of a meteor; 2) estimation of the entry meteor speed; 3) calculation of the angular coordinates (azimuth and zenith) of the registered meteor radioechos.

After the first years of the radar operation, in addition to the native SKiYMET Genesis Software, we developed our own processing software for primary radar data and meteor detection (KFU software or KFU program). First, the KFU software performs pre-filtering of the primary radar data to eliminate non-meteor reflections of various nature (spark noise, signals reflected from aircrafts, ionosphere backscatter signals). This is provided by step-by-step data processing. In the KFU algorithm, these interfering unwanted objects (spikes and radio reflections from aircraft) are pre-analyzed in the total registration input data and then deleted before final processing (detection of meteor trails). A similar method of input data processing is described in detail in the article (Hocking et al., 2001). Using the new KFU software for input data makes the radar receiving system adaptive to noise environment (interference conditions). As a result, the new filtering algorithm allowed to significantly increase the efficiency of using SKYiMET equipment in terms of detecting meteors, as well as determining meteor parameters.

Secondly, the KFU program allows to estimate entry meteor speed much more efficient (than SKiYMET Software), thanks to the implementation of the Fresnel transform method and the applicable processing of the phase parameters of the radio signal, which we improved according to the works (Hocking, 2000) and (Elford, 2004). The average speed determination accuracy is 3 km/s.

Thus, we were able to significantly improve the quality and statistical indicators of the processed data. To illustrate this, in Table 1 it is shown the results of a comparative analysis of the effectiveness of data processing with two programs (statistics were collected for the entire observation period from November 2016 to December 2018).

As can be seen from Table 1, the KFU program can detect a much larger number of meteors. In addition, the number of meteors with estimated speeds is about 68% of the total number of meteor registrations (instead of 6% for SKiYMET Genesis Software). The achieved result allowed us to conduct more detailed studies of the meteor speed distribution (for different hours of the day and different months).

Table 1. Comparison of the efficiency of data processing using two programs (statistics are for the entire observation period from November 2016 to December 2018).

Statistical Data	SKiYMET Genesis Software	KFU Software	relation of exceeding (KFU/Skiymet)
Total Number of Meteors	3 266 901	8 696 502	2.66
Meteor Number with Estimated Speed	186 524	5 946 358	31.9
Percentage of Meteors with Speed	6	68	

The method for determining the angular coordinates (Azimuth and Zenith) of registered meteor radioechoes is described in detail in the article (Jones et al., 1998)

1.3. The initial main results of meteor observations in 2016-2018

This paper presents the first initial results of processing experimental data obtained from the new meteor radar. Fig. 2 shows the graphs of daily values of the meteor numbers for the observation cycle 2016-2018 (the processed results are presented in two alternative programs - KFU and SKiYMET programs). Sharp splashes of the curve on the graphs (for individual days) mean days with a partial interruption of observations during the day (due to repair or maintenance work at this time). It can be seen that the number of meteors using KFU program significantly exceeds the number of meteors obtained using the standard SkiYMET software.

Both graphs show a seasonal dependence on the number of meteors (with a maximum in summer and a minimum in early spring) due to the Earth passing through the areas of increased concentration of sporadic meteors distributed in space, as well as meteor showers, in the period from May to November. In addition, against the general background of the number of meteors, there are strong splashes corresponding to the dates of the main meteor showers: Geminids in December (12/16 and 12/17), Quadrantids in January (1/17) and Perseids in August (8/17). Also it can be seen Orionids in mid-October, Eta-Aquariids in late April - early May.

Another important parameter is the speed of meteor particles entering the atmosphere. As we have already noted, the KFU program for determining the entry meteor speed allowed not only to significantly increase the total percentage of recorded meteors while simultaneously determining their speeds (Table 1), but also to better detect meteors with higher speeds (> 50 km/s, Fig.3). In the presented speed distribution, no correction was made for observational biases (zenith attraction and the effect of Faraday rotation). The factor of the meteor

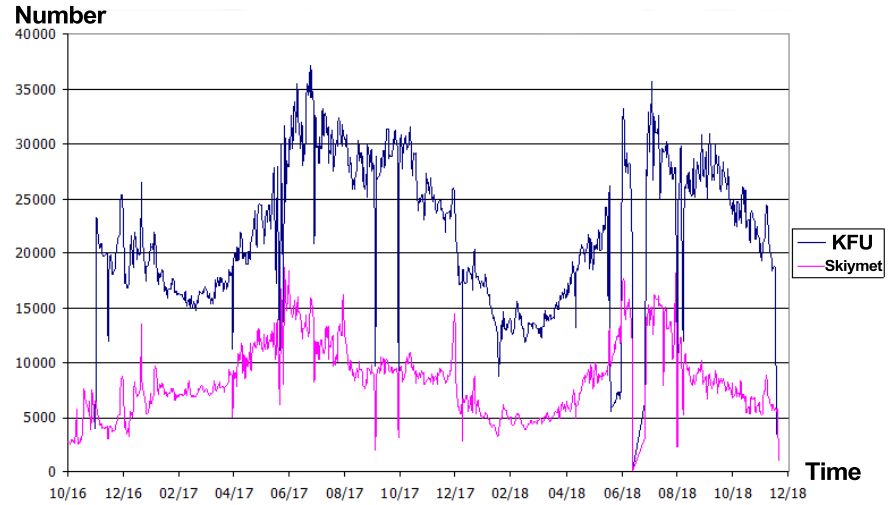

Figure 2. Annual variation of the daily number of meteors in 2016-2018 (detected by KFU and SKiYMET programs)

deceleration was also not taken into account. Since we are dealing with averaged distributions, all of these factors can be neglected here.

As you can see, on the graph of the seasonal dependence of the distribution of meteor speeds, there are two maxima: in the region of 30 km/s and 55 km/s (Fig.3). In general, during the year meteors prevail with speeds in the range of 20-40 km/s. In addition, some local maxima occur in January (which corresponds to the Quadrantid shower), as well as in December (35 km/s, Geminids). In Fig.3 it can be seen that a maximum in the region of 55 km/s appears from June to December. Comparison with Fig.2 shows that this is a period of strong meteor activity.

The distributions of speeds and heights (Fig.4) show a rather strong dependence of altitude on the meteor speed. In accordance with the meteor physics, meteors at high speeds begin to burn at high altitudes what is shown on the charts. A local increase in the number of meteors with speeds of about 55 km/s is also found in the work of other researchers, for example (Holdsworth et al., 2007). This feature of the speed distribution may be associated with heterogeneity in the distribution of meteor matter in the vicinity of the Earth's orbit. To give a more definitive answer to this question, it is necessary to compare the mutual distribution of meteors by speed and radiant. If high-speed meteors in the speed range of about 55 km/s are shown by close radiants, then we can speak of the existence of isolated meteoroid streams.

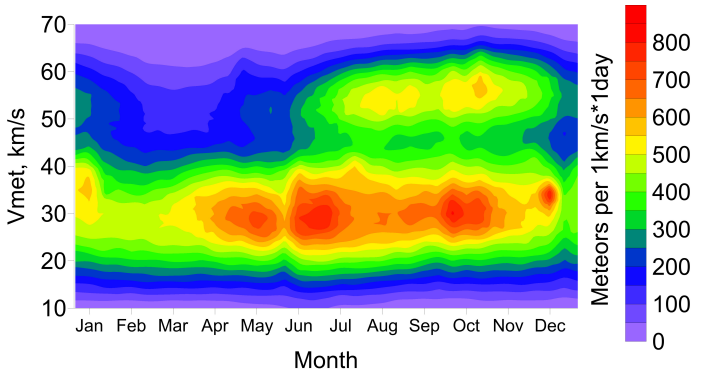

Figure 3. Meteor speed distribution depending on month of the year (for 2017).

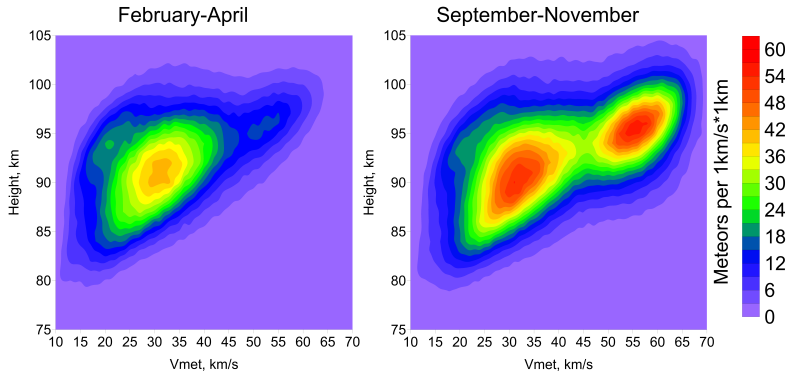

Figure 4. Meteor speed distribution depending on the height (for 2017).

2. Observations of meteor showers

2.1. Method of determination of meteor shower radiants

The method for determination the coordinates of meteor radiants was borrowed from (Jones & Jones, 2006). The entire celestial sphere is divided into elementary areas of 2x2 degrees in the equatorial coordinate system (α, δ). For each such place it is assigned a unit (test) vector T, which corresponds to the band on the celestial sphere AA (this is the location of points of possible meteor radioechoes) (Fig.5). In fact, the radioecho band GC corresponds to the observed radiant vector R. Next, the test vector T closest to the vector R is sought. Then, according to the Jones's method, the integration over the GC and AA bands is performed using the weighting function and as a result, we obtain the response from the transformation system. For the real observed meteor shower

after integration the response gives the maximum number of meteors and for the sporadic background it gives a minimum number.

To reduce the effect of the presence of a false positive result of the program, we apply the "strip with a positive part" (white stripe) and a "strip with a negative part" (black stripe). In fact, we thereby subtract the sporadic background from the radar response of the meteor shower.

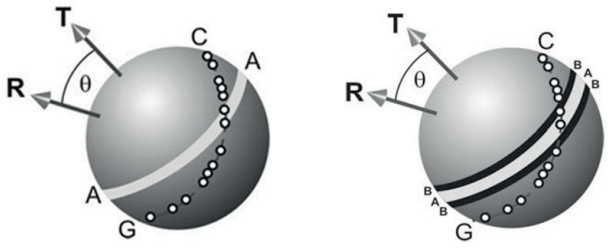

Figure 5. Explanation of the method for determination of meteor shower radiants (figures are taken from the materials of the article (Jones & Jones, 2006))

Based on this method, a computer program was developed that determines the coordinates of the radiants in the equatorial coordinate system (α, δ). The input parameters of the program are: the time of the event (radioecho), the angular coordinates of the radio reflection in the horizontal coordinate system (azimuth and zenith), and the entry speed of the meteor relative to the Earth. Fig.6 shows a screenshot of one of the KFU program tabs. Here you can set: sampling intervals by speed, by date, the width of the AA test band, thresholds and other parameters.

Fig.7 shows the distribution of the angular coordinates of radioechoes for one day (December 13, 2018) for the meteor speed range of 30-40 km/s. Shown here: in green - test band AA, corresponding to the previously known coordinates of the Geminid shower radiant, in red - to coordinates of the registered meteor shower radiant per day in the speed range of 30-40 km/s, in blue - to all meteors per day, including sporadic ones. It can be seen that the data correspond to each other.

After additional transformations, we finally build a 3D distribution of radiant coordinates over the celestial sphere in the equatorial coordinate system, which in this case take the following form (Fig.8). As can be seen, the distribution maximum is concentrated in a narrow region, which corresponds to a meteor shower. In this case, it is the Geminids shower.

Thus, using the Jones's method it is possible to obtain the coordinates of meteor radiants, number of meteors, dates of activity and represent them in the form of a set of three-dimensional graphs depending on speed and time.

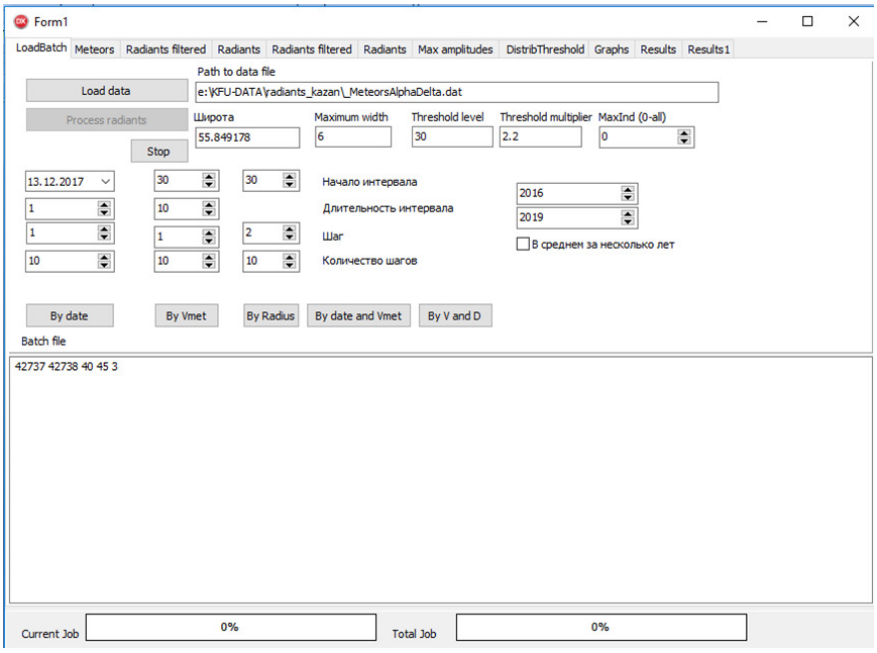

Figure 6. Screenshot of one of the KFU program tabs for determination of radiant coordinates

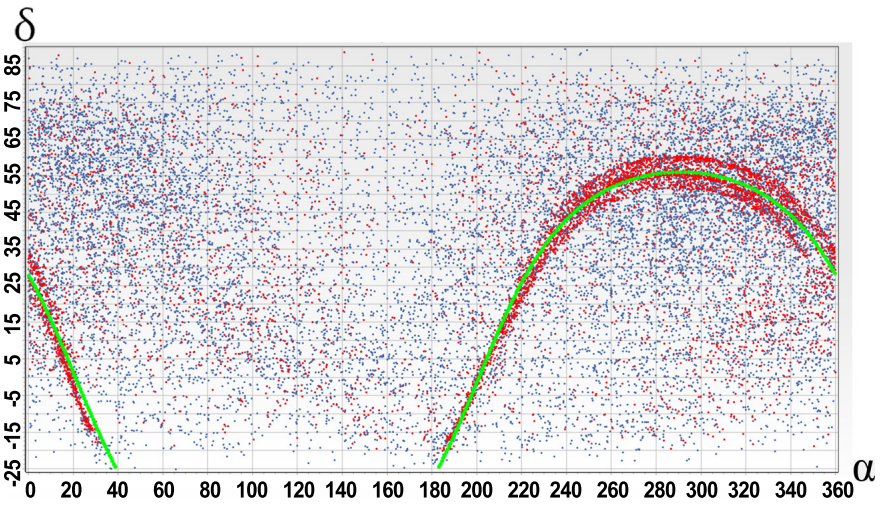

Figure 7. Distribution of angular coordinates of radioechoes in equatorial coordinate system for speed interval of 30-40 km/s for December 13th, 2018

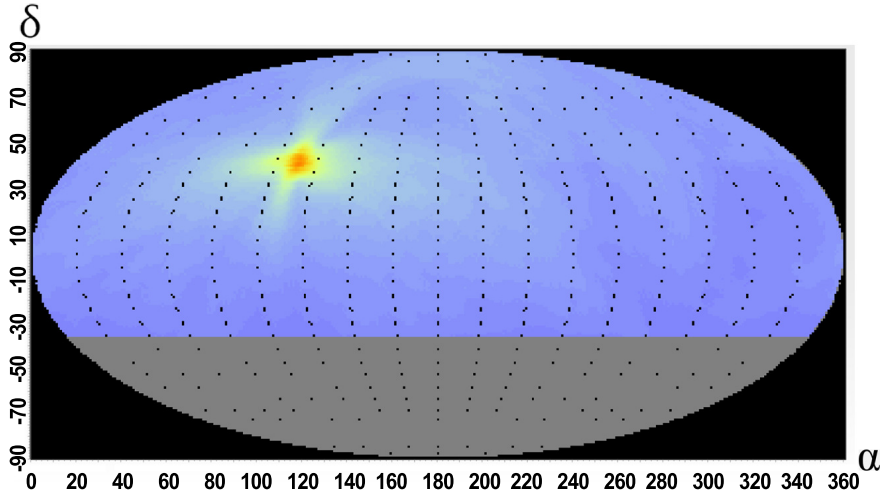

Figure 8. Distribution of Geminid radiants in equatorial coordinate system for December 13th, 2018

2.2. Results of observations

Let's move on to considering the results of observations of meteor showers. Fig.9 shows a summary 3D map of meteor activity for the period from 2017 to 2019. The srong showers are visible - the Quadrantids in January, the Eta-Aquariids in April, the Arietids in June, and the Geminids in December. The Perseids are poorly distinguished in August (which is obviously due to the increased general background of high-speed meteor activity in this area and at this time). All other meteor showers are also visible including the Draconids in 2018.

Fig.10-11 show observational data for the Eta-Aquariids and the Arietids meteor showers in 2017 and 2018. The graphs of changes of the registered number of meteors from day to day are shown, as well as graphs of the gradual daily shift of the radiant coordinates.

2.3. Brief results of observations of meteor showers in 2019

Throughout the full year of 2019, the meteor radar was in continuous operation (with the exception of a few hours associated with maintenance). A total of 43 showers were detected, six of which are shown in Fig.12-15. It should be noted that the showers of the southern hemisphere of the celestial sphere, namely the Southern June Aquilids and the Southern Iota Aquariids, were not registered using the KFU radar due to two factors: the location of the radar at northern latitudes (56°N 49°E) and low shower intensity. At the same time, in the case of sufficiently intense southern showers, such as the Alpha Capricornids, the

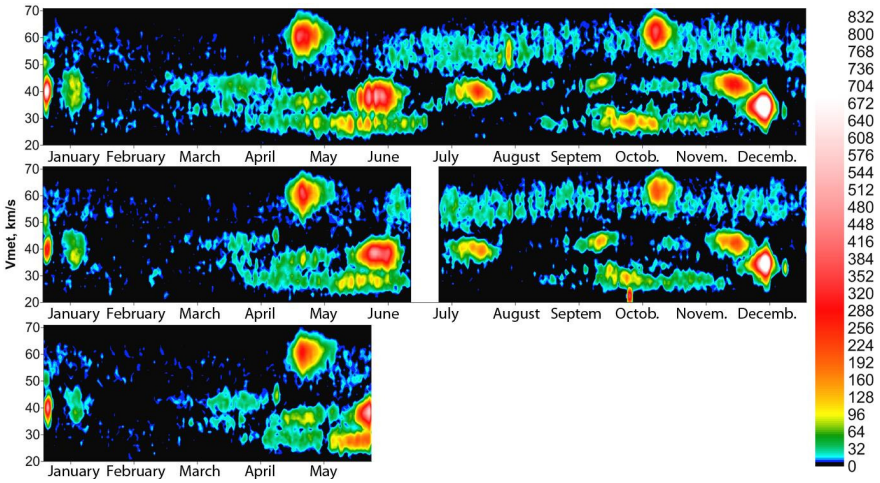

Figure 9. Distribution of meteor showers in 2017-2019

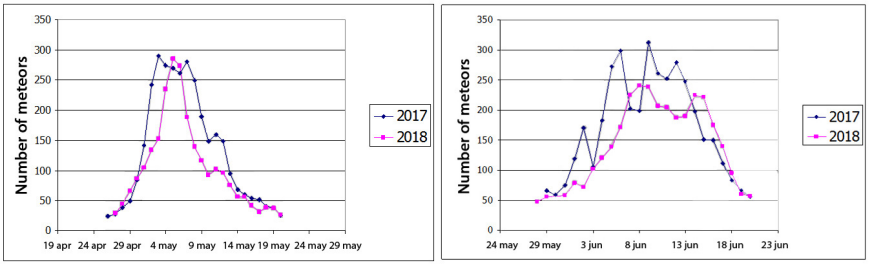

Figure 10. Meteor number from day to day in 2017-2018 (left - Eta Aquariids, right - Arietids)

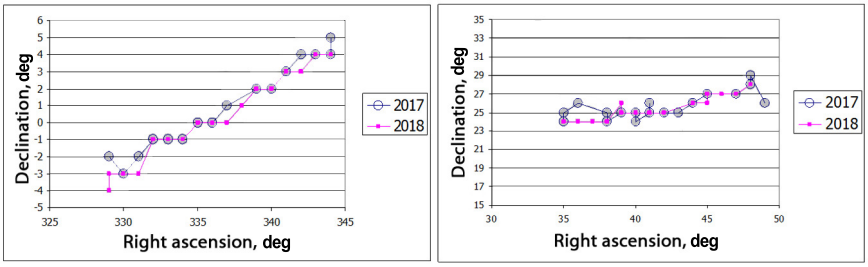

Figure 11. Daily shift of radiant coordinates (α, δ) in 2017-2018 (left -Eta Aquariids, right - Arietids)

Southern Delta Aquariids and the Piscis Austrinids the KFU radar was able to register them.

Let's move on to presenting of individual meteor showers. Fig.12-15 show the celestial sphere from -30° to +90° in declination (α) and from 0° to 360° in right ascension (δ). Fig.13 shows the April Lyrid shower with coordinates $\alpha = 273°$, $\delta = 34°$, speed 46.5 km/s, date of maximum intensity April 22. This is a low-intensity shower, the number of meteors in 4 days (for a speed range of 44-48 km/s) was 170 meteors. Fig.12 shows data of the Eta Aquariids shower with coordinates $\alpha = 339°$, $\delta = 0°$.

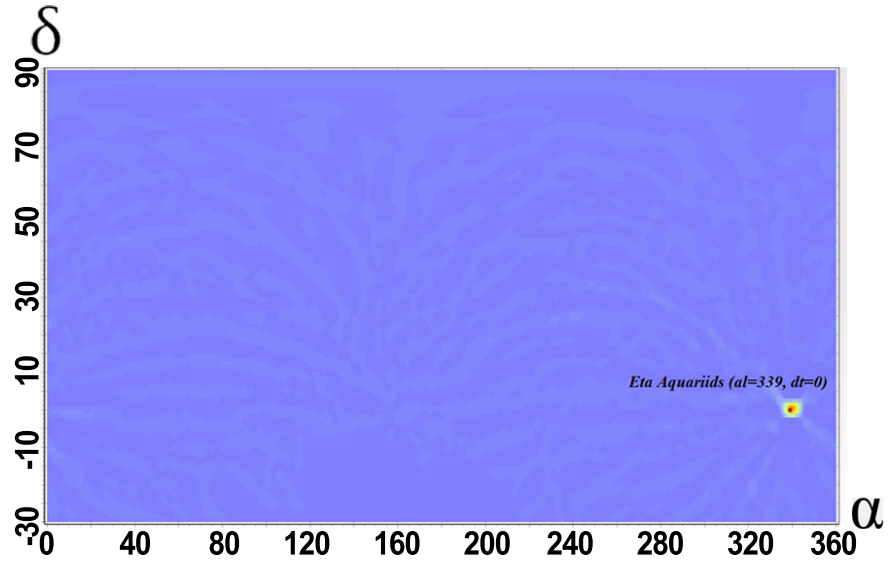

Figure 12. Position of the calculated radiant coordinates for the Eta Aquariids ($\alpha = 339°, \delta = 0°$) on the celestial sphere in equatorial coordinate system.

Fig.14 shows data of the Northern Daytime Omega-Cetids shower with coordinates $\alpha = 12°, \delta = 20°$ and the Southern Daytime Omega-Cetids shower with coordinates $\alpha = 23°, \delta = -3°$. Fig.15 shows the shower of Daytime Lambda Taurids with coordinates $\alpha = 57°, \delta = 13°$. At the same time, in this speed range, it can be seen a more powerful shower of the Daytime Arietids with coordinates $\alpha = 48°, \delta = 28°$.

All our data fully correspond to the work of other authors, in particular, to the work (Brown et al., 2008).

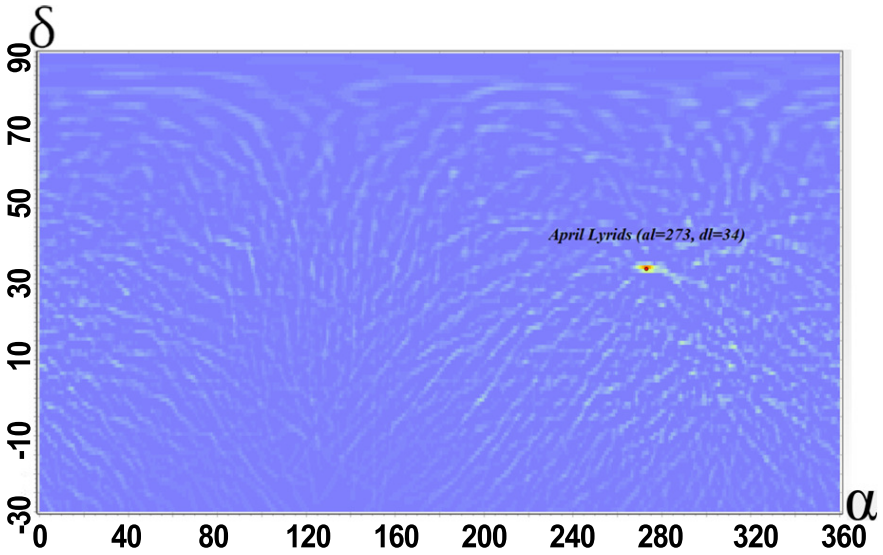

Figure 13. Position of the calculated radiant coordinates for the April Lyrids ($\alpha = 273^\circ$, $\delta = 34^\circ$) on the celestial sphere in equatorial coordinate system.

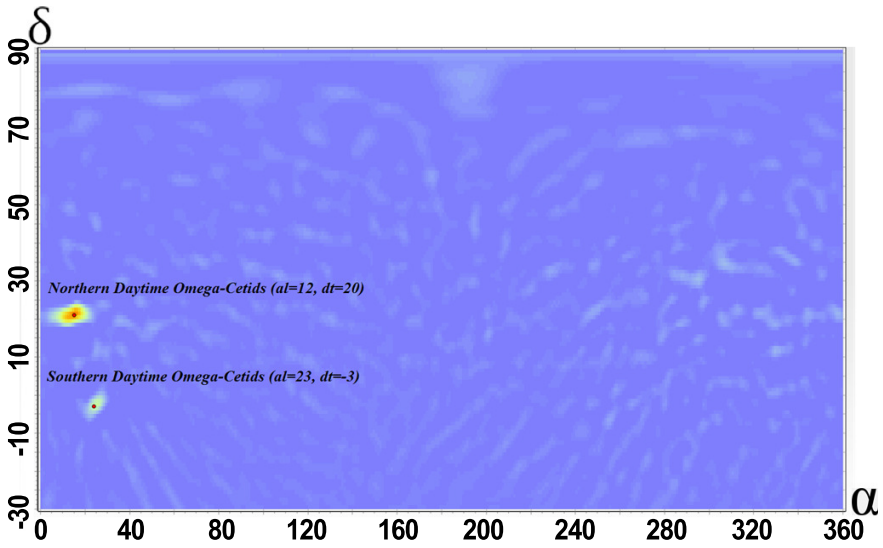

Figure 14. Position of the calculated radiant coordinates for the Northern Daytime Omega-Cetids ($\alpha = 12^\circ, \delta = 20^\circ$) and Southern Daytime Omega-Cetids ($\alpha = 23^\circ, \delta = -3^\circ$) on the celestial sphere in equatorial coordinate system.

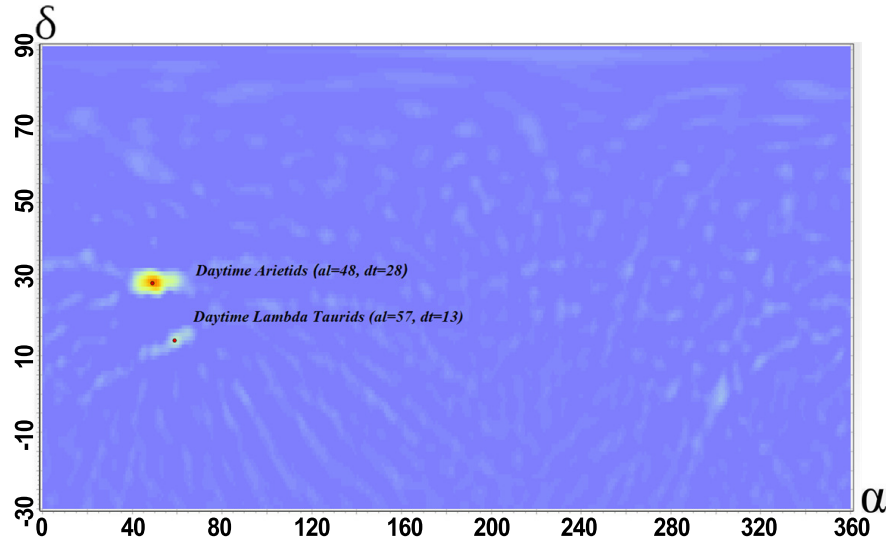

Figure 15. Position of the calculated radiant coordinates for Daytime Lambda Taurids ($\alpha = 57°, \delta = 13°$) and Daytime Arietids ($\alpha = 48°, \delta = 28°$) on the celestial sphere in equatorial coordinate system.

3. Conclusion

With the equipping of a new meteor radar at Kazan Federal University, a new stage of the long-term meteor observations and scientific researches in Kazan has begun. With the usage of our own algorithm for processing primary meteor registrations, it was possible to significantly improve the quality and statistical indicators of the processed data. Comparative analysis showed a significant increase in the number of registrations due to the processing of meteors with weaker signal-to-noise ratio. The introduction of a new algorithm for determining the speeds of meteors has proven to be especially effective, which makes it possible to perform detailed and statistically secured studies and analysis of experimental data.

The seasonal and daily dependencies of the number and speeds of meteors for the period 2016-2019 as well as the distribution of meteor speeds depending on the heights of meteor trails have been obtained. A total number of 43 meteor showers were registered, their radiant coordinates were calculated. The radiant distribution of the Eta Aquariids, Arietids, April Lyrids, Northern and Southern Daytime Omega-Cetids, Daytime Lambda Taurids and Daytime Arietids are presented.

Acknowledgements.
This work was funded by the Russian Government Program of Competitive Growth of Kazan Federal University.

References

Brown, P., Weryk, R., Wong, D., & Jones, J., A meteoroid stream survey using the Canadian Meteor Orbit Radar: I. Methodology and radiant catalogue. 2008, *Icarus*, **195**, 317

Elford, W., Radar observations of meteor trails, and their interpretation using Fresnel holography: a new tool in meteor science. 2004, *Atmospheric Chemistry and Physics*, **4**, 911

Hocking, W., Real-time meteor entrance speed determinations made with interferometric meteor radars. 2000, *Radio Science*, **35**, 1205

Hocking, W., Fuller, B., & Vandepeer, B., Real-time determination of meteor-related parameters utilizing modern digital technology. 2001, *Journal of Atmospheric and Solar-Terrestrial Physics*, **63**, 155

Holdsworth, D., Elford, W., Vincent, R., et al., All-sky interferometric meteor radar meteoroid speed estimation using the Fresnel transform. 2007, in *Annales Geophysicae*, Copernicus GmbH, 385–398

Jones, J. & Jones, W., Meteor radiant activity mapping using single-station radar observations. 2006, *Monthly Notices of the Royal Astronomical Society*, **367**, 1050

Jones, J., Webster, A., & Hocking, W., An improved interferometer design for use with meteor radars. 1998, *Radio Science*, **33**, 55

Kalabanov, S., Sherstyukov, O., Karpov, A., & Ishmuratov, R., Orbital structure of a meteoric complex in a vicinity of the Earth's orbit by Kazan meteor radar. Types of meteor orbits. 2018a, *Planetary and Space Science*, **161**, 84, DOI: doi.org/10.1016/j.pss.2018.06.015

Kalabanov, S. A., Karpov, A. V., Sulimov, A. I., Sherstyukov, O. N., & Ishmuratov, R. A., Progress of radar observations of meteors in Kazan (Russia) over the last sixty years. 2018b, *Proceedings of the International Astronomical Union*, **13**, 260, DOI: doi.org/10.1017/S1743921319000401

Kostylev, K. V., Radio equipment of the Engelgardts Astronomical Observatory for automatic observation of meteors (in Russian). 1958, *Astronomy Reports*, **4**, 643

McKinley, D. W. R. & Millman, P. M., A phenomenological theory of radar echoes from meteors. 1949, *Proceedings of the IRE*, **37**, 364

Sidorov, V., Kalabanov, S., Sidorova, S., Filin, I., & Filimonova, T., Associations of meteor microshowers or as the Kazan radar SEES radiants on northern celestial hemisphere. 2005, in *Modern Meteor Science An Interdisciplinary View* (Springer), 165–179

Contrib. Astron. Obs. Skalnaté Pleso **51**, 221 – 225, (2021)
https://doi.org/10.31577/caosp.2021.51.3.221

Potentials of spectroscopic studies of comets and exoplanets with WSO-UV mission

E. Kanev, S. Sichevsky, V. Shmagin and M. Sachkov

Institute of Astronomy,
Russian Academy of Sciences(E-mail: kanev@inasan.ru)

Received: August 5, 2021; Accepted: November 28, 2021

Abstract. In this article we consider the prospects of research on comets and exoplanets using instruments onboard the WSO-UV mission. Ultraviolet spectroscopy at 115-310 nm is a powerful tool for studying comets, since this range of the electromagnetic spectrum contains most of the resonance lines of atoms, molecules and ions. The spectrographs on board the WSO-UV spacecraft will become one of the most important instruments for spectral studies of comets and exoplanets after 2025.

Key words: UV – comets – exoplanets

1. Introduction

Observations in the ultraviolet (UV) range of the electromagnetic spectrum are the key to solving many problems in determining the chemical composition of comets. UV spectroscopy provides important information about the composition of a cometary coma. For example, radiation elements that originate from the products of dissociation of water: OH, H and O, or correspond to secondary atomic, molecular and ionic forms, such as C, C+, CO, CO+, CO+2 dominate in a cometary coma. Spectra and images provide information about the structure and dynamic characteristics of the coma and help to reveal the structure and other properties of the nuclei.

Comets are difficult to observe. We are limited to observing at a distance, so the key task is to distinguish between the signatures of the coma and the nucleus. Another problem is N2 and noble gases, which are very volatile and evaporate at very low temperatures. Thus, they are of particular interest for the thermal history of comets. But their UV-signature in a cometary coma has yet to be found. Observations of comets from space have several specific features (Sachkov, 2016). One of the space projects fitting most of the requirements for cometary observations is the World Space Observatory - Ultraviolet (WSO-UV). WSO-UV is a multipurpose international space mission created in response to the growing demand for UV facilities by the astronomical community (Sachkov et al., 2018).

2. Scientific tasks

The main scientific tasks of the WSO-UV observatory consist in spectroscopy of faint sources and imaging in the UV part of the spectrum. At the same time, the following should be achieved: high spectral resolution, maximum spatial resolution, and, for studies of faint sources, high permeability. The choice of parameters of the T-170M telescope (large diameter of the primary mirror (170 cm), special coatings that improve reflection in the UV range, high-precision guidance and stabilization systems, etc.) is due to the necessity for maximum angular resolution and maximum effective area in the range of 110-320 nm, in order to provide high-resolution spectroscopy and high-quality imaging (Sachkov et al., 2019).

2.1. Comets in UV with WSO-UV

A number of problems in the field of cometary research, in particular, the determination of the chemical composition of comets and the study of physical processes in their nuclei, can be solved only with the use of observational data in the UV range of the electromagnetic spectrum. Due to the opacity of the Earth's atmosphere, such studies can only be carried out by methods of exoatmospheric astronomy. At the same time, exoatmospheric cometary observations have a number of peculiarities compared to such studies of other astronomical objects.

Let's list the most significant of them. Comets are moving objects. Their speed can reach tens of arcseconds per hour. For example, comet Halley moves at 11" per hour relative to the stars. To obtain UV spectra, it is necessary not only to adjust the stabilization of the spacecraft during long exposures, but also to have a sufficiently accurate a priori knowledge of this velocity. It is important, especially for spectral studies, to take into account the dependence of the relative intensity of solar and cometary lines in the spectrum on the comet velocity. This is the so-called swing effect. It is associated with the fact that the lines in the solar radiation spectrum are shifted by the magnitude of the comets heliocentric velocity. The presence of solar lines in the spectrum significantly complicates observations for some cometary velocities. For example, for the C I 165 nm line at a speed of more than 40 km/s, the cometary line will be recorded three times weaker than the maximum possible.

Another important aspect of UV spectral studies of comets is the fact that comets are variable objects. Cometary nuclei produce short-lived tails and comas, which require continuous or quasi-continuous observations. Comets are extended objects. The most suitable instrument for their spectral research is a high-slit (long-slit) spectrograph. Such spectrographs were used in the rocket missions for observation of comet Hale-Bopp in 1997.

2.2. Exoplanets in UV with WSO-UV

Given the large aperture and the instrument sensitivity, WSO-UV will be one of the major workhorse for exoplanet observations. The current exoplanet research can be divided into five major aspects:

- planet detection,
- planet formation and migration,
- planets physical properties,
- planet's chemical properties and biomarkers,
- planets as a tool to study the properties of the host stars.

The WSO-UV mission will be a crucial tool for the study of the last four aspects (Fossati et al., 2014).

3. WUVS instruments of the WSO-UV mission

The spectroscopic capabilities of WSO-UV and HST are rather similar; in the NUV range, WSO-UV spectrographs will be more efficient than the HST/STIS spectrograph however, the sensitivity of HST/COS in the FUV range will not be matched by WSO-UV:

- high-resolution spectroscopic observations of pointlike objects in the 115 - 320 nm spectral range. Resolving power of the two high resolution spectrographs designed for observations in the NUV (180 – 320 nm) and FUV (110 – 180 nm) is $R > 50000$;
- low-resolution (resolving power $R > 1000$) spectral observations. A long slit spectrograph will operate in the 115 – 320 nm range too. It is especially suitable for faint and extended objects such as comets.

4. UV SPectrographs of the exospheres of Earth-like EXoplanet (UVSPEX)

In cooperation Russia-Japan FCU will be equipped UVSPEX spectrograph with MCP detector in the photon counting mode records spectra in the range of 115 - 135 nm. It is expected the spectrograph has a spectral resolution better than 0.5 nm. Thus, bservations of oxygen line OI (triplet 130.2 - 130.6 nm) during exoplanet transit can distinguish an Earth from a Venus or Mars (Tavrov et al., 2018).

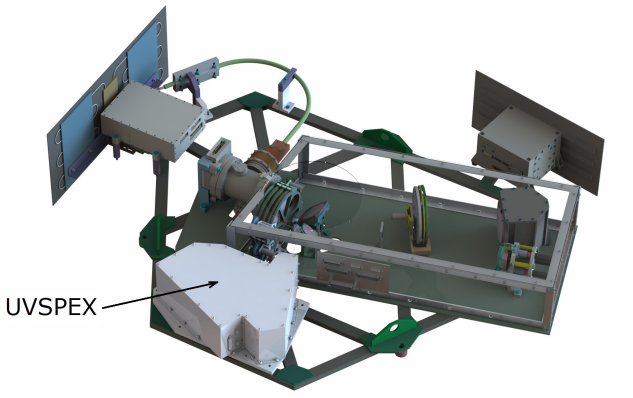

Figure 1. FCU general view.

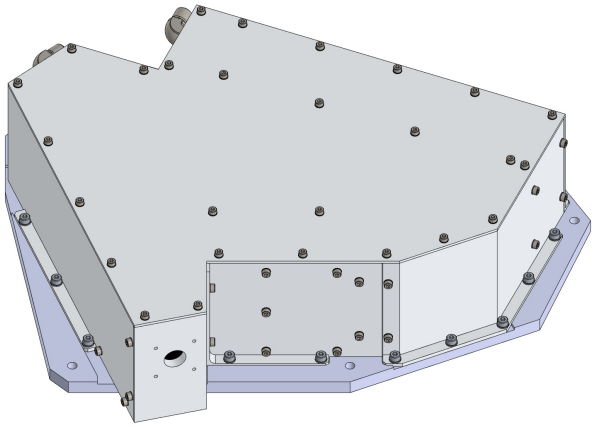

Figure 2. UVSPEX general view.

5. conclusions

The WSO-UV space observatory, which will be equipped with low- and high-resolution spectrographs, will be a very significant tool for cometary studies. Due to its high-resolution spectrographs and UVSPEX instrument, it will also become one of the main workhorses for exoplanet observations. WSO-UV will be ohe of the most important tool for the spectral studies of comets and exoplanets after 2025.

Acknowledgements. Authors acknowledge the support of Ministry of Science and Higher Education of the Russian Federation under the grant 075-15-2020-780 (N13.1902.21.0039).

References

Fossati, L., Bisikalo, D., Lammer, H., Shustov, B., & Sachkov, M., Major prospects of exoplanet astronomy with the World Space Observatory-UltraViolet mission. 2014, *Astrophysics and Space Science*, **354**, 9, DOI: 10.1007/s10509-014-2027-3

Sachkov, M., Panchuk, V., Klochkova, V., et al., Spectroscopic instrumentation of 1-m class telescopes for ground support of the space mission WSO-UV. 2019, *Contributions of the Astronomical Observatory Skalnate Pleso*, **49**, 142

Sachkov, M. E., Spectral studies of comets in the ultraviolet range and prospects of the WSO-UV project in these studies. 2016, *Solar System Research*, **50**, 294, DOI: 10.1134/S0038094616040055

Sachkov, M. E., Kartashova, A. P., & Emel'yanenko, V. V., Prospects for spectral studies of comets: The World Space Observatory - Ultraviolet project. 2018, *Planetary Space Science*, **164**, 75, DOI: 10.1016/j.pss.2018.06.013

Tavrov, A., Kameda, S., Yudaev, A., et al., Stellar imaging coronagraph and exoplanet coronal spectrometer: two additional instruments for exoplanet exploration onboard the WSO-UV 1.7-m orbital telescope. 2018, *Journal of Astronomical Telescopes, Instruments, and Systems*, **4**, 1 , DOI: 10.1117/1.JATIS.4.4.044001

Contrib. Astron. Obs. Skalnaté Pleso **51**, 226 – 240, (2021)
https://doi.org/10.31577/caosp.2021.51.3.226

Dynamic evolution of pairs of trans-Neptunian objects: the case of binary and single objects in pair

E. Kuznetsov, O. Al-Shiblawi and V. Gusev

Ural Federal University
Lenina Avenue, 51, Yekaterinburg, 620000 Russian Federation (E-mail: eduard.kuznetsov@urfu.ru)

Received: August 1, 2021; Accepted: October 20, 2021

Abstract. We performed a search for pairs of trans-Neptunian objects in close orbits with semi-major axes of more than 30 AU. Distances in the space of Keplerian orbits were estimated using the Kholshevnikov metrics. Found 21 pairs of trans-Neptunian objects in which one of the components is binary, for Kholshevnikov metrics in five-dimensional space of Keplerian orbits less than 0.121 $AU^{1/2}$. All pairs belong to cold Classical Kuiper belt objects. Based on nominal orbits, the dynamic evolution of pairs of trans-Neptunian objects in the past 10 Myr has been studied numerically. We searched for low relative-velocity close encounters between trans-Neptunian objects in pairs as well as the minima of the Kholshevnikov metrics and the convergence of the lines of nodes and apses, to estimate the age of the pairs.
Key words: Trans-Neptunian objects – Classical Kuiper belt objects – celestial mechanics

1. Introduction

Apart from Pluto and Charon, the first trans-Neptunian object (TNOs) was found in 1992. Although many TNOs were found on quite elliptic orbits, some of them had roughly circular orbits on a plane near the ecliptic (or the invariant solar system plane), today about 3 500 objects have been recognized and indexed. The distribution of the orbits of asteroids in the Solar System is the result of various processes that affect for a long time (see e.g. Deienno et al., 2016; Granvik et al., 2017).

As was shown in (Vokrouhlický & Nesvorný, 2008), in the main belt of asteroids, there are a large number of pairs of asteroids with close orbits that have a common origin. A study of these pairs (Pravec & Vokrouhlický, 2009) proved their statistical significance. Unbound pairs of asteroids have also been identified in (Pravec et al., 2010; Jacobson, 2016; Kuznetsov & Safronova, 2018). One candidate pair resides in the scattered disc (Rabinowitz et al., 2011). Groups of pairs define young asteroid clusters (Pravec et al., 2018; Kuznetsov & Vasileva, 2019).

Different processes can lead to the formation of pairs or groups of minor bodies with close orbits. It is collisional break-ups, rotational or thermal-stress-induced splittings, tidal disruptions, and binary dissociations (see e.g., (Benz & Asphaug, 1999; Boehnhardt, 2004; Sekanina & Chodas, 2005, 2007; Bottke et al., 2006; Jacobson & Scheeres, 2011; Schunová et al., 2014; Jacobson, 2016; Vokrouhlický et al., 2017). Mean motion and secular resonances can also induce orbital coherence (see e.g. de la Fuente Marcos & de la Fuente Marcos, 2016).

A candidate collisional family in the outer Solar system was proposed by Chiang (2002). The first asteroid family identified in the outer Solar system was the one associated with dwarf planet Haumea (Brown et al., 2007). The subject of finding collisional families of trans-Neptunian objects has been studied by Chiang et al. (2003) and Marcus et al. (2011). de la Fuente Marcos & de la Fuente Marcos (2018) perform a systematic search for statistically significant pairs and groups of dynamically correlated objects through those with a semi-major axis greater than 25 AU, applying a technique that uses the angular separations of orbital poles and perihelia together with the differences in time of perihelion passage to single out pairs of relevant objects from which groupings can eventually be uncovered. They confirm the reality of the candidate collisional family of TNOs associated with the pair 2000 FC_8 – 2000 GX_{146} and initially proposed by Chiang (2002). They find four new possible collisional families of TNOs associated with the pairs (134860) 2000 OJ_{67} – 2001 UP_{18}, 2003 UT_{291} – 2004 VB_{131}, 2002 CU_{154} – 2005 CE_{81} and 2003 HF_{57} – 2013 GG_{137}. They find several unbound TNOs that may have a common origin, the most significant ones are (135571) 2002 GG_{32} – (160148) 2001 KV_{76} and 2005 GX_{206} – 2015 BD_{519}.

In (Kuznetsov et al., 2021) performed a search for statistically significant pairs and groups of dynamically correlated objects through those with a semi-major axis greater than 30 AU, applying a novel technique that uses Kholshevnikov metrics (Kholshevnikov et al., 2016, 2020) in the space of Keplerian orbits. Found 27 pairs of TNOs in close orbits, 22 pairs in which one of the TNO is binary, and 11 pairs of binary trans-Neptunian objects. All pairs belong to cold classical Kuiper belt objects. Among the dynamically cold population of the classical Kuiper belt, during the evolution of the protoplanetary disk and the migration of planets, conditions are implemented for the preservation of close binary or contact TNOs with components of approximately equal masses (Nesvorný & Vokrouhlický, 2019). On the other hand, the evolution of wide binary trans-Neptunian objects turns out to be unstable due to frequent encounters with other TNOs, which lead to the decay of binary systems (Campbell, 2021) and the formation of TNO pairs in close orbits.

We perform a study of the dynamical evolution of pairs of TNOs in which one of the component is binary. This paper is organized as follows. Section 2 reviews the methods which we used to search for TNOs with close orbits, research the dynamical evolution of TNOs, and estimate the age of the TNO pairs. Some

pairs found by our approach are presented in Section 3. In Section 4, we discuss the results and summarize our conclusions.

2. Methods

We have used natural metrics $\varrho(\mathcal{E}_1, \mathcal{E}_2)$ in the space of Keplerian orbits (Kholshevnikov et al., 2016, 2020) to search for TNOs with close orbits. Here Keplerian orbits $\mathcal{E}_s$ are points in a five-dimensional space of orbits (the position on the orbit is omitted). Let us denote by a, p, e, i, ω, Ω the semi-major axis, semi-latus rectum, eccentricity, inclination, argument of the pericentre and longitude of the ascending node of the orbit, respectively.

The metric ϱ_2 defines the distance between two orbits in the five-dimensional space of Keplerian orbits (Kholshevnikov et al., 2016)

$$\varrho_2^2 = (1+e_1^2)p_1 + (1+e_2^2)p_2 - 2\sqrt{p_1 p_2}(\cos I + e_1 e_2 \cos P), \tag{1}$$

here indices 1 and 2 correspond to orbital elements of the first and second bodies, respectively,

$$\cos I = c_1 c_2 + s_1 s_2 \cos \Delta,$$

$$\cos P = s_1 s_2 \sin\omega_1 \sin\omega_2 +$$

$$(\cos\omega_1 \cos\omega_2 + c_1 c_2 \sin\omega_1 \sin\omega_2)\cos\Delta +$$

$$(c_2 \cos\omega_1 \sin\omega_2 - c_1 \sin\omega_1 \cos\omega_2)\sin\Delta,$$

$$c = \cos i, \quad s = \sin i, \quad \Delta = \Omega_1 - \Omega_2.$$

The metric ϱ_5 defines the distance in the three-dimensional factor-space of the positional elements. Its elements are classes of orbits with fixed p, e, i and all possible values of ω and Ω (Kholshevnikov et al., 2016)

$$\varrho_5^2 = (1+e_1^2)p_1 + (1+e_2^2)p_2 - 2\sqrt{p_1 p_2}\{e_1 e_2 + \cos(i_1 - i_2)\}. \tag{2}$$

The metric ϱ_2 shows the current distance between the Keplerian orbits. The metric ϱ_5 gives the minimum distance between the orbits among all possible positions of the nodes and pericenter of the orbits. Analyzing the metrics will help identify candidates for young pairs. The positions of the lines of nodes and apses of the TNO orbits in young pairs should be close because the orientation of the orbits has changed slightly since the formation of the pair due to the secular drift of nodes and pericenter. If the metrics ϱ_2 and ϱ_5 are small (for TNO pair with binary, one can limit ourselves to 0.12 $\mathrm{AU}^{1/2}$) and have close values (e.g. $\varrho_2 - \varrho_5 < 0.025$ $\mathrm{AU}^{1/2}$), then such a pair of TNOs can be considered a candidate for young pair (e.g Kuznetsov et al., 2020).

We have used both numbered and multiopposition objects from the Asteroids Dynamic Site (AstDyS, https://newton.spacedys.com/astdys/). Epoch of the orbital elements is MJD 58800 (00^h 00^m 00.000^s BDT 13.11.2019) depending

on the used sets of orbital elements from the AstDyS. The metrics ϱ_2 (1) and ϱ_5 (2) have been calculated to search for TNOs pairs with close orbits.

The dynamic evolution of TNO pairs was studied in two stages. In the first step, to find close approaches of TNOs in pairs in the past and, therefore, estimate the age of the pairs, we have performed numerical integrations of the orbits of TNOs in pairs backward in time (a time span of 10 Myr) with the code known as Orbit9 (the OrbFit Software Package, http://adams.dm.unipi.it/orbfit/ (Orbfit Consortium, 2011)). Orbit9 software allows us to estimate the maximum Lyapounov Characteristic Exponent (LCE). We estimated the LCE for the cold classical Kuiper belt to be 0.1 Myr that makes it possible to study the evolution of nominal orbits over several million years. The numerical integrations were made taking the nominal orbits given by AstDyS database as initial conditions. The eight major planets and the dwarf planet Pluto were integrated consistently. The mean ecliptic of J2000.0 was taken as reference plane for the output. We used heliocentric coordinates.

The standard methods for determining the age of pairs of small bodies in close orbits include analysis of 1) low relative-velocity close encounters of objects (see, e.g. Pravec et al., 2019), 2) the minimum distances between the orbits of objects (see, e.g. Kuznetsov et al., 2020), 3) simultaneous approaches of node lines and apse lines of objects orbits (see, e.g. Rosaev & Plávalová, 2017).

The analysis of simultaneous approaches of the lines of nodes and apse of the TNO orbits can be considered as a special case of a more general method using the analysis of the minimum distances between the TNO orbits, for example, using the Kholshevnikov metrics. When analyzing the simultaneous approaches of the lines of nodes and lines of the apses, only two elements are used — the longitude of the ascending node and the argument of the pericenter. At the same time, the estimate of the minimum distance between the orbits is calculated based on five Keplerian elements — the semi-major axis, eccentricity, inclination, longitude of the ascending node, and the argument of the pericenter. Since at the moment of pair formation, the orbits of the objects are close, the difference in the longitudes of the ascending nodes $\Delta\Omega$ and the difference in the arguments of the pericenter Δg should vanish simultaneously with the attainment of a minimum by the metric ϱ_2.

The condition of convergence of orbits does not yet guarantee the convergence of objects moving in these orbits. Therefore, to estimate the age of pairs, it is also necessary to analyze the possibility of the onset of low relative-velocity close encounters, at which the distance between objects r_{rel} is comparable to the radius of the Hill sphere R_H of a more massive body, and the relative velocity v_{rel} is of the order of the escape velocity V_{esc} relative to a more massive body. Pravec et al. (2019) used the criteria for low-speed encounters for asteroids in the main asteroid belt: $r_{rel} < (5 \text{ or } 10)R_H$, $v_{rel} < (2 \text{ or } 4)V_{esc}$, where V_{esc} is the escape velocity on the surface of a more massive body. The narrower limits were used for better converging orbits (e.g., younger ones, or those in non-chaotic

zones of the main asteroid belt), while the loosened limits were typically used for pairs with the orbits affected by some orbital chaoticity.

For each close approach of TNOs in pair we determined the relative distance r_{rel} between TNOs and relative velocity v_{rel}, as well as the Hill sphere radius R_H and escape velocity V_{esc} of the primary body. The radius of the Hill sphere was estimated as:

$$R_H = \frac{1}{2} r_1 D_1 \left(\frac{4\pi}{9} \frac{G\rho_1}{\mu} \right)^{1/3}, \tag{3}$$

where r_1 is the heliocentric distance of the primary's TNO, D_1 is its diameter, ρ_1 is its bulk density, G is the gravitational constant and μ is the gravitational parameter of the Sun. The escape velocity of primary body for relative distance r_{rel} was estimated as:

$$V_{esc} = \sqrt{\frac{\pi}{3} \frac{G D_1^3 \rho_1}{r_{rel}}}. \tag{4}$$

The diameter D of the TNO can be estimated from the absolute magnitude H and the geometric albedo p_v (Bowell et al., 1989):

$$D = 1329\,\mathrm{km}\, 10^{-H/5} \frac{1}{\sqrt{p_v}}. \tag{5}$$

We need to know the physical parameters of the TNO to estimate the radius of the Hill sphere R_H (3) and the escape velocity V_{esc} (4). Since the objects included in the studied TNO pairs belong to the dynamically cold population of the classical Kuiper belt and have dimensions not exceeding several hundred km, we used the same density values $\rho = 0.5$ g cm^{-3} and geometric albedo $p_v = 0.13$ for all TNOs (Muller et al. ., 2020).

Estimates of the single TNO density range from 0.5 to 2 g cm^{-3} (Lacerda & Jewitt, 2007; Grundy et al., 2008; Fernández, 2020) and grow with an increase in the TNO diameter. For TNOs several hundred km in size, the density estimates are $0.5 - 0.6$ g cm^{-3} (Lacerda & Jewitt, 2007; Grundy et al., 2008; Fernández, 2020). We used the minimum density value $\rho = 0.5$ g cm^{-3}, which will give the minimum estimates for the radius of the Hill sphere R_H (3) and the escape velocity V_{esc} (4). If the density value is 2 g cm^{-3}, the value of the radius of the Hill sphere R_H will be underestimated by $4^{1/3} \approx 1.6$ times, and the value of the escape velocity V_{esc} by $4^{1/2} = 2$ times. This can be taken into account when establishing the criteria for close encounters of the TNO pair. We used the physical parameters of binary TNOs published in (Grundy et al., 2009, 2011, 2019)

3. Results

3.1. Search for pairs with binary TNO in close orbits

We used the osculating orbital elements from the AstDyS database for the epoch MJD 58800, to calculate the Kholshevnikov metrics ϱ_2 (1) and ϱ_5 (2). The following criteria were chosen for the selection of young pairs of TNOs: $\varrho_2 \leq 0.121$ AU$^{1/2}$ ($\varrho_2^2 \leq 0.0146$ AU $= 2.2 \cdot 10^6$ km), $\varrho_5 < 0.12$ AU$^{1/2}$ ($\varrho_5^2 < 0.0144$ AU $= 2.2 \cdot 10^6$ km) and $\varrho_2 - \varrho_5 < 0.025$ AU$^{1/2}$ ($(\varrho_2 - \varrho_5)^2 < 0.000625$ AU $= 9.4 \cdot 10^4$ km). The criteria for the metrics ϱ_2 and ϱ_5 correspond to two or three values of the Hill sphere radius for TNO. The closeness of the metrics ϱ_2 and ϱ_5 may indicate the youth of a pair of TNOs (after forming a pair, the orbits have not yet had time to disperse due to the precession of nodes and pericenter). However, this is only a necessary condition for the youth of the pairs because the precession of the nodes and pericenter of the orbits has a conditionally periodic type.

We selected 21 pairs of TNOs with binaries satisfying the first two conditions: $\varrho_2 \leq 0.121$ AU$^{1/2}$ and $\varrho_5 < 0.12$ AU$^{1/2}$ (see Tab. 1). Ten pairs of TNOs (in bold in Tab. 1) satisfy all three conditions. Tab. 2 gives the orbital elements for the epoch MJD 58800, here M_0 is the mean anomaly, and H is the absolute magnitude of TNO. Analysis of the Tab. 2 shows that all detected TNOs included in the pairs belong to the dynamically cold population of the classical Kuiper belt, which is characterized by orbits with semi-major axes from 42 to 45 AU, eccentricities not exceeding 0.1, and inclinations not exceeding 5° (Gladman et al., 2008; Kavelaars et al., 2008). The minimum value of the semi-major axis for TNO 2003 UN_{284} is 42.4 AU, the maximum value for 2015 RP_{280} is 45.5 AU. The maximum eccentricity of 0.105 has TNO 2012 HE_{85}. The maximum inclination of 3.8° is achieved for TNO 2003 QY_{90}.

3.2. Dynamic evolution of pairs with binary TNO in close orbits

We carried out a numerical simulation of the orbital evolution in the time interval of 10 Myr into the past for all selected pairs with binary TNO (see Tab. 1). The nominal values of the osculating elements of the TNO orbits from the AstDyS base for the epoch MJD 58800 (see Tab. 2) were chosen as the initial ones.

Tab. 3 shows the minimum values of the metric ϱ_{2min} and the corresponding moments t_ϱ, measured in years from the epoch MJD 58800. Tab. 3 gives the pairs in the same order as in Tab. 1. For 13 pairs, the minimum value of the metric is $\varrho_{2min} < 0.07$ AU$^{1/2}$ ($\varrho_{2min}^2 < 0.0049$ AU $= 7.33 \cdot 10^5$ km). The minimum value $\varrho_{2min} = 0.0057$ AU$^{1/2}$ ($\varrho_{2min}^2 = 3.25 \cdot 10^{-5}$ AU $= 4.86 \cdot 10^3$ km) was recorded for the pair TNO (469610) 2004 HF_{79} – 2013 UL_{17}.

The moments t_ϱ corresponding to the minima of the metrics are not the moments of TNO pairs formation since, in addition to the approach of the orbits, the objects must also encounter. A search was carried out for low relative-velocity close encounters of TNOs included in pairs in close orbits (see Tab. 1),

Table 1. TNOs pairs with binaries.

Binary TNO	TNO	ϱ_2 [AU$^{1/2}$]	ϱ_5 [AU$^{1/2}$]
2005 GD$_{187}$	**2001 OG$_{109}$**	0.0731	0.0664
(275809) 2001 QY$_{297}$	**2015 VB$_{169}$**	0.0732	0.0654
(469610) 2004 HF$_{79}$	**1997 CT$_{29}$**	0.0791	0.0546
2005 GD$_{187}$	2015 VV$_{170}$	0.0918	0.0664
2002 VD$_{131}$	**(505446) 2013 SP$_{99}$**	0.0976	0.0945
2004 HK$_{79}$	2015 VB$_{171}$	0.0996	0.0657
2006 JV$_{58}$	2004 KF$_{19}$	0.0998	0.0707
(275809) 2001 QY$_{297}$	**2006 HB$_{123}$**	0.1039	0.0856
2003 QY$_{90}$	**2002 CU$_{154}$**	0.1049	0.0957
2015 RP$_{280}$	**2012 HE$_{85}$**	0.1083	0.0933
2000 CF$_{105}$	**2015 GJ$_{57}$**	0.1110	0.0977
2003 UN$_{284}$	1996 TK$_{66}$	0.1124	0.0834
2015 VW$_{168}$	**2013 UL$_{17}$**	0.1133	0.0989
2004 HK$_{79}$	2004 VB$_{131}$	0.1135	0.0674
(505447) 2013 SQ$_{99}$	2004 HE$_{79}$	0.1141	0.0872
2004 HK$_{79}$	2015 GA$_{57}$	0.1144	0.0199
2005 GD$_{187}$	(420356) Praamzius	0.1148	0.0889
2004 PW$_{117}$	2015 GT$_{57}$	0.1174	0.0978
2002 VD$_{131}$	**2002 CZ$_{224}$**	0.1184	0.0983
2004 PW$_{117}$	2013 TL$_{172}$	0.1188	0.0265
(469610) 2004 HF$_{79}$	2013 UL$_{17}$	0.1209	0.0837

based on the results of numerical modeling. The integration interval was 10 Myr in the past. The nominal TNO orbits from the AstDyS database were used. The criteria for the search for low relative-velocity close encounters were chosen taking into account the uncertainty of the density ρ and albedo p_v of the TNO: $r_{rel} < 3\,R_H$, $v_{rel} < 4\,V_{esc}$. On the considered time interval, for none of the pairs, the conditions of low relative-velocity close encounters were fulfilled.

Tab. 4 shows information about the approaches of TNO to distances less than $10\,R_H$ (here t_r is the moment at which the minimum distance is reached). There are only six such pairs. The closest approach of the TNOs to $r_{rel} = 2.8\,R_H$ was recorded for the pair TNO 2005 GD$_{187}$ – (420356) Praamzius as the minimum relative velocity $v_{rel} = 167\,V_{esc}$. However, this velocity is 42 times higher than the value corresponding to the low relative-velocity close encounters. We can conclude that in the considered interval of 10 Myr, the encounters of TNOs to distances of less than $10\,R_H$ is possible. Still, high speeds of relative motion show that the moments of close approaches of TNOs are most likely not the moments of formation of pairs of TNOs in close orbits.

Table 2. Orbital elements of TNOs pairs with binaries at epoch MJD58800.0.

TNO	a [AU]	e	i [°]	Ω [°]	g [°]	M_0 [°]	H [mag]
(275809) 2001 QY_{297}	44.117	0.085	1.547	108.75	129.91	82.73	5.58
(420356) Praamzius	42.531	0.011	1.101	314.26	1.46	182.67	5.60
(469610) 2004 HF_{79}	43.598	0.034	1.485	76.64	193.70	338.79	6.42
(505446) 2013 SP_{99}	43.805	0.062	0.791	71.92	250.51	52.07	7.36
(505447) 2013 SQ_{99}	44.181	0.094	3.469	51.96	177.15	142.02	6.57
1996 TK_{66}	42.565	0.016	3.315	44.59	211.26	136.86	6.37
1997 CT_{29}	43.643	0.034	1.014	74.52	210.21	239.25	6.56
2000 CF_{105}	43.684	0.032	0.528	56.47	56.74	31.87	6.94
2001 OG_{109}	43.759	0.018	0.540	332.70	1.58	355.71	8.15
2002 CU_{154}	43.652	0.056	3.355	108.98	41.12	9.66	6.91
2002 CZ_{224}	44.853	0.065	1.687	66.48	263.82	183.34	6.95
2002 VD_{131}	45.006	0.066	0.851	84.62	239.38	70.85	6.57
2003 QY_{90}	42.922	0.047	3.762	104.05	41.84	198.99	6.48
2003 UN_{284}	42.411	0.004	3.069	35.99	277.08	121.47	7.42
2004 HE_{79}	44.664	0.104	3.085	62.82	164.96	17.20	7.42
2004 HK_{79}	44.179	0.085	1.943	69.02	182.48	340.69	6.92
2004 KF_{19}	44.470	0.070	0.107	329.90	277.11	2.75	6.92
2004 PW_{117}	43.868	0.055	1.862	81.35	76.57	167.84	6.34
2004 VB_{131}	44.027	0.076	1.745	50.37	207.53	153.34	6.55
2005 GD_{187}	42.971	0.022	0.707	354.40	333.59	200.83	7.21
2006 HB_{123}	44.448	0.097	1.801	115.76	128.02	5.93	7.04
2006 JV_{58}	45.323	0.067	0.318	144.15	95.97	11.25	6.63
2012 HE_{85}	44.926	0.105	3.016	235.00	38.36	12.37	9.04
2013 TL_{172}	43.833	0.058	1.791	95.04	78.81	197.66	6.85
2013 UL_{17}	42.712	0.030	1.831	82.27	211.10	86.11	8.17
2015 GA_{57}	44.084	0.082	1.938	56.15	184.95	333.43	7.96
2015 GJ_{57}	43.477	0.027	1.328	82.03	40.14	85.44	7.69
2015 GT_{57}	44.065	0.067	2.285	92.10	72.51	37.83	8.55
2015 RP_{280}	45.495	0.096	3.489	232.41	45.34	83.23	7.51
2015 VB_{169}	43.867	0.083	2.083	104.86	130.78	176.87	7.91
2015 VB_{171}	43.677	0.083	2.391	83.55	172.08	155.30	7.92
2015 VV_{170}	43.065	0.031	0.908	30.91	288.17	93.42	9.06
2015 VW_{168}	42.539	0.045	1.954	96.71	199.17	112.82	8.29

3.3. Analysis of approaches of TNO and their orbits

When assessing the age of pairs of small bodies in close orbits, it is interesting to compare the moments of the approach of orbits, lines of nodes and apsides, and the objects themselves in orbits. At the moment of pair formation, all estimated distances between orbits and bodies should be small. Let us compare the moments of the approach of orbits (see Tab. 3), nodes and pericenter of orbits, as well as objects in orbits (see Tab. 4) for six TNOs experiencing close

Table 3. Minimum values of the metric ϱ_2 and the moments of their occurrence t_ϱ.

Binary TNO	TNO	ϱ_{2min} [AU$^{1/2}$]	t_ϱ [years]
2005 GD_{187}	2001 OG_{109}	0.036	−2840
(275809) 2001 QY_{297}	2015 VB_{169}	0.062	−259660
(469610) 2004 HF_{79}	1997 CT_{29}	0.056	−53400
2005 GD_{187}	2015 VV_{170}	0.059	−6417930
2002 VD_{131}	(505446) 2013 SP_{99}	0.056	−9570
2004 HK_{79}	2015 VB_{171}	0.081	−124000
2006 JV_{58}	2004 KF_{19}	0.057	−246070
(275809) 2001 QY_{297}	2006 HB_{123}	0.063	−22060
2003 QY_{90}	2002 CU_{154}	0.069	−80050
2015 RP_{280}	2012 HE_{85}	0.067	−40850
2000 CF_{105}	2015 GJ_{57}	0.102	−13740
2003 UN_{284}	1996 TK_{66}	0.086	−5006740
2015 VW_{168}	2013 UL_{17}	0.081	−801640
2004 HK_{79}	2004 VB_{131}	0.079	−8040
(505447) 2013 SQ_{99}	2004 HE_{79}	0.070	−7297160
2004 HK_{79}	2015 GA_{57}	0.057	−9421100
2005 GD_{187}	(420356) Praamzius	0.084	−1157230
2004 PW_{117}	2015 GT_{57}	0.020	−7254560
2002 VD_{131}	2002 CZ_{224}	0.107	−1970310
2004 PW_{117}	2013 TL_{172}	0.056	−7689270
(469610) 2004 HF_{79}	2013 UL_{17}	0.0057	−4159900

Table 4. The closest approach moments t_r of TNO in pairs under the condition $r_{rel} < 10\,R_H$.

Binary TNO	TNO	r_{rel} [R_H]	R_H [10^3 km]	v_{rel} [V_{esc}]	V_{esc} [m s^{-1}]	t_r [years]
(469610) 2004 HF_{79}	1997 CT_{29}	8.6	439	213	0.26	−3714950
2005 GD_{187}	2015 VV_{170}	4.5	307	232	0.25	−3463500
2002 VD_{131}	(505446) 2013 SP_{99}	9.4	428	596	0.22	−2230280
2006 JV_{58}	2004 KF_{19}	8.7	389	921	0.23	−4696470
2000 CF_{105}	2015 GJ_{57}	6.4	356	684	0.23	−4590180
2005 GD_{187}	(420356) Praamzius	2.8	631	167	0.65	−6882190

encounters. At the moment of pair formation, the conditions $t_r \approx t_\varrho$, $\Delta\Omega \approx 0$, and $\Delta g \approx 0$ must be met. The Tab. 5 gives the moments t_Δ corresponding to the condition $\Delta\Omega \approx 0$ and $\Delta g \approx 0$ for six pairs from the Tab. 4.

Pair TNOs (469610) 2004 HF_{79} – 1997 CT_{29}. The minimum distance between TNOs is fixed at the moment of $t_r = -3714950$ years. The value of the metric ϱ_2 reaches its minimum at $t_\varrho = -53400$ years. The evolution of the metric ϱ_2 with time shows that the metric, on average, monotonically increases in

Table 5. The moments t_Δ corresponding to the condition $\Delta\Omega \approx 0$ and $\Delta g \approx 0$.

Binary TNO	TNO	t_Δ [Myr]
(469610) 2004 HF_{79}	1997 CT_{29}	-3.2
2005 GD_{187}	2015 VV_{170}	-3.0
		-4.2
		-6.8
		$-9.4 - -9.0$
2002 VD_{131}	(505446) 2013 SP_{99}	$-0.7 - -0.5$
2006 JV_{58}	2004 KF_{19}	-0.7
2000 CF_{105}	2015 GJ_{57}	-1.5
2005 GD_{187}	(420356) Praamzius	-5.6
		-6.4

the past from the moment of minimum. Analysis of the change in the differences in the longitudes of the ascending nodes $\Delta\Omega$ and the arguments of the pericenter Δg shows that both differences are close to zero in the vicinity of the time 3.2 Myr in the past and in the present. Since the methods used give significantly different estimates of the pair's age, we did not find low relative-velocity close encounters of TNOs in the considered time interval, and we conclude that the age of the pair exceeds 10 Myr.

Pair TNOs 2005 GD_{187} – 2015 VV_{170}. The minimum distance between TNOs is fixed at the moment of $t_r = -3463500$ years. The value of the metric ϱ_2 reaches a minimum at $t_\varrho = -6417930$ years. The evolution of the metric ϱ_2 with time shows that the metric remains small for the entire considered interval. Its value does not exceed 0.13 $AU^{1/2}$. Analysis of the differences in the longitudes of the ascending nodes $\Delta\Omega$ and the arguments of the pericenter Δg shows that both differences are close to zero in the vicinity of 3, 4.2, 6.8, $9.0 - 9.4$ Myr in the past. The minimum distances between TNOs and between their orbits are achieved in the vicinity of the moments of the approach of the lines of nodes and apsides. However, we did not find low relative-velocity close encounters of TNOs in the considered time interval. Most likely, the age of the pair exceeds 10 Myr.

Pair TNOs 2002 VD_{131} – (505446) 2013 SP_{99}. The minimum distance between TNOs is fixed at the moment of $t_r = -2230280$ years. The value of the metric ϱ_2 reaches its minimum at $t_\varrho = -9570$ years. The evolution of the metric ϱ_2 with time shows that the distance between the orbits increases into the past, reaching 0.9 $AU^{1/2}$. Analysis of the change in the differences in the longitudes of the ascending nodes $\Delta\Omega$ and the arguments of the pericenter Δg shows that both differences are close to zero about $0.5 - 0.7$ Myr ago. The methods used give significantly different estimates of the pair's age. We did not detect any low relative-velocity close encounters of TNOs. Most likely, the age of the pair exceeds 10 Myr.

Pair TNOs 2006 JV_{58} – 2004 KF_{19}. The minimum distance between TNOs is fixed at the moment of $t_r = -4696470$ years. The value of the metric ϱ_2 reaches a minimum at $t_\varrho = -246070$ years. Starting from 1 Myr ago, the metric ϱ_2 grows, reaching the value 0.7 $\mathrm{AU}^{1/2}$ at the end of the considered interval. Analysis of the change in the differences in the longitudes of the ascending nodes $\Delta\Omega$ and the arguments of the pericenter Δg shows that both differences are close to zero about 0.7 Myr ago. The methods used give significantly different estimates of the pair's age. We did not detect any low relative-velocity close encounters of TNOs. Most likely, the age of the pair exceeds 10 Myr.

Pair TNOs 2000 CF_{105} – 2015 GJ_{57}. The minimum distance between TNOs is fixed at the moment of $t_r = -4590180$ years. The value of the metric ϱ_2 reaches a minimum at $t_\varrho = -13740$ years. Starting from 2 Myr ago, the metric ϱ_2 grows, reaching the value 0.5 $\mathrm{AU}^{1/2}$ at the end of the considered interval . Analysis of the change in the differences in the longitudes of the ascending nodes $\Delta\Omega$ and the arguments of the pericenter Δg shows that both differences are close to zero about 1.5 Myr ago. The methods used give significantly different estimates of the pair's age. We did not detect any low relative-velocity close encounters of TNOs. Most likely, the age of the pair exceeds 10 Myr.

Pair TNOs 2005 GD_{187} – (420356) Praamzius. The minimum distance between TNOs is fixed at the moment of $t_r = -6882190$ years. The value of the metric ϱ_2 reaches a minimum at $t_\varrho = -1157230$ years. Starting from 2 Myr ago, the metric ϱ_2 grows, reaching the value 0.25 $\mathrm{AU}^{1/2}$ at the end of the considered interval. Analysis of the change in the differences in the longitudes of the ascending nodes $\Delta\Omega$ and the arguments of the pericenter Δg shows that both differences are close to zero in the vicinity of 5.6 and 6.4 Myr ago. The minimum distances between TNOs and between their orbits are achieved in the vicinity of the moments of the approach of the lines of nodes and apsides. However, we did not find low relative-velocity close encounters of TNOs in the considered time interval. Most likely, the age of the pair exceeds 10 Myr.

4. Discussion and conclusions

We performed a search for TNO pairs, in which one of the objects is binary, among all numbered objects and objects observed in more than one opposition. The measure of the proximity of the orbits was the Kholshevnikov metric ϱ_2. We selected 21 pairs of TNOs in close orbits to study the dynamic evolution and estimate the age of the pairs. All pairs belong to the dynamically cold population of the classical Kuiper belt. In this region, favorable conditions are formed for the preservation of close binary TNO systems (Nesvorný & Vokrouhlický, 2019). However, at the same time, wide TNO binary systems disintegrate due to encounters with other objects (Campbell, 2021). The most probable source of TNO pairs, in which one of the objects is binary, is the decay of ternary and multiple TNO systems.

The analysis of dynamic evolution based on nominal orbits over 10 Myr, carried out using three approaches: the search for the approaches of orbits, lines of nodes and apsides, the TNOs themselves in orbits, showed ambiguous results. As a rule, estimates of the age of pairs obtained by different methods gave significantly different estimates. This may indicate that the age of the pairs exceeds 10 Myr.

An approach based on the study of the probabilistic evolution of a pair of TNOs should play an important role in increasing the reliability of estimates of the age of TNO pairs. We plan to use this technic in our future studies.

The interval of 10 Myr is relatively short for TNO because, during this time, objects of the classical Kuiper belt make only $33-36$ thousand periods in orbit. For comparison, young pairs in the main asteroid belt are pairs with an age of up to 2 Myr. During this time, asteroids make $400-600$ thousand the orbital periods. In the future, it is planned to increase the integration interval to 200 Myr. On such a long interval, the manifestation of stochastic properties of the TNO dynamic evolution is inevitable; therefore, the main methods used to estimate the age of pairs should be methods that estimate the distance between orbits, their nodes, and pericenters.

Acknowledgements. This work has been supported by the Russian Ministry of Science and Higher Education via the State Assignment Project FEUZ-2020-0038.

References

Benz, W. & Asphaug, E., Catastrophic Disruptions Revisited. 1999, *Icarus*, **142**, 5, DOI: 10.1006/icar.1999.6204

Boehnhardt, H. 2004, *Split comets*, ed. M. C. Festou, H. U. Keller, & H. A. Weaver, 301

Bottke, William F., J., Vokrouhlický, D., Rubincam, D. P., & Nesvorný, D., The Yarkovsky and Yorp Effects: Implications for Asteroid Dynamics. 2006, *Annual Review of Earth and Planetary Sciences*, **34**, 157, DOI: 10.1146/annurev.earth.34.031405.125154

Bowell, E., Hapke, B., Domingue, D., et al., Application of photometric models to asteroids. 1989, in *Asteroids II*, ed. R. P. Binzel, T. Gehrels, & M. S. Matthews, 524–556

Brown, M. E., Barkume, K. M., Ragozzine, D., & Schaller, E. L., A collisional family of icy objects in the Kuiper belt. 2007, *Nature*, **446**, 294, DOI: 10.1038/nature05619

Campbell, H., Stability and Formation of Ultra-Wide Kuiper Belt Binaries. 2021, in AAS/Division of Dynamical Astronomy Meeting, Vol. **53**, *AAS/Division of Dynamical Astronomy Meeting*, 501.04

Chiang, E. I., A Collisional Family in the Classical Kuiper Belt. 2002, *Astrophys. J. Lett.*, **573**, L65, DOI: 10.1086/342089

Chiang, E. I., Lovering, J. R., Millis, R. L., et al., Resonant and Secular Families of the Kuiper Belt. 2003, *Earth Moon and Planets*, **92**, 49, DOI: 10.1023/B:MOON.0000031924.20073.d0

de la Fuente Marcos, C. & de la Fuente Marcos, R., Far from random: dynamical groupings among the NEO population. 2016, *Mon. Not. R. Astron. Soc.*, **456**, 2946, DOI: 10.1093/mnras/stv2885

de la Fuente Marcos, C. & de la Fuente Marcos, R., Dynamically correlated minor bodies in the outer Solar system. 2018, *Mon. Not. R. Astron. Soc.*, **474**, 838, DOI: 10.1093/mnras/stx2765

Deienno, R., Gomes, R. S., Walsh, K. J., Morbidelli, A., & Nesvorný, D., Is the Grand Tack model compatible with the orbital distribution of main belt asteroids? 2016, *Icarus*, **272**, 114, DOI: 10.1016/j.icarus.2016.02.043

Fernández, J. 2020, *Introduction: The Trans-Neptunian zone: past, present and future*, ed. D. Prialnik, M. A. Barucci, & L. Young, 1–22

Gladman, B., Marsden, B. G., & Vanlaerhoven, C. 2008, *Nomenclature in the Outer Solar System*, ed. M. A. Barucci, H. Boehnhardt, D. P. Cruikshank, A. Morbidelli, & R. Dotson, 43

Granvik, M., Morbidelli, A., Vokrouhlický, D., et al., Escape of asteroids from the main belt. 2017, *Astronomy and Astrophysics*, **598**, A52, DOI: 10.1051/0004-6361/201629252

Grundy, W. M., Noll, K. S., Buie, M. W., et al., Mutual orbits and masses of six transneptunian binaries. 2009, *Icarus*, **200**, 627, DOI: 10.1016/j.icarus.2008.12.008

Grundy, W. M., Noll, K. S., Nimmo, F., et al., Five new and three improved mutual orbits of transneptunian binaries. 2011, *Icarus*, **213**, 678, DOI: 10.1016/j.icarus.2011.03.012

Grundy, W. M., Noll, K. S., Roe, H. G., et al., Mutual orbit orientations of transneptunian binaries. 2019, *Icarus*, **334**, 62, DOI: 10.1016/j.icarus.2019.03.035

Grundy, W. M., Noll, K. S., Virtanen, J., et al., (42355) Typhon Echidna: Scheduling observations for binary orbit determination. 2008, *Icarus*, **197**, 260, DOI: 10.1016/j.icarus.2008.04.004

Jacobson, S. A., Multiple origins of asteroid pairs. 2016, in IAU Symposium, Vol. **318**, *Asteroids: New Observations, New Models*, ed. S. R. Chesley, A. Morbidelli, R. Jedicke, & D. Farnocchia, 55–65

Jacobson, S. A. & Scheeres, D. J., Dynamics of rotationally fissioned asteroids: Source of observed small asteroid systems. 2011, *Icarus*, **214**, 161, DOI: 10.1016/j.icarus.2011.04.009

Kavelaars, J., Jones, L., Gladman, B., Parker, J. W., & Petit, J. M. 2008, *The Orbital and Spatial Distribution of the Kuiper Belt*, ed. M. A. Barucci, H. Boehnhardt, D. P. Cruikshank, A. Morbidelli, & R. Dotson, 59

Kholshevnikov, K. V., Kokhirova, G. I., Babadzhanov, P. B., & Khamroev, U. H., Metrics in the space of orbits and their application to searching for celestial objects

of common origin. 2016, *Mon. Not. R. Astron. Soc.*, **462**, 2275, DOI: 10.1093/mnras/stw1712

Kholshevnikov, K. V., Shchepalova, A. S., & Jazmati, M. S., On a quotient space of keplerian orbits. 2020, *Vestnik St. Petersburg University: Mathematics*, **53**, 108, DOI: 10.1134/S1063454120010045

Kuznetsov, E. & Safronova, V., Application of metrics in the space of orbits to search for asteroids on close orbits. 2018, *Planet. Space Sci.*, **157**, 22, DOI: 10.1016/j.pss.2018.04.011

Kuznetsov, E. D., Al-Shiblawi, O. M., Gusev, V. D., & Ustinov, D. S., Pairs of Trans-Neptunian Objects with Close Orbits. 2021, in *Lunar and Planetary Science Conference*, Lunar and Planetary Science Conference, 1859

Kuznetsov, E. D., Rosaev, A. E., Plavalova, E., Safronova, V. S., & Vasileva, M. A., A Search for Young Asteroid Pairs with Close Orbits. 2020, *Solar System Research*, **54**, 236, DOI: 10.1134/S0038094620030077

Kuznetsov, E. D. & Vasileva, M. A., On New Members of Asteroid Clusters Similar to Asteroid Pairs. 2019, *Meteoritics & Planetary Science*, **54**, A229, DOI: https://doi.org/10.1111/maps.13346

Lacerda, P. & Jewitt, D. C., Densities of Solar System Objects from Their Rotational Light Curves. 2007, *Astronomical Journal*, **133**, 1393, DOI: 10.1086/511772

Marcus, R. A., Ragozzine, D., Murray-Clay, R. A., & Holman, M. J., Identifying Collisional Families in the Kuiper Belt. 2011, *Astrophys. J.*, **733**, 40, DOI: 10.1088/0004-637X/733/1/40

Nesvorný, D. & Vokrouhlický, D., Binary survival in the outer solar system. 2019, *Icarus*, **331**, 49, DOI: 10.1016/j.icarus.2019.04.030

Orbfit Consortium. 2011, OrbFit: Software to Determine Orbits of Asteroids, Astrophysics Source Code Library

Pravec, P., Fatka, P., Vokrouhlický, D., et al., Asteroid clusters similar to asteroid pairs. 2018, *Icarus*, **304**, 110, DOI: 10.1016/j.icarus.2017.08.008

Pravec, P., Fatka, P., Vokrouhlický, D., et al., Asteroid pairs: A complex picture. 2019, *Icarus*, **333**, 429, DOI: 10.1016/j.icarus.2019.05.014

Pravec, P. & Vokrouhlický, D., Significance analysis of asteroid pairs. 2009, *Icarus*, **204**, 580, DOI: 10.1016/j.icarus.2009.07.004

Pravec, P., Vokrouhlický, D., Polishook, D., et al., Formation of asteroid pairs by rotational fission. 2010, *Nature*, **466**, 1085, DOI: 10.1038/nature09315

Rabinowitz, D., Schwamb, M. E., Hadjiyska, E., Rojo, P., & Tourtellottee, S., A Tale of Two TNOs. in , *EPSC-DPS Joint Meeting 2011*, Vol. **2011**, 1642

Rosaev, A. & Plávalová, E., New members of Datura family. 2017, *Planetary Space Science*, **140**, 21, DOI: 10.1016/j.pss.2017.01.017

Schunová, E., Jedicke, R., Walsh, K. J., et al., Properties and evolution of NEO families created by tidal disruption at Earth. 2014, *Icarus*, **238**, 156, DOI: 10.1016/j.icarus.2014.05.006

Sekanina, Z. & Chodas, P. W., Origin of the Marsden and Kracht Groups of Sunskirting Comets. I. Association with Comet 96P/Machholz and Its Interplanetary Complex. 2005, *Astrophys. J. Suppl. S.*, **161**, 551, DOI: 10.1086/497374

Sekanina, Z. & Chodas, P. W., Fragmentation Hierarchy of Bright Sungrazing Comets and the Birth and Orbital Evolution of the Kreutz System. II. The Case for Cascading Fragmentation. 2007, *Astrophys. J.*, **663**, 657, DOI: 10.1086/517490

Vokrouhlický, D. & Nesvorný, D., Pairs of Asteroids Probably of a Common Origin. 2008, *Astron. J.*, **136**, 280, DOI: 10.1088/0004-6256/136/1/280

Vokrouhlický, D., Pravec, P., Ďurech, J., et al., Detailed Analysis of the Asteroid Pair (6070) Rheinland and (54827) 2001 NQ8. 2017, *Astron. J.*, **153**, 270, DOI: 10.3847/1538-3881/aa72ea

Contrib. Astron. Obs. Skalnaté Pleso **51**, 241 – 248, (2021)
https://doi.org/10.31577/caosp.2021.51.3.241

Trajectory estimation for fresh impacts on Mars

E.D. Podobnaya, O.P. Popova and D.O. Glazachev

Sadovsky Institute of Geosphere Dynamics
Leninsky prospect 38, Moscow, Russia, (E-mail: epodobnaya@gmail.com)

Received: August 1, 2021; Accepted: November 10, 2021

Abstract. Exploration of small craters and craters clusters on Mars allows one to study meteoroid fragmentation details that cannot be detected in terrestrial conditions. It was suggested earlier that the description of a cluster with a scattering ellipse allows one to estimate the meteoroids' trajectory, which is connected with orbital parameters of the impactor. Independent construction of scattering ellipses and comparison with crater ejecta demonstrate the accuracy and find out some problems of this approach.

Key words: meteoroids – Mars – craters – impacts – cluster – fragmentation – strewn fields

1. Introduction

In recent years, about 700 fresh dated meteoroid impact sites were discovered on Mars (Malin et al., 2006; Daubar et al., 2013, 2019). Meteoroid impacts resulted in the formation of single craters and crater fields, with crater sizes up to 50 m.

Due to the more rarefied Mars atmosphere (in comparison with Earth) falling meteoroids are less destroyed. Nevertheless, near half of meteoroids are fragmented in the Martian atmosphere and are forming crater clusters (Daubar et al., 2013, 2019).The comparison of Martian and terrestrial fireballs allows to suggest 40-50% of terrestrial meteoroids would lead to the formation of crater fields on Mars (Hartmann et al., 2018). On Earth, meteoroids are usually observed during a short flight through the atmosphere. In rare cases, their fragments are found as meteorites. Estimates meteoroids properties depend on used fragmentation models calibrated on a small number of events. As Mars surface level corresponds to about 30 km altitude in the Earth atmosphere, crater scattering fields on Mars surface provide a unique opportunity to see the results of less significant fragmentation.

Detailed data for 77 crater fields (clusters) containing from 2 to 465 individual craters, were obtained by HiRISE camera (High Resolution Imaging Science Experiment), which made high resolution images of Mars (Daubar et al., 2013, 2019). The minimum size of craters in clusters is about 1 m due to the resolution of the cameras. The average diameter of craters in various clusters is from 1 to 6 m, the average value for all clusters is 2.5 m. Clusters craters (Fig. 1) can be de-

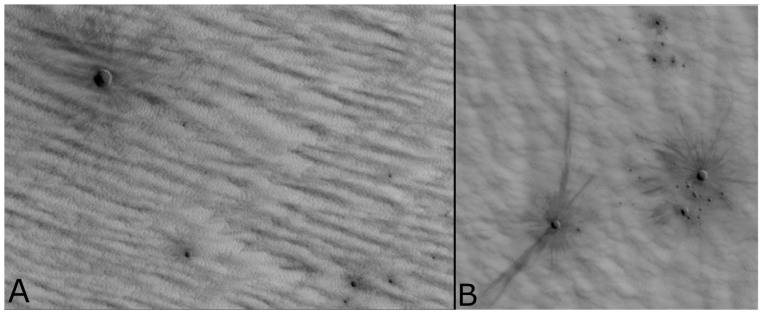

Figure 1. HiRISE images for craters distribution in two clusters under study. A: Cluster ESP_013655_1710. B: Cluster ESP_013800_1820.

scribed by the scattering ellipse, which allows to estimate the parameters of the meteoroid trajectory, for example azimuth and entry angle into the atmosphere.

Destruction of a space object can be a rather complex, multi-stage process. The description of the meteorites scattering field by an ellipse was initially proposed for the case of a single fragmentation. Scattering ellipse parameters depend on the trajectory of the multiply fragmented space object, although possibly in a more complex way. A closer look at the location of the craters within the scattering ellipses may reveal more about the fragmentation process and impactor properties. The size of cluster depends on many factors, including the size of the impactor, its strength and the strength of its fragments, density, the fragmentation process, and others (Ivanov et al., 2008). Cluster study can provide an opportunity to determine these characteristics. Finding the smallest ellipse fitting the cluster is one of the first approaches to describe clusters (Daubar et al., 2019).

2. Scattering ellipses

To describe clusters and obtain various estimates (entry angle, azimuth), Daubar et al. (2019) proposed to fit the minimum ellipse covering 90% of the craters in the cluster. Here scattering ellipses were constructed for 55 clusters, which contain more than 5 craters. It is not clear how sensitive the estimates of the angles and cluster sizes obtained by Daubar et al. (2019) are to the applied method, so we used the same algorithm independently. In addition, we tested several more algorithms and chose the best of them (Podobnaya et al., 2020). First algorithm, called below MVE, is similar to the method applied by Daubar et al. (2019). Minimal square ellipses, which cover 300 random sets of craters (with possible duplication), were built for each cluster. Bootstrap procedure was used for more reliable results and possible incomplete data compensation. Averaged ellipse is used as the result. Next algorithm, called below Stat, is a

statistical ellipse, implemented in Wolfram Mathematica software. Constructed scattering ellipses (Fig. 2) differ from the independent source (Daubar et al., 2019) by ellipse area up to 1.5 times.

The ratio of the ellipse semi-axes was used to determine the meteoroids entry angle. Our estimates made by two methods mentioned above differ by no more than 15°in most cases. Obtained trajectory projection angle (i.e. azimuth without direction) demonstrates not more than 20°difference between MVE, Stat and an independent estimate (Daubar et al., 2019) in most cases. The direction of flight of the meteoroid (azimuth) was determined as the direction from the center of the scattering ellipse along its major axis towards the maximum crater. Azimuths and other angles in this work are counted clockwise from north. The flight direction coincides with an accuracy of 45°in about 80% of cases, and in 10-15% the direction is opposite (depending on the algorithm of the scattering ellipse constructing). In the remaining 5-10% of cases, the main axis of the ellipses is perpendicular to those indicated in Daubar et al. (2019).

3. Scattering ellipses on Earth

As an independent testing, the considered methods of constructing a scattering ellipse (MVE, Stat) were applied to two recent terrestrial scattering fields - the Ozerki and Chelyabinsk meteorites, for which all trajectory parameters are known (Kartashova et al., 2020; Borovička et al., 2013; Popova et al., 2013). The angle of entry into the atmosphere and azimuth were found from the obtained scattering ellipses.

In the case of the Chelyabinsk meteoroid, data of 180 fragments (the maximum fragment weight is 600 kg) were considered (Popova et al., 2013). The obtained estimates of the flight direction coincide with the results obtained by other methods - 283-284°(Popova et al., 2013; Borovička et al., 2013) with an accuracy of several degrees (Fig. 3). For the entry angle into the atmosphere of the Chelyabinsk meteoroid considering scattering ellipses give the angle of 7-8°, with a known estimate of 18°(the angle is measured from the horizontal) (Popova et al., 2013). According to the data of the nearest meteorological stations (Verkhneye Dubrovo, 180 km from Chelyabinsk), the wind speed during the meteoroid flight at altitudes below 20 km did not exceed 15 $\mathrm{m\,s^{-1}}$, and the wind direction was approximately 320-330°(Fig. 3). The difference in the estimates relate to wind influence on small fragments and with incomplete collection of small fragments, the real scattering field was probably wider.

The scattering ellipses obtained from the data of 76 fragments (the maximum fragment mass is 740 g) of the Ozerki meteorite (Popova et al., 2019) were compared with the trajectory found in Kartashova et al. (2020). Our estimates of meteoroid entry angle into the atmosphere (33-35°) correlate poorly with the estimate at 77.6°(from the horizon) (Kartashova et al., 2020). The azimuth of the Ozerki meteoroid flight is also estimated based on the obtained scattering

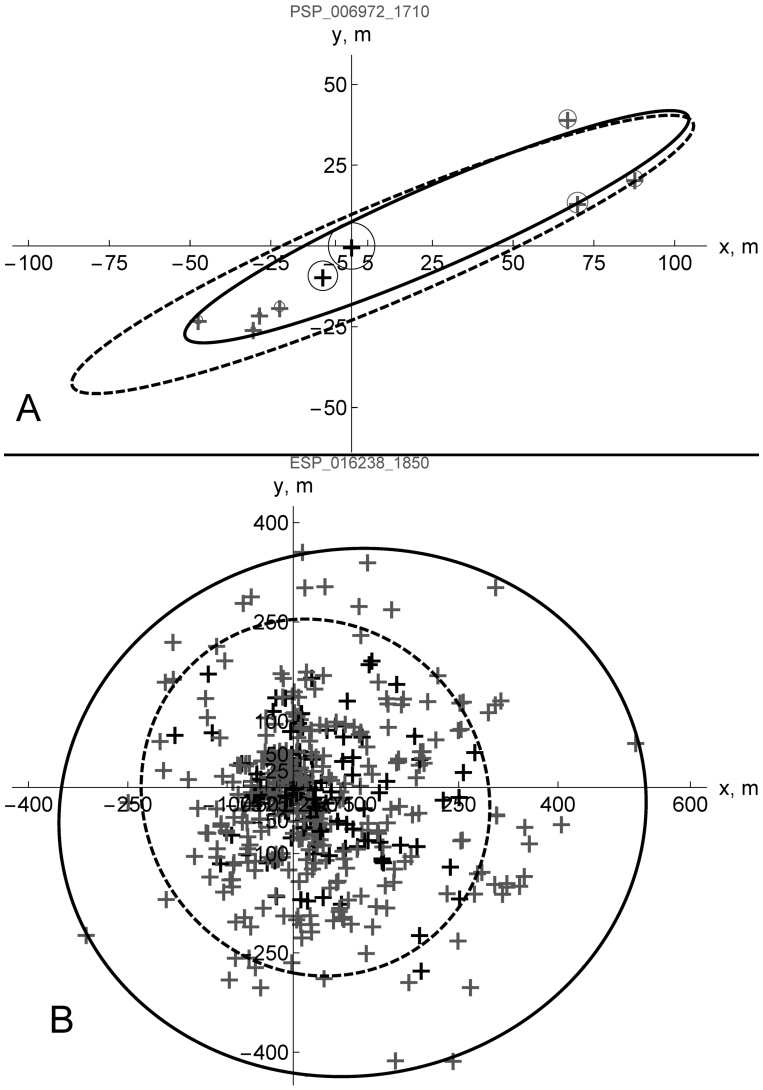

Figure 2. Minimal square ellipses covering 90% of the craters in the cluster, constructed in two different ways. Solid line corresponds to MVE ellipse and dashed - to Stat one. Pluses show the location of crater centers inside the cluster, the circles around show the size of craters (ones marked black are included in upper quantile by size). A: Cluster PSP_006972_1710 with small number of craters (N=9). B: Cluster ESP_016238_1850 with large number of craters (N=465).

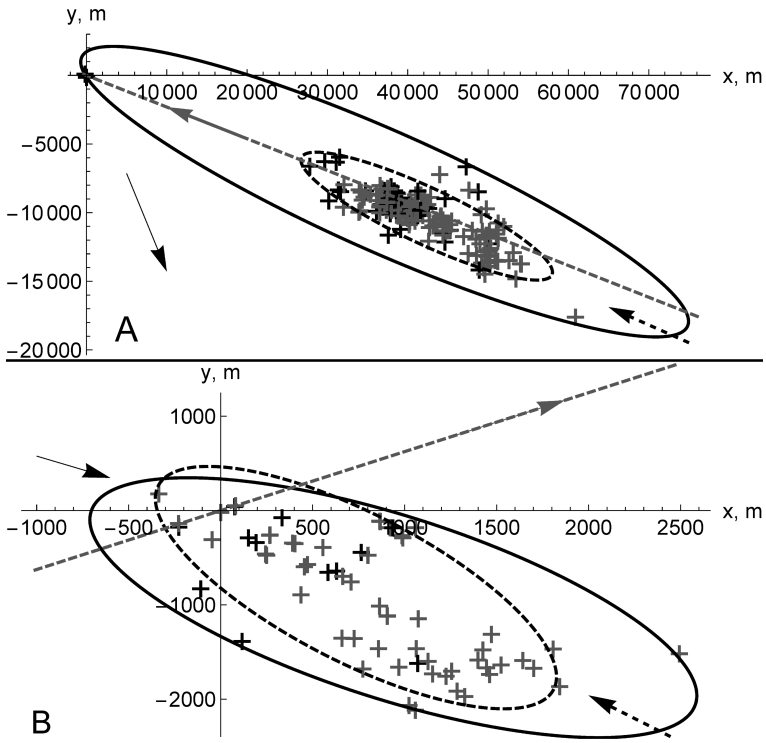

Figure 3. Scattering ellipses on the Earth covering the found fragments and constructed by two different methods. Solid line corresponds to MVE ellipse and dashed - to Stat. Pluses show the location of fragments inside the cluster (black ones are included in upper quantile by size). The black solid arrow marks the wind direction. A: Chelyabinsk meteorite. The dashed line indicates the trajectory from an independent source (Popova et al., 2013), which coincides with one obtained in this work (the arrow on the trajectory line shows the direction of flight). B: Meteorite Ozerki. The dashed line refer to the trajectory from an independent source (Kartashova et al., 2020) (the arrow on the trajectory line shows the direction of flight). The dashed arrow indicates the average trajectory and direction of flight for discussed methods.

ellipses as 308-321°(taking into account the direction; Fig. 3). Analysis of video records (Kartashova et al., 2020) results in azimuth about 58° ± 3° (the trajectory is directed from southwest to northeast; Fig. 3), the difference with our estimates is large. According to the data of the nearest meteorological station (50 km), the wind during the meteoroid flight was directed from an azimuth of 300°at altitudes below 20 km. Based on the location of small fragments to the right of the ellipse (Fig. 3), it can be concluded that the positions of small fragments (less than 1 kg) are primarily determined by the wind. The scattering

field of the Ozerki meteorite is elongated in the direction of the wind; for small fragments with an almost vertical entry into the atmosphere, it is primarily determined by the wind.

4. Ejecta

The crater ejecta gives the possibility to estimate the direction of the flight in some cases. For oblique impacts crater ejecta is asymmetrical and is more pronounced in the direction of flight (Shuvalov, 2011). The images allow us to consider craters ejecta in detail for a number of clusters. The direction of flight determined by the ejecta was compared with estimates from scattering ellipses. The azimuths were found based on the location of craters ejecta from the images of Mars provided by the HiRISE project (Burleigh et al., 2012; Ivanov et al., 2010). The azimuth estimates for the projection of fragments trajectory from crater ejecta were done for 41 out of 55 considered clusters, examples of comparing meteoroid trajectory for two clusters are shown at Fig. 4. Flight direction of the meteoroid obtained by the crater ejecta does not agree very well with the azimuths calculated from the scattering ellipses. In one third of the cases the difference is no more than 45°, in 40% of the cases the results differ in direction (180° ± 45°). For 30% of cases the directions are perpendicular, i.e., ejecta is directed mainly along the minor axis of the scattering ellipse (i.e., across the scattering field).

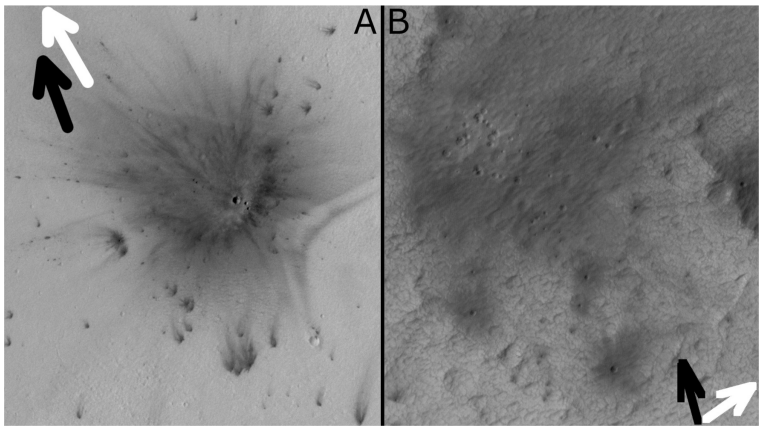

Figure 4. Images from HiRISE for two clusters. Arrows show meteoroid flight direction obtained by scattering ellipse (black arrows) and by craters ejecta location (white arrows). A: Cluster ESP_024646_1890. B: Cluster ESP_026009_1920.

5. Summary

Crater strewn fields are often described by an ellipse. It is suggested that this description allows to estimate trajectory azimuth and entry angle based on the scattering ellipse. Several methods of ellipse construction were applied to fresh Martian crater clusters and best ones were chosen. The resulting ellipses were compared with each other and with an independent estimate. Comparison (by the number of covered craters and by area) showed that the considered methods give a scattering ellipse with an area of 1.41.7 times to the area obtained from the initial estimates (Daubar et al., 2019) and cover at least 88% of craters in clusters in average. From the scattering ellipses, estimates of the parameters for meteoroids entry into the atmosphere (entry angle and azimuth) were obtained. In general, all the considered methods give approximately the same value of the meteoroid trajectory azimuth, the difference in most cases does not exceed 15°. Meteoroid flight is directed from the center of the scattering ellipse along its major axis towards the maximum crater. The flight direction coincides with an accuracy of 45°in 80% of cases, in 10-15% - the direction is opposite. In the remaining 5-10% of cases the constructed scattering ellipses are perpendicular to the independent source estimates (Daubar et al., 2019). The meteoroid entry angle into the atmosphere depends on the ratio of the scattering ellipse semi-axes; its estimates by different methods in most cases differ by less than 15°from the initial estimate (Daubar et al., 2019).

The algorithms for constructing scattering ellipses were applied to the data on the fragmentation of two meteoroids on Earth - the Ozerki and Chelyabinsk meteorites. It was shown that it is possible to estimate the azimuth and the entry angle for large fragments in oblique impact, whose fall is little affected by wind. The scattering field of small fragments of a meteoroid with an almost vertical trajectory of entry is determined mainly by wind drift.

For some clusters, the azimuth of the meteoroid trajectory was found from craters ejecta. In about 70% of these clusters the ejecta is oriented along the scattering ellipse major axis (with accuracy 45°), the direction of flight coincides only in 30%. The direction of the ejecta from the crater along the minor axis of the scattering ellipse, obtained in 30% of cases, requires consideration. Modeling the formation of scattering fields probably help to solve these problems.

References

Borovička, J., Spurný, P., Brown, P., et al., The trajectory, structure and origin of the Chelyabinsk asteroidal impactor. 2013, *Nature*, **503**, 235, DOI: 10.1038/nature12671

Burleigh, K. J., Melosh, H. J., Tornabene, L. L., et al., Impact airblast triggers dust avalanches on Mars. 2012, *Icarus*, **217**, 194, DOI: 10.1016/j.icarus.2011.10.026

Daubar, I. J., Banks, M. E., Schmerr, N. C., & Golombek, M. P., Recently Formed Crater Clusters on Mars. 2019, *Journal of Geophysical Research (Planets)*, **124**, 958, DOI: 10.1029/2018JE005857

Daubar, I. J., McEwen, A. S., Byrne, S., Kennedy, M. R., & Ivanov, B., The current martian cratering rate. 2013, *Icarus*, **225**, 506, DOI: 10.1016/j.icarus.2013.04.009

Hartmann, W. K., Daubar, I. J., Popova, O., & Joseph, E. C. S., Martian cratering 12. Utilizing primary crater clusters to study crater populations and meteoroid properties. 2018, *Met. Planet. Sci.*, **53**, 672, DOI: 10.1111/maps.13042

Ivanov, B. A., Melosh, H. J., McEwen, A. S., & HiRISE Team, Small Impact Crater Clusters in High Resolution HiRISE Images. 2008, in *Lunar and Planetary Science Conference*, Lunar and Planetary Science Conference, 1221

Ivanov, B. A., Melosh, H. J., McEwen, A. S., & HiRISE Team, New Small Impact Craters in High Resolution HiRISE Images - III. 2010, in *Lunar and Planetary Science Conference*, Lunar and Planetary Science Conference, 2020

Kartashova, A., Golubaev, A., Mozgova, A., et al., Investigation of the Ozerki meteoroid parameters. 2020, *Planetary Space Science*, **193**, 105034, DOI: 10.1016/j.pss.2020.105034

Malin, M., Edgett, K., Posiolova, L., McColley, S., & Noe, D. E., Catalog of new impact sites on Mars formed May 1999–March 2006. Malin Space Science Systems. 2006, *Inc., San Diego, California*

Podobnaya, E., Popova, O., & Glazachev, D., Scattering Ellipses for Fresh Clusters of Craters on Mars. 2020, *Collection of scientific papers IDG RAS. Dynamic processes in geospheres. Issue 12. (In Russian)*

Popova, O., Rybnov, Y., Kharlamov, V., & Glazachev, D., Analysis of Optical and Infrasonic Observations of the Ozerki Meteorite Fall. 2019, *Abstract Book of the 5th International Conference "Trigger Effects in Geosystems"*, 165

Popova, O. P., Jenniskens, P., Emel'yanenko, V., et al., Chelyabinsk Airburst, Damage Assessment, Meteorite Recovery, and Characterization. 2013, *Science*, **342**, 1069, DOI: 10.1126/science.1242642

Shuvalov, V., Ejecta deposition after oblique impacts: An influence of impact scale. 2011, *Met. Planet. Sci.*, **46**, 1713, DOI: 10.1111/j.1945-5100.2011.01259.x

Contrib. Astron. Obs. Skalnaté Pleso **51**, 249 – 256, (2021)
https://doi.org/10.31577/caosp.2021.51.3.249

Approach to build a dedicated space born small aperture UV telescope for the long term study of comets (Comet-UV project)

M. Sachkov, A. Shugarov, V. Shmagin and A. Kartashova

Institute of Astronomy of the Russian Academy of Sciences, 48 Pyatnitskaya st. 119017, Moscow, Russia

Received: August 1, 2021; Accepted: November 22, 2021

Abstract. We present the concept of a small-aperture 20 cm wide field UV telescope for a long term detailing study of comets in UV range. Because of the small size and autonomous repointing system, the proposed telescope can be installed on various satellites as an auxiliary instrument. It also can be used on the future International Lunar Research station (ILRS). The main goal of the mission is the long term detailed study of comets and other minor bodies in the Solar System. We briefly discuss variants of the optical schemes, methods of pointing the telescope, scientific filters and modern CMOS detectors. A small dedicated UV telescope with a modern detector will obtain a lot of new information to study comets in the UV range.

Key words: Comets – Space telescope – UV

1. Introduction

Comets are important "eyewitnesses" of Solar System formation and evolution. It is also a rich material for the study of the formation of exoplanets (Fossati et al., 2014). The data in the UV range of the electromagnetic spectrum helps to determine the chemical composition and to study the physical processes in cometary nuclei and coma (Shustov et al., 2018).

Comets were observed many times in UV by large space telescopes such as HST, FUSE, GALEX (see a review by Sachkov (2016)). The World Space Observatory - Ultraviolet (WSO-UV) project, which is scheduled to launch in 2025, will effectively solve most problems in the field of ultraviolet studies of comets and can become an important research tool (Sachkov et al., 2018, 2019). At the same time, because of the lack of available observing time to study comets with large space telescopes, we are looking to build a small and relatively cheap dedicated instrument, optimized for a specific scientific task, to observe comets in the UV range, which is inaccessible for any ground telescopes.

Small aperture and, therefore, lack of sensitivity of such a small instrument can be compensated by a huge amount of observing time to observe each comet of interest. Digital co-adding of large amounts of images taken with dithering

will allow us to get reasonably detailed images of extended comet tails with both acceptable angular resolution, sensitivity and dynamic range even with a small telescope.

The Comet-UV project is based on the ultraviolet telescope and a modern CMOS detector with a special multilayer quadrant UV filter with excellent suppression of visible light.

The CMOS detector, which is not sensitive to local overexposure and has a low readout noise, will allow to achieve a high S/N ratio when adding a large number of frames of the comet's nucleus and tail. The presence of a bright comet nucleus will not affect the telescope's ability to observe a weak tail.

In the basic version, a full-aperture slewing mirror will be installed in front to repoint the telescope. The slewing mirror will be used not only to point the telescope at the selected area, but also to switch between filters and perform dithering. The image of the comet will be sequentially projected onto 4 areas of the detector covered with different filters, and for each filter several images will be obtained with a small (a few pixels) image offset inside one filter in order to reject the traces of cosmic particles and detector defects.

The future International Lunar Research Station (ILRS) can be considered as a place to install this small aperture (15-30 cm) UV telescope (Sachkov et al., 2020). It can be used for the long term detailed study of comets and other minor bodies in the Solar System in several FUV and NUV bands, as well as in visible and possibly IR.

The proposed UV telescope also can be part of scientific payload on other spacecraft.

2. The telescope

Several optical schemes are considered for the Comet-UV project.

In the simplest option, a two-mirror axial scheme without a corrector with the detector located in the Cassegrain focus can be used. The main advantages of this option are simplicity, compactness and maximum transmission in UV. The main disadvantages are limited field of view (less than 0.5 deg) and presence of distortion at the edge of the detector.

To increase the field of view and compensate distortions, it is possible to use a lens corrector from MgF_2 or CaF_2. The operation of such a corrector in a wide range of wavelengths from vacuum UV to the visible region needs additional investigation.

The most promising is an off-axis multi-mirror optical scheme that provides excellent image quality over a field of 1 deg, wide spectral range and symmetrical PSF due to the absence of secondary mirror mounting spiders. The main disadvantages are the complexity of manufacturing, adjustment and the strict requirements for the mirror position stability.

Due to the small aperture and compactness of the Comet-UV telescope, it is possible to manufacture such off-axis schemes, including structural elements, entirely from materials with low coefficients of thermal expansion. Accurate focusing of the telescope can be carried out by controlled heating of some structural elements.

Preliminary, as a baseline for the Comet-UV conceptual design, we have chosen a classical RC optical system with enhanced CaF_2 lens corrector which operates from FUV to optical wavelength ranges. It provides image quality of 0.5 arcsec in all filters. If necessary, a filter wheel can be installed in front of the detector. The preliminary parameters of the telescope are as follows:

Table 1. The main parameters of the Comet-UV telescope.

Parameter	Value
Telescope aperture	200 mm
Optical scheme	RC with CaF_2 corrector
Focal length	3000 mm
Field of view (round, diameter)	0.54×0.43 deg (on 23×18.4 mm detector)
Spectral range	125–900 nm
D_{80}	9 μm @ 125 nm 30 μm @ 500 nm
Central obscuration	32 %
Detector	CMOS GSPRINT4521
Detector size	23×18.4 mm
Detector format	5120×4096 pixels
Pixel size	4.5 μm
Pixel scale	0.38 arcsec pixel^{-1}
Typical single exposure	up to 600 s
Slewing mirror size	320×220 mm
Slewing mirror tilt angles	pitch +30°...+90° roll ± 60°
Area of observation with a slewing mirror	60°×120°
Time of repointing	3 s
Telescope length	600 mm
Telescope with slewing mirror length	1100 mm

Depending on the available detector, the field of view of the Comet-UV telescope will be about 0.54°×0.43°. We propose to use a detector with a small pixel (4.6 μm) and electronic shutter.

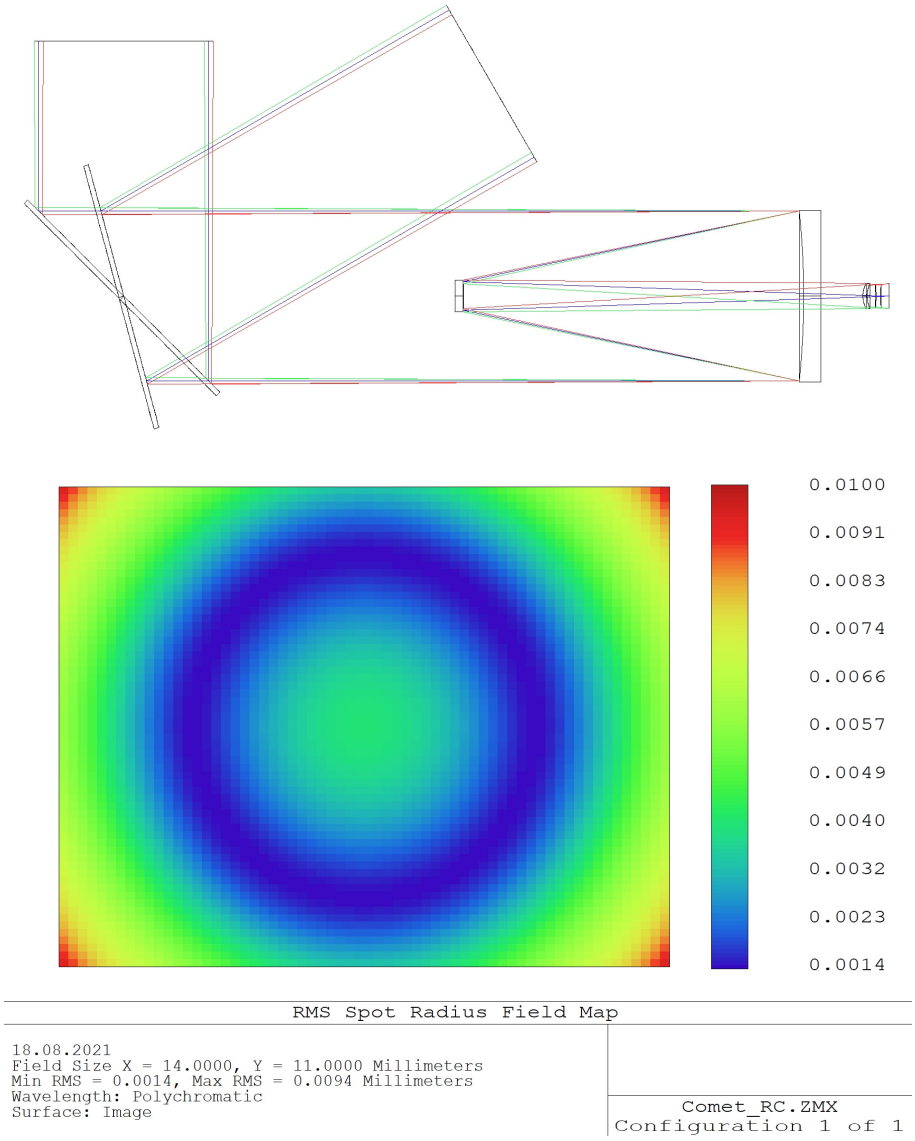

Figure 1. Optical scheme of the telescope with a repointing mirror (top), image quality (bottom).

3. Telescope repointing system

In large projects, the telescope is usually rigidly mounted to the platform. Telescope pointing at the object is carried out by moving the entire spacecraft, followed by precise stabilization of the platform.

When designing a relatively small telescope, operated as an additional payload, or if there are a large number of other scientific instruments on the spacecraft with their own requirements for the orientation of the platform, the telescope should provide an autonomous repointing system to point, stabilize and track the object of interest. It also may be required to compensate for residual drifts of the space platform.

Autonomous repointing of a small telescope can be carried out in two ways, by using a full-aperture mirror installed in front of the entrance pupil of the telescope, or by installing the telescope on a two axis mount.

The main advantages of repointing using a full-aperture mirror are the speed of repointing, small moment of inertia, and, as a result, small perturbing moment during repointing and possibility of its compensation. The disadvantages are an increase in the dimensions and weight of the optical assembly (the mirror dimensions should be larger than the telescope entrance aperture) and an additional reflecting surface in the optical path.

The main advantage of repointing using a two axis mount is a larger area of observation. The disadvantage is an increase in complexity of the mechanical design.

Preliminary, as a baseline for the Comet-UV conceptual design we have chosen to put a slewing mirror in front of the telescope. The repointing area will be about $60^\circ \times 120^\circ$.

4. Detector and filters

For a long time, the pixel size of a scientific grade CCD could not be reduced below the threshold of about 10 μm without significant losses in the well capacity, limitations in the CCD production technology and problems with readout time and noise. In the last few years, thanks to the rapid development of CMOS technology, it has become possible to manufacture an active pixel with a size of 3-5 μm, sufficient well capacity (tens of thousands of electrons), low noise and high quantum efficiency. Due to the very low CMOS reading noise (down to $1\,e^-$ RMS), a dynamic range of such small pixels can be more than 5000:1, which is comparable to a classic CCD.

With small pixel size CMOS it is possible to improve the spatial resolution by having better sampling or to increase the field of view of the telescope while maintaining sampling.

Observation in UV with CMOS and CCD detectors faces two challenges, low quantum efficiency in UV and the red leak of UV filters.

It is shown in (Nikzad et al., 2012), that it is possible to design simple coatings using different materials to achieve >50% of quantum efficiency in different parts of the UV range: MgF_2 for 130-160 nm range, Al_2O_3 of different thickness for 160-200 nm and 200-230 nm, HfO_2 for 230-280 nm.

The other problem of using CCD or CMOS detectors for observations in the UV range is the long pass transmission (red leak) of filters. It is possible to build a multilayer filter with an acceptable suppression (down to E-5) of the optical component for the near-UV range, however the photometric correction of the observed data will be required for the far-UV range in any case.

For example, in the DORADO project (Singer et al., 2021), it is proposed to use a multilayer dielectric filter on the CCD surface with a band pass of 180-230 nm, which provides a suppression of the optical component down to E-5, twice better than the WFC3 common standalone multilayer filters.

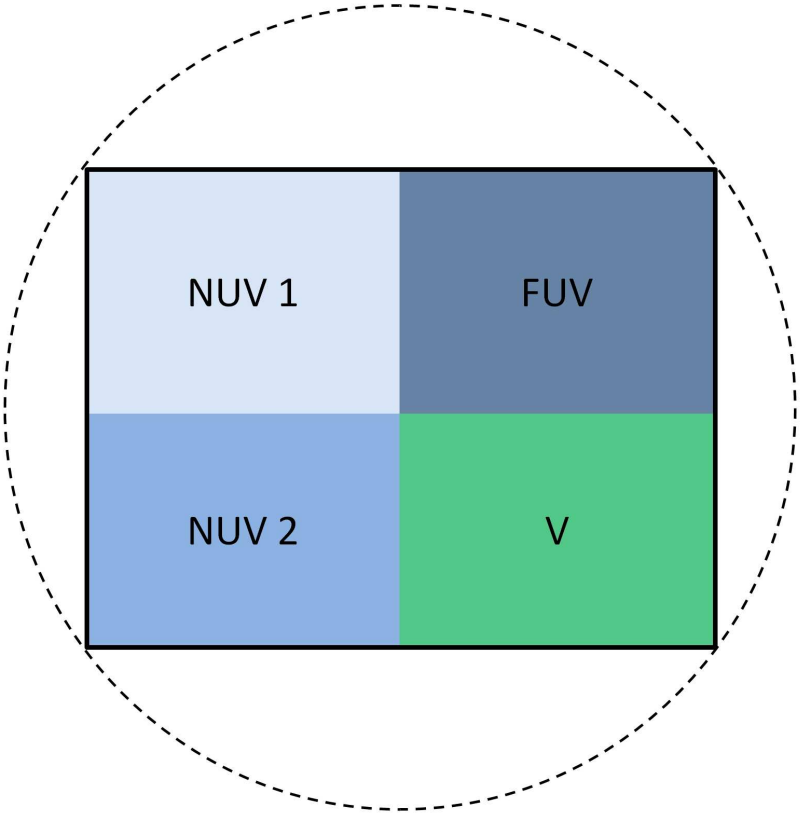

Figure 2. Focal plane and filters layout.

For the Comet-UV project, it is planned to use a modern CMOS from the Chinese company GPEXEL with a special treatment of the back side of the silicon wafer to increase sensitivity in the UV range (Shugarov et al., 2021).

As an example, we can mention a modern CMOS GSPRINT4521 with a global shutter, photosensitive area of 23×18.4 mm, pixel size of $4.5\,\mu$m, pixel capacity of $30000\,e^-$ and readout noise of $3\,e^-$ RMS. We hope that the technology of multilayer coating, similar to the DORADO project, can be applied for GPIXEL's back illuminated CMOS.

For the Comet-UV project, we suggest to deposit 4 multilayer light filters directly on the CMOS chip (Fig. 2). Three UV filters (FUV, NUV1, NUV2) are the main scientific filters and one standard V filter is needed to correct the long-pass transmission of UV filters, e.g. for red leak calibration.

5. Conclusion

Despite a small aperture, the proposed telescope will allow to perform a detailed study of comets in the UV range, which is inaccessible for ground telescopes.

The key technical innovations of the project are the usage of a modern CMOS detector with small size pixels, coated with different multilayer UV filters with good red leak suppression.

Because Comet-UV is a dedicated project to observe comets, it will have a lot of observation time to study each comet of interest. Adding a huge amount (up to hundreds) of images taken in different filters with dithering will allow us to create very detailed images of the comet nucleus and tail in three UV filters and one visible one with reasonable resolution (0.5 arcsec) and high dynamic range of the resulting image. Comets can be observed many times during their travel through the Solar System, including the regions close to the Sun.

The Comet-UV instrument can be installed on various satellites as an auxiliary instrument or on the future International Lunar Research station.

The telescope also can be used to observe other objects of opportunity. Astronomers will receive a relatively universal and inexpensive orbital telescope, operated in UV and optical ranges, suitable for the detailed study of comets and for a wide range of other scientific tasks.

Acknowledgements. Authors acknowledge the support of Ministry of Science and Higher Education of the Russian Federation under the grant 075-15-2020-780 (N13.1902.21.0039).

References

Fossati, L., Bisikalo, D., Lammer, H., Shustov, B., & Sachkov, M., Major prospects of exoplanet astronomy with the World Space Observatory-UltraViolet mission. 2014, *Astrophysics and Space Science*, **354**, 9, DOI: 10.1007/s10509-014-2027-3

Nikzad, S., Hoenk, M. E., Greer, F., et al., Delta-doped electron-multiplied CCD with absolute quantum efficiency over 50% in the near to far ultraviolet range for single photon counting applications. 2012, *Applied Optics*, **51**, 365, DOI: 10.1364/AO.51.000365

Sachkov, M., Sichevsky, S., Kanev, E., & Kartashova, A., WSO-UV Field Camera Unit: science case and ground support with 1-m class telescopes. 2019, *Contributions of the Astronomical Observatory Skalnate Pleso*, **49**, 145

Sachkov, M. E., Spectral studies of comets in the ultraviolet range and prospects of the WSO-UV project in these studies. 2016, *Solar System Research*, **50**, 294, DOI: 10.1134/S0038094616040055

Sachkov, M. E., Kartashova, A. P., & Emel'yanenko, V. V., Prospects for spectral studies of comets: The World Space Observatory - Ultraviolet project. 2018, *Planetary Space Science*, **164**, 75, DOI: 10.1016/j.pss.2018.06.013

Sachkov, M. E., Shugarov, A. S., Shmagin, V. E., & Sichevsky, S. G., The concept of the Moon-based astrophysical UV telescope (The Luna-UV project). 2020, *INASAN Science Reports*, **5**, 368, DOI: 10.51194/INASAN.2020.5.6.011

Shugarov, A. S., Vishnyakov, E. A., Nikolenko, A. D., et al., CCD272-64 and GSENSE400BSI-GP CMOS quantum efficiency measurement in EUV and VUV. in , *International Conference on Space Optics - ICSO 2020*, ed. B. Cugny, Z. Sodnik, & N. Karafolas, Vol. **11852**, International Society for Optics and Photonics (SPIE), 2214 – 2222

Shustov, B., Sachkov, M., Gómez de Castro, A. I., et al., Comets in UV. 2018, *Astrophysics and Space Science*, **363**, 64, DOI: 10.1007/s10509-018-3282-5

Singer, L. P., Cenko, S., & Dorado Science Team, Dorado: A Wide-Field Ultraviolet Imaging Satellite for the Multi-Messenger Era. 2021, in American Astronomical Society Meeting Abstracts, Vol. **53**, *American Astronomical Society Meeting Abstracts*, 309.05

Contrib. Astron. Obs. Skalnaté Pleso **51**, 257 – 265, (2021)
https://doi.org/10.31577/caosp.2021.51.3.257

Modern UV detectors for small aperture space mission to study comets

A. Shugarov

Institute of Astronomy of the Russian Academy of Sciences, 48 Pyatnitskaya st. 119017, Moscow, Russia

Received: August 1, 2021; Accepted: November 28, 2021

Abstract. A small dedicated UV telescope with a modern detector can obtain a lot of new information to study comets in the UV range, which is inaccessible for ground telescopes. We discuss the latest trends in UV-optimized CMOS and CCD detectors that can improve the efficiency of a small aperture (20 cm) space burn UV telescope. The improvements of classical CCD are moving toward improving quantum efficiency in UV, development of the new anti-reflection coatings and multilayer UV filters with enhanced red leak suppression. CMOS with a very small pixel (3-5 μm) of more than 20 Mpixel format allows to improve sampling and to increase the price/performance ratio of a small aperture telescope.
Key words: UV detectors – CCD – CMOS – comets

1. Introduction

For a long time the efficiency (total transmittance or effective area) of a space telescope in UV was low because of low quantum efficiency of detectors, losses on reflective coatings on the mirrors, absence of anti-reflecting coating for UV lenses, problems with fabrication of large and complicated UV lenses and red leak of UV filters.

The progress in detector and multiplayer filter technologies makes it possible to significantly improve the efficiency of UV telescopes, especially in the near-UV range. Nowadays it has become possible to design a small aperture UV telescope with a total throughput of the system similar to the optical range. For a decade after the completion of the HST, the hopes of astrophysicists are associated with the World Space Observatory - Ultraviolet (WSO-UV) Project, which is scheduled to launch in 2025 (Sachkov et al., 2020, 2019). With the help of the project tools, most of the tasks in the field of ultraviolet studies of comets (Sachkov, 2016; Sachkov et al., 2018) and exoplanets (Fossati et al., 2014) will be effectively solved.

The UV detector with anti-reflective coating and (possibly) with directly deposited UV filters is the key element of the telescope. The design of a new UV wide field telescope should be carried out in parallel with the design of a large format detector and filters.

In this paper we discuss a possible approach to select the UV detector for a small aperture space borne UV telescope to study comets in UV.

2. General requirements for the detector and trade-off between CCD and CMOS

The baseline detector requirements to study comets in UV are as follows:

- image format of no less than 4000×4000 pixels;
- pixel size of 5-10 μm;
- spectral range: FUV and NUV with the best possible sensitivity, with no strict requirements for optical sensitivity;
- red leak suppression of UV filters better and E-5 (target);
- reasonable dynamic range (higher than 5000 in a single frame);
- ability to operate with local over illumination;
- low afterglow;
- very low readout noise (target is 1...2 e^- RMS) to operate with UV filters that lead to a very low background. It is also required to improve image co-adding;
- low dark current (less than 0.01 e^- pixel^{-1} s^{-1}) to operate with exposures of up to a few minutes;
- electronic shutter;
- high radiation tolerance.

Currently, the CMOS detector technology has demonstrated the following characteristics:

- readout noise of less than 3 e^-RMS, some detectors demonstrate a 1 e^- RMS readout noise level in high gain mode with limited dynamic range;
- lag (loss of charge during readout) of less than 2 e^-;
- geometric dimensions of up to 5-7 cm;
- pixels of various sizes down to a few microns are available, however scientific grade sensors with reasonable performance have a pixel size larger than 5 μm;
- quantum efficiency of a back illuminated CMOS with anti-reflective coating has been raised up to 90% in a visible range, which is comparable to the best CCD;

– CMOS back illumination technology demonstrates similar behavior to the CCD technology in terms of quantum efficiency and back surface treatment, therefore, most probably in the future UV optimized CMOS with UV anti-reflective coatings will reach the same quantum efficiency in NUV and FUV ranges as CCD has.

The CCD detector technology has shown the following parameters:

– readout noise of about 3 e^- RMS at low speed;

– large dynamic range, up to 18 bit ADC;

– charge transfer inefficiency for a long space mission is an issue, especially when operated with a low background which is the case for UV observations, in the worst-case scenario charge loses can rise up to 10 electrons;

– geometric dimensions of up to 9 cm;

– frame transfer CCD provides electronic shutter functionality, but with doubled chip area;

– pixel size of 10...20 μm for scientific grade CCD;

– quantum efficiency of back illuminated CCD with coating in NUV can reach 80%;

– technology to improve CCD quantum efficiency in FUV up to 50% was demonstrated;

– series of UV missions demonstrate maturity of the CCD technology.

The main advantages and disadvantages of CMOS versus CCD as a detector for a small aperture UV telescope to observe comets are as follows.

Advantages of CMOS over CCD:

– lower readout noise;

– higher readout speed;

– smaller pixel size;

– electronic shutter (global, roller).

Disadvantages of CMOS over CCD:

– slightly lower quantum efficiency for very small pixel size detectors;

– lower dynamic range;

– pixel-to-pixel variations of photo-electrical parameters;

– to achieve a full dynamic range, many CMOS need to take 2 images with low and high gain modes, which cause additional photometric errors;

– CMOS detectors still have limited heritage in space scientific application, especially in UV range;

– impossibility to achieve extremely (less than $0.01\,e^-\,pixel^{-1}\,s^{-1}$) low dark current even with deep cooling.

3. Quantum efficiency in UV

Observation in UV with CMOS and CCD detectors faces two challenges, low quantum efficiency in UV and the red leak of UV filters.

In the ultraviolet spectral range, the short absorption lengths (below 10 nm) and high reflectance of the silicon strongly affect the quantum efficiency.

In the USA (NASA Jet Propulsion Laboratory), a surface passivation technology by boron atoms (delta-doped) was developed Hoenk et al. (2014). The technology of surface growth using a molecular beam on the back surface of a CCD, CMOS or photodiode with control accuracy up to the atomic level is used. Afterwards, the ALD (atomic layer deposition) technology is used to apply a multilayer anti-reflection coating on the detector. The combination of these two technologies makes it possible to build a CCD or CMOS detector with a high quantum efficiency in the range of 100-300 nm. Delta-doped technology provides a high internal quantum efficiency and the additional anti-reflection coating reduces light loss on reflection. It is shown Nikzad et al. (2012), that it is possible to design simple coatings using different materials to achieve >50% of quantum efficiency in different parts of the UV range: MgF_2 of 13 nm thickness for 130-160 nm range, Al_2O_3 of 16 nm thickness for 160-200 nm, Al_2O_3 of 23 nm thickness for 200-230 nm, HfO_2 of 23 nm thickness for 230-280 nm.

Alternatively, Teledyne e2v has developed the proprietary processes to improve the UV quantum efficiency Heymes et al. (2020). To improve internal quantum efficiency, the shallow p+ implantation is used to permit the thinning of the backside potential well of a CCD chip. Two different levels are available: basic with a 40 nm ±10 nm thick p+ layer and enhanced which uses an extra etching process to thin the p+ layer. For the enhanced process, the quantum efficiency without coating is about 10-15% in FUV range.

The second step is reducing the reflectivity of the back-surface by using an anti-reflective coating designed for targeted wavelengths. For example, for the WUVS project Teledyne e2v developed a special gradient anti-reflection coating for 180-310 nm range matched with a spectrograph dispersion Shugarov et al. (2014). According to the test results, this coating improves the quantum efficiency up to 4 times in comparison with the uncoated CCD in 250-300 nm range Shugarov et al. (2021a).

One of the prospect examples of using a CMOS detector to operate in the near UV range is the Ultraviolet Transient Astronomical Satellite (ULTRASAT) Asif (2021) that is currently in a preliminary design phase. The wide field UV space telescope has a 200 $\deg^2$ field of view and the mosaic of four backside illuminated UV optimized CMOS sensors has a sensitive area of 90×90 mm (89.8 Megapixel). The CMOS sensors are designed and produced by Tower Semiconductor Ltd and Analog Value Ltd. (AV) in Israel. The photo sensitive area of a single chip is 45.011×45.011 mm (4738×4738 pixels) with a pixel size of 9.5 μm, well capacity is 140 ke^- and 16-21 ke^- in low and high gain modes, dark current is $< 0.026\,\mathrm{e}^-\,\mathrm{s}^{-1}$ at 200 K, readout noise with rolling shutter is $< 3.5\,\mathrm{e}^-$ RMS and a readout time of < 20 s.

The key feature of the detector is high quantum efficiency in NUV.

Firstly, the back-illuminated CMOS sensor has high-K dielectric coating to improve internal quantum efficiency in UV. This coating acts similar to the delta doping technology from JPL.

Secondly, an optimized anti-reflection coating is applied. Different anti-reflective coatings were tested to find a balance between transmittance and red leak suppression. According to current test results Bastian-Querner et al. (2021), the average quantum efficiency of 60% (corrected for quantum yield) in the range of 220-280 nm can be achieved.

4. Field of view, angular resolution and image co-adding

Digital co-adding is especially important for a small aperture telescope without a large mosaic. It is the only way for a small telescope to improve sensitivity, to achieve best possible angular resolution and to map extended objects such as comets in different filters.

For each project the telescope field of view and detector pixel scale should be selected in order to find a balance between angular resolution, field of view and observation rate according to scientific tasks.

Because of a limited amount of comets, for a dedicated project to observe comets in UV the observing rate is not a priority. To study comets in UV and to compete with other ground based and space borne telescopes, the angular resolution should have priority over a single frame field of view, because of the possibility to construct a mosaic image using many observations.

The angular resolution should be better than 0.5 arcsec and the telescope field of view large enough to utilize a 20-50 Mpixel class detector.

Image co-adding helps to improve the dynamic range of a CMOS detector that may have only 12-14 bit ADC. Image co-adding is especially important for a small pixel size CMOS with a limited pixel well capacity. Image co-adding with a high gain mode may be considered instead of using a CMOS dual gain readout to improve the photometric accuracy, if a detector with 1 e^-RMS noise will be available.

Fixed filters directly deposited on a detector is a good choice for a small size telescope to simplify the design and to reduce the cost, as well as to improve the red leak suppression. Fixed filters are another argument to use image co-adding technique.

The main negative point of co-adding is extra consuming of observing time.

5. Small pixel size CMOS

In the last few years it has become possible to manufacture an active pixel with a size of 3-5 μm with reasonable well capacity of tens of thousands of electrons, low noise and high quantum efficiency.

In high gain mode some CMOS has a readout noise as low as 1 e^- RMS, thus a dynamic range of such small pixels can be more than 5000:1, that is enough for scientific application and even can compete with some classic CCD.

The combination of a telescope with high image quality and CMOS with a small pixel allows to build a wide field telescope with an improved price/performance ratio.

The CMOS cost is not as high as the telescope and evidently much lower than the whole mission cost. Therefore, it is better to chose the detector that is slightly larger than the telescope's field of view, e.g. to put the round telescope field of view inside the square detector with a small margin at the detector's edge.

Using small pixel size CMOS it is possible to increase the field of view of the telescope while maintaining sampling without increasing the cost of the focal unit. The other option is to improve the spatial resolution by having better sampling.

Designing and manufacturing of the moderate field of view telescope with enhanced image quality in order to operate with a small pixel detector is complicated and expensive, however modern technologies of optics manufacturing will probably keep the telescope cost at a reasonable level.

As an example, the 151 Mpixel CMOS IMX411BSI has format of 14×10 k (54×40 mm) and a pixel size of 3.76 μm. Unfortunately, this promising sensor most probably will not have a UV-enhanced option.

Another example is a modern CMOS GSPRINT4521 with a global shutter, photosensitive area of 23×18.4 mm, pixel size of 4.5 μm, pixel capacity of 30000 e^- and reading noise of 3 e^- RMS. UV-optimized GPEXEL sensors with special treatments of the back side of the silicon wafer demonstrated reasonable quantum efficiency without anti-reflection coating Shugarov et al. (2021b). We hope that multilayer UV coating, similar to the DORADO project, can be applied for GPIXEL's back illuminated CMOS.

6. UV filters to observe comets

Red leak is one of the main problem to design UV filters for silicon-based detectors.

For the near-UV range the best multilayer filters provide acceptable suppression of the optical component, however for the far-UV range the photometric correction of the observed data is required in most cases.

In the DORADO project it is proposed to use a multilayer dielectric filter on the CCD surface Singer et al. (2021). The operation band pass is 180-230 nm and suppression of the optical component is about E-5. It was demonstrated that directly deposited filter on CCD provides twice better suppression than the HST WFC3 common standalone multilayer filters.

To observe comets in UV, we suggest putting at least 4 multilayer filters directly on the detector: three for the UV range (FUV, NUV1, NUV2) and one standard V filter to correct the long-pass transmission of UV filters, e.g. for red leak calibration. The presence of several optical filters will expand the scientific capabilities of the mission.

Directly deposited filters help to avoid additional mechanical filter change mechanism.

7. Conclusion

A promising way to build an effective small aperture moderate price UV telescope to observe comets in UV is to combine the following approaches and technologies:

- to design a telescope with a UV lens field corrector to provide better than 0.5 arcsec resolution with a 5 μm pixel size detector;
- to use small pixel size CMOS of a 20-50 Mpixel format to improve angular resolution and data capacity;
- to look for a 1 e^- RMS noise CMOS detector to improve image co-adding and to utilize the advantage of a low sky background in UV;
- to look for the possibility to deposit several different UV-optimized coatings (probably of different materials) on the detector;
- to look for the possibility to deposit several UV filters with good red leak suppression on the detector.

A combination of a small aperture high angular resolution telescope and CMOS with a small pixel will allow to design a system with better price/performance ratio than before. The CMOS detector, which is not sensitive to local overexposure and has a large dynamic range, will allow to achieve a very high S/N ratio when adding a large number of frames of the comet's nucleus and tail.

The presence of a bright comet nucleus will not affect the telescope's ability to observe a weak tail.

A dedicated 20 cm aperture UV-optimized telescope with modern UV optimized detector and filters will allow to perform a detailed study of comets in the UV range, which is inaccessible for ground telescopes.

References

Asif, A., Design of the ULTRASAT UV camera. in , *UV, X-Ray, and Gamma-Ray Space Instrumentation for Astronomy XXII*, ed. O. H. Siegmund, Vol. **11821**, International Society for Optics and Photonics (SPIE), 272 – 280

Bastian-Querner, B., Kaipachery, N., K?ster, D., et al., Sensor characterization for the ULTRASAT space telescope. in , *UV/Optical/IR Space Telescopes and Instruments: Innovative Technologies and Concepts X*, ed. A. A. Barto, J. B. Breckinridge, & H. P. Stahl, Vol. **11819**, International Society for Optics and Photonics (SPIE), 136 – 152

Fossati, L., Bisikalo, D., Lammer, H., Shustov, B., & Sachkov, M., Major prospects of exoplanet astronomy with the World Space Observatory-UltraViolet mission. 2014, *Astrophysics and Space Science*, **354**, 9, DOI: 10.1007/s10509-014-2027-3

Heymes, J., Soman, M., Buggey, T., et al., Calibrating Teledyne-e2v's ultraviolet image sensor quantum efficiency processes. in , *X-Ray, Optical, and Infrared Detectors for Astronomy IX*, ed. A. D. Holland & J. Beletic, Vol. **11454**, International Society for Optics and Photonics (SPIE), 263 – 273

Hoenk, M. E., Nikzad, S., Carver, A. G., et al., Superlattice-doped silicon detectors: progress and prospects. in , *High Energy, Optical, and Infrared Detectors for Astronomy VI*, ed. A. D. Holland & J. Beletic, Vol. **9154**, International Society for Optics and Photonics (SPIE), 324 – 336

Nikzad, S., Hoenk, M. E., Greer, F., et al., Delta-doped electron-multiplied CCD with absolute quantum efficiency over 50% in the near to far ultraviolet range for single photon counting applications. 2012, *Applied Optics*, **51**, 365, DOI: 10.1364/AO.51.000365

Sachkov, M., Sichevsky, S., Kanev, E., & Kartashova, A., WSO-UV Field Camera Unit: science case and ground support with 1-m class telescopes. 2019, *Contributions of the Astronomical Observatory Skalnate Pleso*, **49**, 145

Sachkov, M., Sichevsky, S., Shustov, B., et al., Field camera unit of the WSO-UV mission. 2020, in Society of Photo-Optical Instrumentation Engineers (SPIE) Conference Series, Vol. **11444**, *Society of Photo-Optical Instrumentation Engineers (SPIE) Conference Series*, 1144474

Sachkov, M. E., Spectral studies of comets in the ultraviolet range and prospects of the WSO-UV project in these studies. 2016, *Solar System Research*, **50**, 294, DOI: 10.1134/S0038094616040055

Sachkov, M. E., Kartashova, A. P., & Emel'yanenko, V. V., Prospects for spectral studies of comets: The World Space Observatory - Ultraviolet project. 2018, *Planetary Space Science*, **164**, 75, DOI: 10.1016/j.pss.2018.06.013

Shugarov, A., Savanov, I., Sachkov, M., et al., UV detectors for spectrographs of WSO-UV project. 2014, *Astrophysics and Space Science*, **354**, 169, DOI: 10.1007/s10509-014-1911-1

Shugarov, A. S., Sachkov, M., Bruce, G., et al., WSO-UV mission WUVS instrument FUV-UV CCD detectors qualification campaign main results. in , *International Conference on Space Optics - ICSO 2020*, ed. B. Cugny, Z. Sodnik, & N. Karafolas, Vol. **11852**, International Society for Optics and Photonics (SPIE), 2223 – 2234

Shugarov, A. S., Vishnyakov, E. A., Nikolenko, A. D., et al., CCD272-64 and GSENSE400BSI-GP CMOS quantum efficiency measurement in EUV and VUV. in , *International Conference on Space Optics - ICSO 2020*, ed. B. Cugny, Z. Sodnik, & N. Karafolas, Vol. **11852**, International Society for Optics and Photonics (SPIE), 2214 – 2222

Singer, L. P., Cenko, S., & Dorado Science Team, Dorado: A Wide-Field Ultraviolet Imaging Satellite for the Multi-Messenger Era. 2021, in American Astronomical Society Meeting Abstracts, Vol. **53**, *American Astronomical Society Meeting Abstracts*, 309.05

Contrib. Astron. Obs. Skalnaté Pleso **51**, 266 – 269, (2021)
https://doi.org/10.31577/caosp.2021.51.3.266

WSO-UV field camera unit for comet and exoplanet observations

S. Sichevsky, E. Kanev, V. Shmagin and M. Sachkov

Institute of Astronomy of the Russian Academy of Sciences, 48 Pyatnitskaya st. 119017, Moscow, Russia

Received: August 5, 2021; Accepted: November 25, 2021

Abstract. The World Space Observatory for Ultraviolet (WSO–UV) is a space observatory equipped with instrumentation for spectroscopy and for imaging in the UV spectral range. After the Hubble Space Telescope, WSO–UV will be the largest mirror telescope for UV astronomy. Thus, the WSO-UV space observatory will guarantee continuity of UV observation of comets and exoplanets.

Key words: space vehicles: instruments – ultraviolet: general – comets

1. Introduction

WSO–UV is a space observatory in geostationary orbit with an inclination of $\sim 40°$. One has a 1.7–meter telescope capable of spectroscopy and direct imaging in the UV range of the spectrum (115 to 305 nm). The nominal lifetime is 5 years with an expected extension of up to 10 years.

The main scientific purpose of WSO–UV is the spectroscopic observation of faint UV sources and high resolution UV imaging (Fossati et al., 2014; Sachkov, 2016; Sachkov et al., 2018b). WSO-UV includes the T–170M telescope designed to fit requirements of high angular resolution and maximum effective area in the 115 nm–305 nm range. It provides the solar avoidance angle about 40°, that is important for observations of comets at low angular distance from the Sun.

An additional tool has recently been proposed for WSO-UV – UVSPEX, a UV spectrograph, is designed to measure atomic hydrogen and oxygen in the exospheres of terrestrial exoplanets (Tavrov et al., 2018). Examination of the transit photometric curves of the exosphere can help differentiate the different types of rocky planets.

2. Field Camera Unit

One of main instruments of WSO-UV is Field Camera Unit (FCU) which has two channels: NUV (near ultraviolet channel) and FUV (vacuum or far ultraviolet channel):

– FUV: the working wavelength range no narrower than from 115 to 176 nm;

Table 1. NUV channel filters to study Earth–like exoplanets.

Name	Type	Central wavelength, nm	FWHM, nm
F255W	Wide-band filter	255	50
F336W	Wide-band filter	336	50

– NUV: from 174 to 305 nm.

The FUV channel has an MCP detector, which is supplied under the international agreement between Russia and Spain. The main characteristics of the FUV channel are as follows:

– Diffraction-quality imaging.

– Highly sensitive photon-counting mode.

– High temporal resolution.

The NUV channel has a CCD detector sensitive from 174 to 305 nm (with a possible expansion to 1000 nm). The main characteristics of the NUV channel:

– Large field of view (FoV).

– Large dynamic range

Key scientific problems of FCU: study of planetary nebulae; UV behavior of a supernova; study of short-term (about 40 ms) variable sources; astroseismology; exoplanetary atmospheres; protostellar jets; Galactic globular clusters and variables. For more details on the scientific problems of the FCU, see Sachkov et al. (2018a)

The study of comets is one of the most promising areas of astronomy for the next decade. UV–spectroscopy of comets in the 115–300 nm wavelength range plays an important role, since this part of the spectrum contains most of the resonance lines of atoms of molecules and ions. The large FoV and high sensitivity of the NUV channal of FCU will make WSO-UV the most efficient observatory to track comet evolution.

To study Earth–like exoplanets by transits photometry method, two ozone absorption bands filters will be used: 230–280 nm (Hartley band, F255W) and 310–360 nm (Huggins band, F336W).

3. NUV channel: technical realisation of Hartley and Huggins bands

NUV channel is located in the center of telescope's field of view. It provides high transmittance as it contains no additional optics except flat pick–off mirror. It

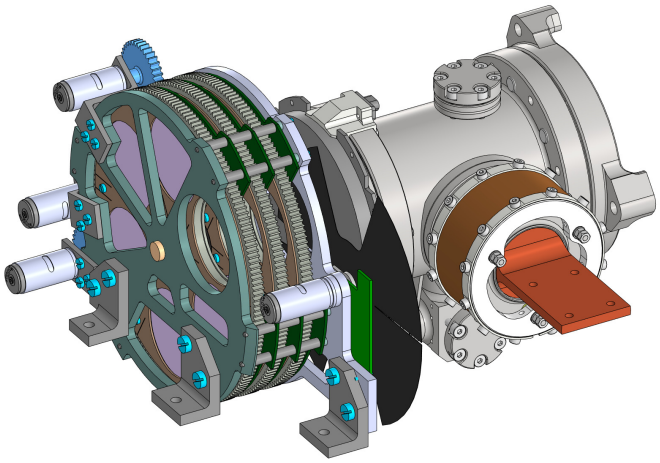

Figure 1. A general view of filter wheels of NUV channel.

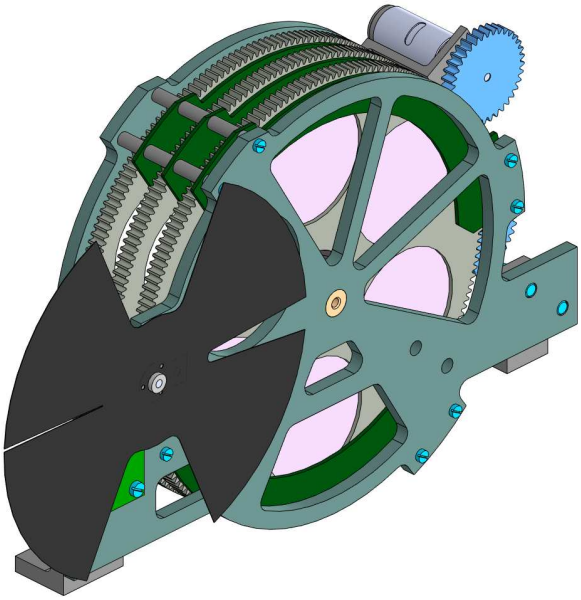

Figure 2. Full–turn shutter of NUV channel.

is equipped with 3 filter wheels with 5 filters and 1 open slot in each one, so up to 15 filters can be used with possibility of combination (see Fig.1).

Full–turn shutter contains 2 open slots for long exposures of faint objects and 2 slits with different width for bright targets and flat–field calibration (see Fig.2).

3.1. Conclusions

The large FoV and high sensitivity of the NUV channel of FCU will make WSO-UV the most efficient observatory to track comet evolution.

The WSO-UV space observatory, scheduled to launch in 2025, could become an important tool in cometary and explanetary UV research in the next decade.

Thus, The WSO-UV space observatorywill guarantee continuity of UV observation of comets and expoplanets.

Acknowledgements. Authors acknowledge the support of Ministry of Science and Higher Education of the Russian Federation under the grant 075-15-2020-780 (N13.1902.21.0039).

References

Fossati, L., Bisikalo, D., Lammer, H., Shustov, B., & Sachkov, M., Major prospects of exoplanet astronomy with the World Space Observatory-UltraViolet mission. 2014, *Astrophysics and Space Science*, **354**, 9, DOI: 10.1007/s10509-014-2027-3

Sachkov, M., Shustov, B., Gómez de Castro, A. I., et al., The new field camera unit imaging instrument onboard WSO-UV. 2018a, in Society of Photo-Optical Instrumentation Engineers (SPIE) Conference Series, Vol. **10699**, *Space Telescopes and Instrumentation 2018: Ultraviolet to Gamma Ray*, ed. J.-W. A. den Herder, S. Nikzad, & K. Nakazawa, 1069935

Sachkov, M. E., Spectral studies of comets in the ultraviolet range and prospects of the WSO-UV project in these studies. 2016, *Solar System Research*, **50**, 294, DOI: 10.1134/S0038094616040055

Sachkov, M. E., Kartashova, A. P., & Emel'yanenko, V. V., Prospects for spectral studies of comets: The World Space Observatory - Ultraviolet project. 2018b, *Planetary Space Science*, **164**, 75, DOI: 10.1016/j.pss.2018.06.013

Tavrov, A., Kameda, S., Yudaev, A., et al., Stellar Imaging Coronagraph and Exoplanet Coronal Spectrometer: Two Additional Instruments for Exoplanet Exploration Onboard The WSO-UV 1.7 Meter Orbital Telescope. 2018, *arXiv e-prints*, arXiv:1810.07644

Contrib. Astron. Obs. Skalnaté Pleso **51**, 270 – 279, (2021)
https://doi.org/10.31577/caosp.2021.51.3.270

Stellar comet spear

M.D. Sizova, A.V. Tutukov and S.V. Vereshchagin

Institute of Astronomy of the Russian Academy of Sciences, 48 Pyatnitskaya st. 119017, Moscow, Russia (E-mail: sizova@inasan.ru)

Received: August 1, 2021; Accepted: September 15, 2021

Abstract. One of the consequences of the evolutionary process of the planetary system is the appearance of comets, asteroids, and even planets (ACP) unbound to their parent star. These small bodies are scattered into interstellar space, orbit the Galactic Center and expand along the star orbit with time. The formed structure resembles a spear in its shape. Similar ACP spears have all stars with planetary systems in the Galaxy. Since such stars are part of the open clusters population, they scatter and form the ACPS spears. In this paper, we performed numerical modeling of the ACP and ASPC spears and estimated their parameters, such as length, width, and time of formation.

Key words: Solar System – comets – open star cluster – Galaxy – kinematics

1. Introduction

Until the 18th century, the interplanetary space of the Newtonian universe was considered empty. This meant that the planets of the Solar system did not exchange matter. One of the consequences of this paradigm was the separation of the phenomena of comets, meteors, and meteorites, attributing them to various natural disasters. It was possible to unite these phenomena only at the turn of the 18–19th century. Ernst Chladni, thus initiated a new, revolutionary change of the astronomical picture of the world (Eremeeva, 2006). With the change of paradigm, it became clear that objects in the Solar system are actively exchanging matter (Martian meteorites, tons of dust falling on the Earth every day). Currently, this statement is not in doubt, and it is difficult to imagine that it was once different.

Nevertheless, the sighting of the first interstellar comet became a real sensation (Meech et al., 2017), and led to a paradigm shift taking place right now, in front of our eyes. We are beginning to understand that not only bodies inside the Solar system exchange matter, but also larger objects - stars, star clusters, and even galaxies. Moreover, ACP objects (asteroids, comets, planets) move freely in the universe, eventually forming clouds, spears and rings along the orbits of their parent bodies. And when approaching, they leave the parent systems and become small interstellar bodies.

This motivates us to take a fresh look at the problems of studying stars and open star clusters, since all stars are born in clusters, and all comets are born in the process of the formation of planetary systems of stars.

Our model assumes the appearance of comets leaving their parent stars due to the gravitational effect from the giant planets. Comets leaving the parent star at the velocities of several kilometers per second end up, prevailingly, in the interstellar space of the Galaxy (Dones et al. (2004) in: Comets II, Univ. Arizona Press, Tucson, pp. 153-174).

Comets leaving the parent star at a velocities of several kilometers per second end up in the interstellar space of the Galaxy. Thus, a cloud resembling a spear is formed (Tutukov & Smirnov, 2004). This process also takes place in the vicinity of all stars with planetary systems. The formation of stars is often accompanied by the appearence of the circumstellar gas-dust disks, the evolution of which leads over time to the formation of planetary systems (Safronov, 1969).

The spear includes not only cometary nuclei but asteroids and planets. The spears of the Sun, stars, and open star clusters formed by the ACP (asteroid – comet – planet) expand the region, in which the objects originating in the given planetary system are situated, to tens of kpc over time. Stars with planetary systems soon begin to be accompanied by ACP spears in the form of spears or even rings, depending on the age of the star. These objects are quite common in the Galaxy since about a third of the stars have planets (Masevich & Tutukov, 1988; Tutukov & Smirnov, 2004).

The work is devoted to the numerical study of the evolution of the free ACP orbits in the Galaxy, leading to their transformation into cometary spears of the Sun, stars, star clusters. Gradually, they form a well-populated ACP component of the Galaxy, composed of filaments of evolved ACP clouds. In particular, for the Solar system, this means that its external boundary expands to several kpc. Interstellar comets are located in ACP spears. ACP spears are generated by distant giants like Jupiter and as a result of the interaction of the planetary Oort cloud with background stars (Faintich, 1971), (Correa-Otto & Calandra, 2019), (Tutukov et al., 2020). Recently discovered interstellar objects 2I/Borisov and 1/I Oumuamua represent this component of the Galaxy (Borisov et al., 2013), (Hallatt & Wiegert, 2020). Note that interstellar meteors with a mass of $\sim 10^4$ g were found by Froncisz et al. (2020), which also represent a significant part of the ACP of the Galactic component. Note also that microlensing facilitates and makes real the process of registering free planets of the Galaxy, lost by parent stars (Mróz et al., 2020).

Since practically all stars are formed in star clusters, about one-third clusters membership stars may have planetary systems (Tutukov, 1978). Thus, ACP spears are inherent for clusters as well. It was shown, that evaporation of stars from clusters leads to the appearance of stellar spears clusters along clusters galactic orbits (Tutukov et al., 2020). The presence of massive and distant enough planets in planet systems leads to the loss of asteroids, comets and Earth–like planets from their parent systems with velocities several kilometers

per second. This process was demonstrated by numerical model in (Tutukov et al., 2020). Lost ACP objects of stars with planet systems will form wide ACP spears in parent clusters which leads to a quick appearance of a rather dense ACP component of star clusters.It is of interest to point here that velocities of a part ACP objects lost by planet systems exceed second space speed for clusters. As a result stellar clusters are forming ACP spears overlapping with its stellar spears. Resulting ACPS spears have to be rather dense, since a significant concentration of stars in their cluster. It is quite possible that the ACPS spears of several close clusters like Pleiades are now identified by Gagné et al. (2021).To determine the potential trajectory of ACPS objects, it is necessary to study the orbits of open clusters and calculate their motion in past epochs.

The structure of the work is based on the similarity of the evolution of stellar and cometary clouds, turning into spears and, over time, into circular streams around the Galactic Center. Section 2 provides an analytical estimate of the parameters of cometary spears formed by the former stellar population of open clusters. These stars have left their parent cluster and formed spear – like structures stretched along galactic orbits. Section 3 contains a description of the Galaxy model. It was used to calculate the evolution of stellar – cometary clouds, the results of which are presented in Section 4 and Section 5. Section 6 contains a brief discussion and Conclusions.

2. Analytical estimates

A lifetime of open clusters is limited by dissipation of stellar component (Chandrasekhar, 1943). Cluster stars, leaving a cluster with a velocity of about 1 km s^{-1}, enrich the stellar component of the ACP open cluster spear. Thereby, these stars replenish the population of the open cluster ACP component. Including the stars, we call it the ACPS spear. An additional way for enrichment of the stellar component of ACPS cluster spear provides for close binary and unstable multiple stars of the cluster. Dissociation of unstable multiple stars leaving parent cluster for ACPS spears. Supernovae explosions in massive close binaries lead to the appearance of fast stars leaving parent clusters again for cluster ACPS spear.

Let us present here some numerical estimates related to stellar cluster, grounded in assumption that their masses M and radii R are connected by the relation $M = 0.2R^2$ (Tutukov, 2019). Roche lobed Oort cloud radius R_R for a cluster star with mass m will be

$$R_R = 2 \times 10^3 (M/M_\odot)^{1/6} (m/M_\odot)^{1/3} AU \quad (1)$$

The distance of the closest encounter between stars in cluster during time t will be

$$\frac{r_{min}}{AU} = 40 (M/M_\odot)^{1/8} (m/M_\odot)^{1/2} (year/t_{10})^{1/2} \quad (2)$$

where t_{10} is the time in units 10^{10} years. It is evident that during the lifetime of open cluster 10^8 years, planet systems with sizes below ~ 40 AU (Tutukov, 1978) remain untouched by cluster stars. But Roche lobe with filling the latter stellar Oort cloud will be intersected by cluster stars about N times:

$$N = 0.16\ t/\tau_k (M/m)^{1/3} \tag{3}$$

where $\tau_k = \frac{R^{3/2}}{G^{1/2}M^{1/2}}$ is Keplerian time of cluster $\tau_k = 10^5 (M/M_\odot)^{1/4}$ years. For $M \approx M_\odot$ we will have $N \cong 1.6 \times 10^4 (M/M_\odot)^{1/12}\ t/10^{10}$ years times. For an open cluster with $M \approx 10^3 M_\odot$ and lifetime $\sim 10^8$ years cluster stars about 200 times intersect Oort clouds of stars with planets. Let us point here that for Solar Oort cloud this member is about 10^5. The intersection of cloud stars Oort clouds leads to a strong dissipation of their ACP member and to the enrichment of ACP component of clusters themselves and cluster ACP spears. Interaction of stars with Oort clouds can be an efficient source of ACP objects of the ACP cluster spears.

3. Galaxy Model

Bulge, represented by a power-law spherical density potential with an exponential cut–off. With the accepted normalizations $\alpha = 1.8$, $r_c = 1.8/8.178$, $v_c(1,0) = 1$ it is presented:

$$\begin{aligned} \rho(r) &= \left(\frac{r_1}{r}\right)^{\alpha} e^{(r/r_c)^2} \\ \rho(R = 8.178, z = 0) &= 27.37 \end{aligned} \tag{4}$$

The potential of the Galactic disk, $\Phi(R,\ z)$, is mathematically described by the expressions by Miyamoto & Nagai (1975):

$$\Phi(R,\ z) = -1/\sqrt{R^2 + (a + \sqrt{z^2 + b^2})^2} \tag{5}$$

where a is the radius of the disk $a = 1.0$, b is the thickness of the disk $b = 0.1$, R is the radial distance from the galactic center, z is the coordinate in the accepted galactic rectangular coordinate system.

Halo - spherically symmetric spatial density distribution of the dark matter in the halo along the profile of (Navarro et al., 1996), with the accepted normalizations 16/8.178, $v_c(1,0) = 1$ it is presented

$$\begin{aligned} \rho(r) &= \frac{1}{4\pi a^3} \frac{1}{(r/a)(1 + r/a)^2} \\ \rho(R = 8.178, z = 0) &= -2.69 \end{aligned} \tag{6}$$

where a is the radius.

4. The Sun motion

Figure 1 shows the orbit of the Sun calculated backward 5 billion years by dint of the so-called "classical potential of the Milky Way" by Bovy (2015) – Eqs. 4 - 6. We took the distance of the Sun to the Galactic Center $R_0 = 8.178$ kpc, and the circular velocity of the Sun $V_0 = 232.8$ km s^{-1} (McMillan, 2017), (Gravity Collaboration et al., 2019). Initial values of the Sun rectangular coordinates and spatial velocity components are $(X\ Y\ Z) = (R_0\ 0\ 20.8)$, $(U\ V\ W) = (0\ V_0\ 0)$. Directions of the coordinate axes: the X–axis is directed to the center of the Galaxy, the Y–axis is in the direction of rotation of the galactic disk, and the Z–axis is directed to the North Pole of the Galaxy. The directions of the spatial velocity components are similar.

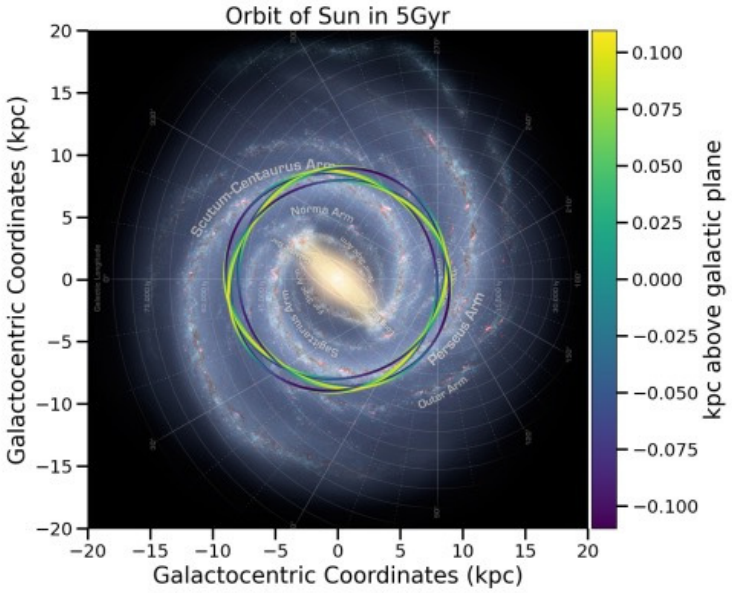

Figure 1. The Sun motion in our Galaxy model. Color bar shows the distance of the Sun to the Galaxy disk plane.

In the XY–plane on Fig. 1, the position of the orbit during the integration time occupies a strip about 1000 pc wide. In this case, along the Z–coordinate, the orbit changes by ± 100 pc.

What the number of the revolutions of the Sun n_{Sun} are shown in Fig. 1? Based on the fact that the Sun speed is $V_0 = 232.8$ km s^{-1} ($\approx$ 233 pc per million year), we found the path length for 5 billion years. It will be $L \approx 1155$ kpc. The orbital length of the the one period is $L_{orb} = 2\pi R_0 \approx 50.5$ kpc. Then

$n_{Sun} \approx 22$. Thus, Fig. 2 shows the orbit of the Sun for one revolution equal to $\approx$ 250 million years.

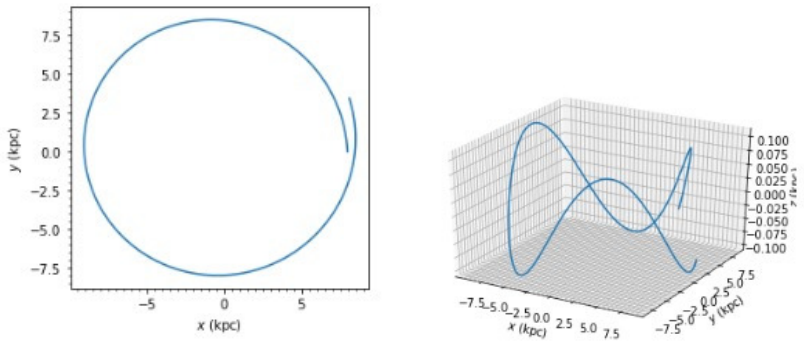

Figure 2. Full revolution of the Sun around the Galaxy Center. Left panel shows the orbit of the Sun in the XY–plane, right panel – in the 3D space.

What causes the orbital oscillations in Z–coordinate (clearly visible on Fig. 1 and Fig. 2)? There are two reasons: 1) the position of the Sun is not exactly in the plane of the Galaxy (Z = 20.8 pc) and 2) the asymmetry of the potential due to the spatial shape of the bulge.

Thus, if the comet is lost by the Solar cometary spear, it is unlikely to meet the Sun again. Indeed, the size of the area or the dimensions of the target is 1000×100 pc.

5. The results of the simulation of the evolution of the Solar and star cluster comet spears

5.1. Comet Clouds Representation

Our model is consisting of decaying objects. We represent the objects themselves as gravitationally unbound points n=1000, point-centered at the time $t = 0$ and then scattering in all directions with particular velocity. The velocity module is different for each type of objects - comets, stars, and star clusters. The cloud lost by the Solar system includes $n = 1000$ points with velocities uniformly distributed over the sphere with radius $v_{ACP} = \sqrt{u^2 + v^2 + w^2}$.

In our study, we considered both clouds of comets leaving the planetary system (for example, the Sun), and clouds of comets lost by all the open cluster member stars. Cometary clouds, leaving the parent star, turn into spatially stretched structures resembling spears in their features. Over time, the spears begin to become cometary streams enclosed in a rings around the Galaxy Center.

5.2. Simulation study of ACPS

We consider two stages of the ACPS clouds formation:

– Comets lost by a star (Sun) with the velocity assumed to be the same for all comets and is 2 km s^{-1} (Tutukov et al., 2020);

– Star clusters disintegrate and loose individual stars at an average speed of 1 km s^{-1}.

As a result of the open cluster evolution, a spear consisting of stars and comets is formed. The calculation results of our model are presented in Fig. 3.

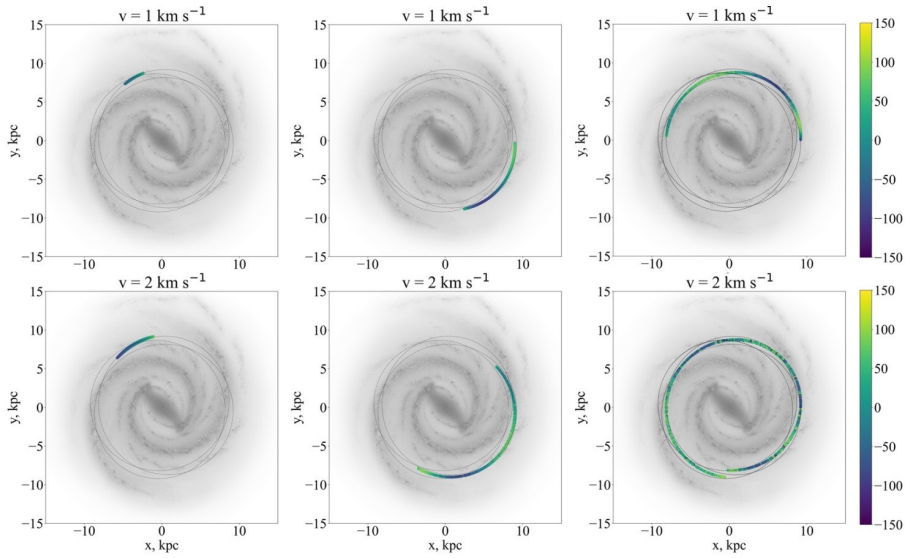

Figure 3. Evolution of stellar and cluster ACPS spears in the time intervals 1, 4.6 and 10 Gyr. Top panels show the evolution of the spear that scatters with velocity v = 1 km s^{-1}, bottom panel with v = 2 km s^{-1}. Color shows pc above the Galactic plane (Z–axis).

Obviously, over time ≈ 10 Gyr, the spear consisting of the stars and small bodies will close, revolving around the Galaxy Center and form an annular stream.

Comets and other members of the ACPS family leaving the parent star at speeds of several kilometers per second end up in the interstellar space of the Galaxy. Thus, a cloud resembling a spear is formed. We named the cometary spear of the Sun and other stars the solid-state ACP component lost by the Sun and other stars during the formation of their planetary systems. In a sense,

they expand the boundary of the parent star's planetary system, effectively distributing the matter of this planetary system far beyond the star.

Stars with planetary systems soon begin to be accompanied by ACP clouds in the form of spears or even rings, depending on the age of the star. These objects are quite common in the Galaxy since about a third of the stars have planets (Masevich & Tutukov, 1988).

5.3. The width of the ACPS stream

We considering the kinematics of

– a cometary spear of the star (the Sun) – comets leave the Solar system at a velocity v = 2 km s^{-1};

– a cometary spear of the open cluster – comets leave the cluster at a velocity v = 1 km s^{-1}.

Fig. 3 shows the star (the Sun) with a cometary spear, and an open cluster with an aggregated comet spear. These spears make the same number of revolutions around the Galactic Center (22 for 5 billion years). The orbits fill a flattened torus with a cross-section of 100×1000 pc.

However, due to the potential of the Galaxy Eqs. 4 - 6 the comet stream is expanded to about one kpc, see Fig. 4. Fig. 4 demonstrate an increase in the filling density of the torus with orbits in the projection onto the XY plane.

As can be seen in Fig. 4, the comets cross-section density increases with a scattering velocity increasing. This is due to the expansion of the ACPS spear, the width of which depends on the peculiar velocity of the comets and galactic potential by Miyamoto & Nagai (1975) and Navarro et al. (1996).

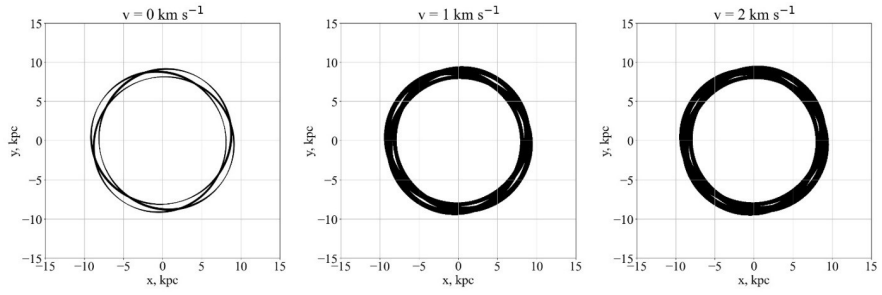

Figure 4. Calculation of the orbits of the Sun (left panel), clouds (spears) of Sun comets (middle panel), spears of cluster comets (right panel). Integration time is 4.6 billion years.

6. Conclusion.

This work is devoted to the numerical study of the evolution of the orbits Free (unbound) ACPS in the Galaxy, leading to their transformation into cometary spears of the Sun, stars, star clusters. Gradually, they form a well–populated ACP component of the Galaxy, composed of filaments of evolved ACP clouds.

The stellar component of the ACPS spears is now discovered for several clusters with ages $\sim 10^8$ years (Li et al., 2021). Their length corresponds to the expansion velocities ~ 0.5 km s^{-1}. Thus, the formation of ACPS spears of open clusters is well supported now by observations.

Acknowledgements. Authors thank the referee for the helpful comments. Authors acknowledge the support of Ministry of Science and Higher Education of the Russian Federation under the grant 075-15-2020-780 (N13.1902.21.0039).

References

Borisov, G., Ionov, I., Bryzgalov, O., et al., Comet C/2013 n4 (borisov). 2013, *Minor Planet Electronic Circulars*, **2013-N51**

Bovy, J., galpy: A python Library for Galactic Dynamics. 2015, *Astrophysical Journal, Supplement*, **216**, 29, DOI: 10.1088/0067-0049/216/2/29

Chandrasekhar, S., Dynamical Friction. III. a More Exact Theory of the Rate of Escape of Stars from Clusters. 1943, *Astrophysical Journal*, **98**, 54, DOI: 10.1086/144544

Correa-Otto, J. A. & Calandra, M. F., Stability in the most external region of the Oort Cloud: evolution of the ejected comets. 2019, *Monthly Notices of the RAS*, **490**, 2495, DOI: 10.1093/mnras/stz2671

Dones, L., Weissman, P. R., Levison, H. F., & Duncan, M. J. 2004, *Oort cloud formation and dynamics*, ed. M. C. Festou, H. U. Keller, & H. A. Weaver, 153

Eremeeva, A. 2006, *History of meteoritics. Origins. Birth. Formation.* (Dubna: Phoenix+)

Faintich, M. B. 1971, Interstellar Gravitational Perturbations of Cometary Orbits., PhD thesis, UNIVERSITY OF ILLINOIS AT URBANA-CHAMPAIGN.

Froncisz, M., Brown, P., & Weryk, R. J., Possible interstellar meteoroids detected by the Canadian Meteor Orbit Radar. 2020, *Planetary Space Science*, **190**, 104980, DOI: 10.1016/j.pss.2020.104980

Gagné, J., Faherty, J. K., Moranta, L., & Popinchalk, M., A Number of nearby Moving Groups May Be Fragments of Dissolving Open Clusters. 2021, *Astrophysical Journal, Letters*, **915**, L29, DOI: 10.3847/2041-8213/ac0e9a

Gravity Collaboration, Abuter, R., Amorim, A., et al., A geometric distance measurement to the Galactic center black hole with 0.3% uncertainty. 2019, *Astronomy and Astrophysics*, **625**, L10, DOI: 10.1051/0004-6361/201935656

Hallatt, T. & Wiegert, P., The Dynamics of Interstellar Asteroids and Comets within the Galaxy: An Assessment of Local Candidate Source Regions for 1I/'Oumuamua

and 2I/Borisov. 2020, in AAS/Division of Dynamical Astronomy Meeting, Vol. **52**, *AAS/Division of Dynamical Astronomy Meeting*, 201.03

Li, N., Li, C., Mo, H., et al., Estimating dust attenuation from galactic spectra. II. Stellar and gas attenuation in star-forming and diffuse ionized gas regions in MaNGA. 2021, *arXiv e-prints*, arXiv:2103.00666

Masevich, A. G. & Tutukov, A. V., Stellar evolution: Theory and observations. 1988, *Moscow Izdatel Nauka*

McMillan, P. J., The mass distribution and gravitational potential of the Milky Way. 2017, *Monthly Notices of the RAS*, **465**, 76, DOI: 10.1093/mnras/stw2759

Meech, K. J., Weryk, R., Micheli, M., et al., A brief visit from a red and extremely elongated interstellar asteroid. 2017, *Nature*, **552**, 378, DOI: 10.1038/nature25020

Miyamoto, M. & Nagai, R., Three-dimensional models for the distribution of mass in galaxies. 1975, *Publications of the ASJ*, **27**, 533

Mróz, P., Poleski, R., Gould, A., et al., A Terrestrial-mass Rogue Planet Candidate Detected in the Shortest-timescale Microlensing Event. 2020, *Astrophysical Journal, Letters*, **903**, L11, DOI: 10.3847/2041-8213/abbfad

Navarro, J. F., Frenk, C. S., & White, S. D. M., The Structure of Cold Dark Matter Halos. 1996, *Astrophysical Journal*, **462**, 563, DOI: 10.1086/177173

Safronov, V. S. 1969, *Evoliutsiia doplanetnogo oblaka.*

Tutukov, A. V., Early Stages of Dynamical Evolution of Star Cluster Models. 1978, *Astronomy and Astrophysics*, **70**, 57

Tutukov, A. V., The Role of Gravitational Radiation in the Evolution of Stars and Galaxies. 2019, *Astronomy Reports*, **63**, 79, DOI: 10.1134/S1063772919020082

Tutukov, A. V., Dremova, G. N., & Dremov, V. V., Generation of Unbound Comets and Planets by Planetary Systems. 2020, *Astronomy Reports*, **64**, 936, DOI: 10.1134/S1063772920110098

Tutukov, A. V. & Smirnov, M. A., Peripheral Structures of Planetary Systems. 2004, *Solar System Research*, **38**, 279, DOI: 10.1023/B:SOLS.0000037463.42719.71

Contrib. Astron. Obs. Skalnaté Pleso **51**, 280 – 284, (2021)
https://doi.org/10.31577/caosp.2021.51.3.280

Prospects to observe comets and asteroids using Russian-Cuban Observatory

M. Ibrahimov[1], D. Bisikalo[1], A. Fateeva[1], R. Mata[2] and O. Pons[2]

[1] *Institute of Astronomy, Russian Academy of Sciences, Moscow, Russia*

[2] *Institute of Geophysics and Astronomy, AMA CITMA, Havana, Cuba*
(E-mail: mansur@inasan.ru)

Received: August 10, 2021; Accepted: December 1, 2021

Abstract. Article reports about prospects to observe comets and asteroids using Russian-Cuban Observatory (RCO). In 2021, RCO wide-field 20cm robotic telescope was put into operation. The telescope has 20 cm aperture, 3.5x3.5 degree field of view and FLI PL16803 4K CCD camera with a set of $UBVRI$ photometric filters. Telescope itself will be used as a multi-task networking observational tool. Using this Cuban telescope with telescopes located in Russia makes it possible to conduct quasi-day-and-night monitoring of comets and asteroids on an arc of more than 200 degrees.

Key words: robotic telescope – astrometry – photometry

1. Introduction

Since 2017, the Institute of Astronomy of the Russian Academy of Sciences (INASAN, Moscow, Russia) and the Institute of Geophysics and Astronomy (IGA, Havana, Republic of Cuba) have been implementing a joint international project (Bisikalo et al., 2018). Project main goal is to build the Russian-Cuban Observatory (RCO, see Alonso et al. 2020, Rev. Cubana Fisica, 37, 162). In 2021, the first RCO optical station in Havana was put into operation (Bisikalo et al. 2022, Astronomy Reports, 99, 1, accepted). Main instrument of this station is an optical wide-field 20cm robotic telescope. Telescope itself will be used as a multi-task networking observational tool. Brief technical description of 20cm telescope and its attachments is provided below. Brief discussion of 20cm telescope network using in frame of Russia-Cuba arc is also presented.

2. IGA optical station and 20cm robotic telescope

A general view of the optical station is shown in Fig. 1. Wide-field 20cm robotic telescope with a set of its attachments is shown in Fig. 2. Optical station is located in a single-floor building on the territory of IGA, Havana. Optical station consists of the following main elements: a) automated dome, b) wide-field

Figure 1. General view of Russian-Cuban Observatory optical station in IGA (Havana, Republic of Cuba).

telescope on an intelligent mount, c) image recording module, d) control, computing, network and meteorological equipment.

An automated 3-meter dome and a 20cm wide-field robotic telescope are installed on the roof of the building Telescope is located in the dome and elevated using 4.2-meter massive concrete column which is separated from the common foundation. The control, computing and network equipment of the observatory is located inside the building.

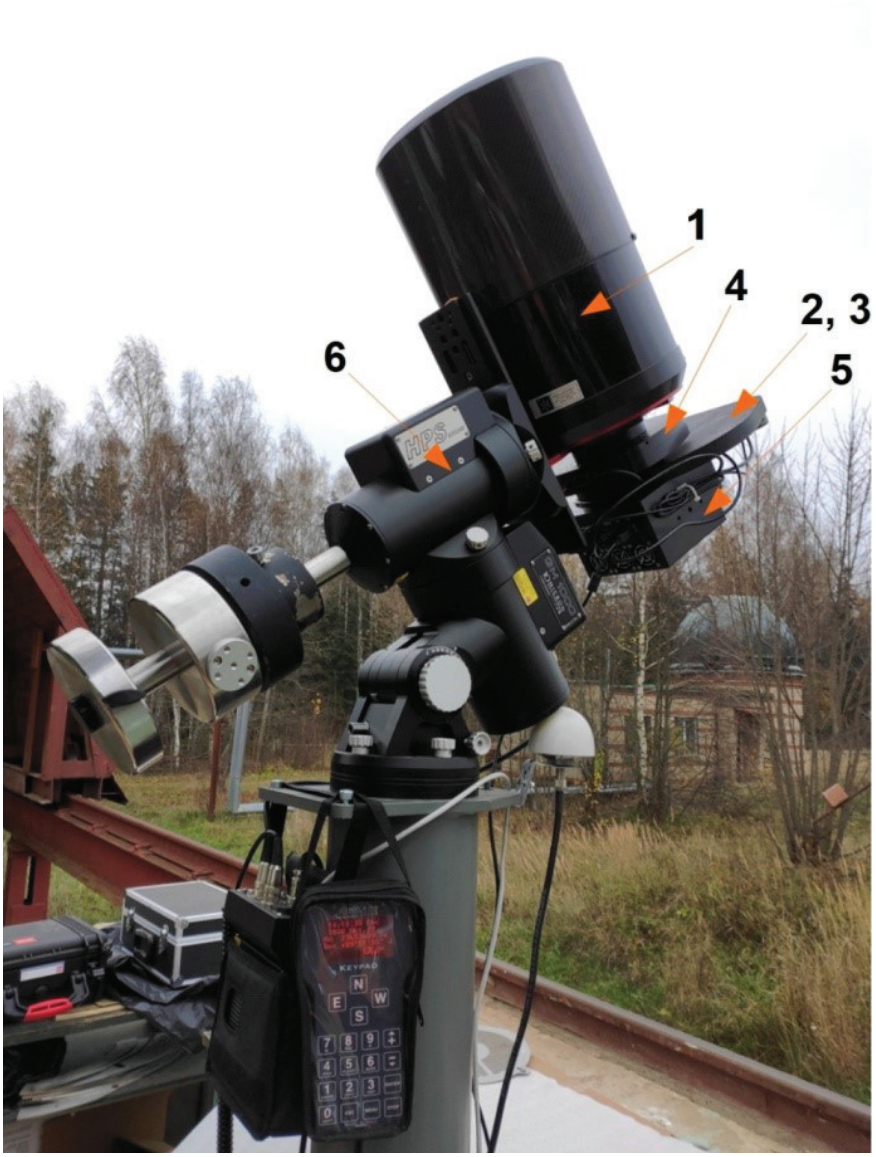

Figure 2. Wide-field 20cm robotic telescope with a set of its attachments. Designated: 1 – Officina Stellare Veloce RH200 mirror-and-lens telescope (200 mm aperture, 600 mm focal length, 3.5x3.5 degree field of view); 2 – 7-position FLI CFW5-7 filter wheel; 3 – set of Johnson-Cousins $UBVRI$ photometric filters (50x50 mm size, installed inside FLI CFW5-7 filter wheel); 4 – FLI ATLAS focuser (3", 105000 steps, 85 nm/step, 8.9 mm stroke); 5 – FLI PL16803 4K CCD camera; 6 – 10 Micron GM1000 HPS mount.

The following technical equipment was used to robotize observing:

i) 3-meter ScopeDome 3M automated dome;

ii) 20cm Officina Stellare Veloce RH200 wide-field telescope with 3.5x3.5 degree field of view;

iii) 10 Micron GM1000 HPS high-precision equatorial mount with 25 kg load capacity and absolute position sensors;

iv) FLI PL16803 4K CCD camera with FLI ATLAS automated focusing unit, 7-position FLI CFW5-7 automated filter wheel, and a set of optical filters to realize $UBVRI$ broadband photometric system.

Entire optical station is operated using a software to remote control, observing, data storage and processing. A wide-field optics of 20cm robotic telescope were adjusted at INASAN Optical Laboratory. Taking into account some natural limitations due to atmospheric conditions and image scale of 3.08" per pixel for FLI PL16803 4K CCD camera, achieved image quality is $FWHM \approx 5$" across entire field of view.

3. 20-cm RCO telescope as a multi-task tool: prospects to observe comets and asteroids

Newly commissioned 20cm wide-field robotic telescope is supposed to use as a multi-task astrometric and photometric instrument. A range of solved research tasks is thought to be wide from near-Earth and Solar space tasks (space debris, Solar System small bodies, etc.) to deep-space astrophysical tasks (observations of active and spotted variable stars, detection and/or follow-up observations of Gamma-Ray Burst optical afterglows, etc.). The list of research tasks performed using this telescope includes also observations of various comets and asteroids including Near-Earth Asteroids and Potentially Hazardous Asteroids.

Above described multi-task capability of RCO 20cm robotic telescope implies its usage on a permanent base together with the Simeiz Observatory 1m Zeiss-1000 and Terskol Observatory 2m Zeiss-2000 telescopes of INASAN Center for collective use (http://www.inasan.ru/divisions/terskol/ckp, (Nikolenko et al., 2019). Also, described network scheme will include 50cm telescope of Ussuriysk Department, Institute of Applied Astronomy of the Russian Academy of Sciences and 0.5-1.5m telescopes of two Astronomical Institutes of the Academy of Sciences of Republic of Uzbekistan and Republic of Tajikistan.

The implementation of such a network makes it possible to conduct optical astronomical monitoring using an arc of 214 degree (or 14.3h) in the northern hemisphere of the sky. Taking into account a natural duration of observational night (from 6 to 12 hours for the sites involved), above network will make it possible to conduct quasi- day-and-night monitoring in near-Earth, Solar and deep space. Comets were observed many times in UV by large space telescopes such as Hubble Space Telescope (see a review by Sachkov (2016)). Russian project "Spektr-UF" (The World Space Observatory - Ultraviolet, WSO-UV),

which is scheduled to launch in 2025, will effectively solve most problems in the field of ultraviolet studies of comets and can become an important research tool (Sachkov et al., 2018, 2019). Data on comets are very important for the study of the formation of planetary systems (Fossati et al., 2014).The wide-field 20cm robotic telescope at the Russian-Cuban Observatory may be an instrument for ground support of space observations.

4. Conclusions

Paper reports about commissioning of the wide-field 20cm robotic telescope at the Russian-Cuban Observatory. Telescope is installed at the optical station in the Institute of Geophysics and Astronomy (Havana, Republic of Cuba). General views of the optical station and its 20cm telescope are shown, telescope attachments are described. Multi-task observational projects that will be carried out using RCO 20cm telescope are briefly discussed. Russia-Cuba network scheme is described and its prospects to observe Solar System small bodies (comets, asteroids, etc.) are briefly discussed.

Acknowledgements. This work was supported by the Ministry of Science and Higher Education of the Russian Federation, Agreement No. 075-15-2019-1716 of November 20, 2019.

References

Bisikalo, D. V., Savanov, I. S., Naroenkov, S. A., et al., Perspectives for Distributed Observations of Near-Earth Space Using a Russian-Cuban Observatory. 2018, *Astronomy Reports*, **62**, 367, DOI: 10.1134/S1063772918060021

Fossati, L., Bisikalo, D., Lammer, H., Shustov, B., & Sachkov, M., Major prospects of exoplanet astronomy with the World Space Observatory-UltraViolet mission. 2014, *Astrophysics and Space Science*, **354**, 9, DOI: 10.1007/s10509-014-2027-3

Nikolenko, I. V., Kryuchkov, S. V., Barabanov, S. I., & Volkov, I. M., Telescopes of the INASAN Simeiz Observatory: current state and prospects. 2019, *INASAN Science Reports*, **4**, 85, DOI: 10.26087/INASAN.2019.4.2.015

Sachkov, M., Sichevsky, S., Kanev, E., & Kartashova, A., WSO-UV Field Camera Unit: science case and ground support with 1-m class telescopes. 2019, *Contributions of the Astronomical Observatory Skalnate Pleso*, **49**, 145

Sachkov, M. E., Spectral studies of comets in the ultraviolet range and prospects of the WSO-UV project in these studies. 2016, *Solar System Research*, **50**, 294, DOI: 10.1134/S0038094616040055

Sachkov, M. E., Kartashova, A. P., & Emel'yanenko, V. V., Prospects for spectral studies of comets: The World Space Observatory - Ultraviolet project. 2018, *Planetary Space Science*, **164**, 75, DOI: 10.1016/j.pss.2018.06.013

PRÁCE ASTRONOMICKÉHO OBSERVATÓRIA
NA SKALNATOM PLESE
LI, číslo 3

Zostavovatelia:	Dr. Mikhail Sachkov
	Dr. Anna Kartashova
Výkonný redaktor:	RNDr. Richard Komžík, CSc.
Vedecký redaktor:	RNDr. Augustín Skopal, DrSc.
Vydal:	Astronomický ústav SAV, Tatranská Lomnica
IČO vydavateľa:	00 166 529
Periodicita:	3-krát ročne
ISSN (on-line verzia):	1336-0337
CODEN:	CAOPF8
Rok vydania:	2021
Počet strán:	110

Contributions of the Astronomical Observatory Skalnaté Pleso are processed using LaTeX 2ε CAOSP DocumentClass file 3.08 ver. 2020.